THERMAL TRANSPORT IN TWO-DIMENSIONAL MATERIALS AND MAGNETIC MULTILAYERS

BY

HYEJIN JANG

DISSERTATION

Submitted in partial fulfillment of the requirements
for the degree of Doctor of Philosophy in Materials Science and Engineering
in the Graduate College of the
University of Illinois at Urbana-Champaign, 2019

Urbana, Illinois

Doctoral Committee:

Professor David G. Cahill, Chair and Director of Research
Professor Moonsub Shim
Assistant Professor André Schleife
Assistant Professor Arend van der Zande

ABSTRACT

Understanding thermal transport properties of materials is essential for both device applications and materials physics. Thermal conductivity and interface thermal conductance are important engineering parameters for small-scale device applications. In addition, microscopic quantities of how different types of heat carriers interact each other are of crucial importance that determine dynamics of charges and spins.

In this thesis, I use ultrafast pump-probe metrology to experimentally investigate thermal transport properties in various materials systems. The first subject is two-dimensional materials having in-plane anisotropies, i.e., black phosphorus, WTe_2, and ReS_2, which were first prepared in 2D structures all in 2014. These materials are promising candidates for next-generation electronics and optoelectronics, and the knowledge of thermal transport properties is needed for engineering heat dissipation in devices. However, the low crystal symmetries complicate experimental evaluation of the properties.

To determine thermal conductivity of the three materials along the three coordination axes, I use time-domain thermoreflectance (TDTR) of conventional geometry, where pump and probe beams are co-aligned, and TDTR of beam-offset geometry, where pump and probe beams on sample surface are spatially separated. The beam-offset TDTR allows to measure in-plane thermal conductivity along any arbitrary direction on sample planes but requires a significantly large thickness of a sample. I report the three-dimensional thermal conductivity of BP, WTe_2, and ReS_2, and their interface thermal conductance with metals. The results are discussed in terms of crystal structure, constituent elements, and atomic bonding strength, and compared with other high-symmetry two-dimensional materials.

The second topic is non-equilibrium heat transport in Pt and Co. Laser-induced non-equilibrium in metals have been extensively studied for noble metals using transient reflectance. However, the interpretation of transient reflectance is not straightforward as reflectance is affected by temperatures of electrons and phonons, and lattice strains. Transition metals also behave differently from noble metals and thus require different theoretical explanations.

I propose to use a four-atomic-layers-thick Co layer as a thermometer to probe non-equilibrium dynamics in metals. I first characterize the properties of Co, e.g., carrier coupling parameters between electrons, phonons, and magnons, by using time-resolved quadratic and linear magneto-optical Kerr effects (TR-QMOKE and TR-MOKE, respectively) on 10-nm-thick and sub-nm-thick Co layers, respectively. Then I use sub-nm-thick Co layers embedded in much thicker Pt layers to investigate non-equilibrium heat transport in Pt. The fast magnetization dynamics of the ultrathin Co layers allows to isolate the electronic temperature at a precise location in Pt/Co/Pt trilayers with sub-picosecond time-resolution. I demonstrate that a model based on the diffusive transport of heat by electrons and the exchange of heat between excitations of electrons, phonons, and magnons consistently explains the temperature evolutions in Pt with different thicknesses, 2−42 nm.

Lastly, I study thermal transport properties of magnetic tunnel junctions (MTJs). MTJs show interesting charge and spin dynamics when they are subject to temperature gradient, such as the tunnel-magneto Seebeck effect and spin Seebeck tunneling. To harness the thermally induced spin behaviors, it is essential to accurately describe the temperature profiles across an MTJ structure while the challenge is to determine the temperature drop across an oxide tunnel barrier. In this work, I use a Co or CoFeB electrode layer in an MTJ as a thermometer and determine the effective thermal conductivity across oxide tunnel barriers, MgO and $MgAl_2O_4$.

ACKNOWLEDGMENTS

I owe a debt of gratitude to many people in graduate school. First, I would like to thank my advisor, Prof. David G. Cahill, for his guidance over the course of my PhD degree. I was first interested in his group as my collaborators back in my master's course suggested TDTR would be a powerful tool to learn. Their suggestion is true, but I have learned far more than that. I admire his critical thinking and enthusiasm towards scientific understanding and techniques. I especially appreciate our weekly meeting on Fridays where I can consult him about all the levels of research, and often get delighted with puzzles solved. Thanks, David, your style of doing research will keep inspiring me in my future careers.

I also would like to thank Prof. Moonsub Shim, Prof. André Schleife, and Prof. Arend van der Zande for serving on my PhD committee and taking time to evaluate my thesis. I acknowledge the support from excellent staffs in the Materials Research Laboratory.

Many collaborators have shared the opportunities for exploring exciting research topics that are not all covered in this thesis: Prof. Goldberger's group at the Ohio State University, Prof. Hersam's group at Northwestern University, Prof. Cha's group at Yale University, and Prof. Johnson's group at the University of Oregon have provided me with 2D materials samples. Dr. Kuschel at Bielefeld University in Germany has provided magnetic tunnel junction samples.

I am grateful for all the group members that I have spent time together and shared happy and frustrating moments: Rich, Jonglo, Gyung-Min, Dongyao, Jun, Johannes, Judith, Xu, Qiye, Jungwoo, Kexin, Kisung, Sushant, Akash, Guangxin, Xiaoyang, Jordan, Wenrui, Kathleen, and Renee. I give special thanks to Greg Hohensee for helping me with getting started in the group and building a solid background in TDTR. Zhu Diao is an expert on all of the instruments and

has saved me from numerous troubles. I thank Ella Pek for our friendship since we joined the group together.

I also thank my friends in the MatSE department and at Winfield Village, who have amused my life in Urbana-Champaign. The happy memories of having parties, road trips, and playing tennis have helped me survive the PhD program. Thanks for caring me like a family member and celebrating important events together.

Finally, I am deeply grateful for my family for their endless support and love. My husband, Jongkyu, was teaching me thermodynamics when we first met, and he is now the person who I am seeking life advice from. This thesis is dedicated to him.

I acknowledge financial support from Kwanjeong Educational Foundation in Korea, National Science Foundation EFRI-1433467, and Army Research Office MURI W911NF-14-1-0016.

TABLE OF CONTENTS

CHAPTER 1
INTRODUCTION

1.1. Motivation

Understanding thermal transport properties of materials is essential for engineering of small-scale devices. The smaller size and higher operational speed of microelectronic devices accompany a higher power density, which becomes a major factor liming the integrated circuit density and performance of devices. [1] Proper cooling of heat should be provided through electrical contacts and requires the knowledge of thermal conductivity of constituent materials and interfacial thermal transport between different materials.

Thermal transport properties are also one of fundamental materials properties and closely linked to a variety of physical phenomena in materials physics. In particular, energy exchange processes between different types of heat carriers in solids, e.g., electrons, phonons, and magnons, provide important energy relaxation channels for quasi-particles. [2] For example, electron-phonon interaction is manifested in lifetimes of conduction electrons for intrinsic electrical resistivity in metals, lifetimes of electron-hole pairs in semiconductors, and formation of Cooper pairs in superconductors.

Direct optical excitation of materials using ultrafast laser pulses creates non-equilibrium among different types of heat carriers and allows to experimentally investigate heat transport and exchange processes that occur on fast time scales, e.g., 10 fs to 100 ps. Understanding of laser-induced non-equilibrium dynamics itself is also important from the perspective of spintronics. Direction excitation of ferromagnetic materials with an ultrafast laser pulse has demonstrated demagnetization about 1000 times faster than when using magnetic or electrical means. [3] The

non-equilibrium among carriers in magnetic structures and devices subject to temperature gradient can also generate spin-polarized currents via the spin Seebeck effect [4,5] and Seebeck spin tunneling. [6]

In this thesis, I study thermal transport properties of various materials systems using ultrafast pump-probe metrology. I determine equilibrium thermal transport properties of layered materials that were recently prepared in two-dimensional (2D) structures and have distinct in-plane anisotropies (Chap. 3). I also investigate non-equilibrium heat transport properties in Co and Pt (Chap. 4), and in magnetic tunnel junctions (Chap. 5).

1.2. Two-dimensional materials with distinct in-plane anisotropy

Van der Waals layered materials have attracted great interest for next-generation electronics. Due to the anisotropic atomic bonding structure, i.e., strong covalent bonds within the planes and much weaker van der Waals bonds along the layering axis, the layered materials can be easily isolated into atomically thin but stable structures consisting of only one or few layers. The low dimensionality gives rise to novel and exotic materials behaviors. For example, the exceptionally high carrier mobilities on the planes and tunable electron band gaps make 2D materials promising for transistors and optoelectronic devices of nanoscale. [10]

Among various emerging 2D materials, I choose the materials that have distinct in-plane anisotropy: black phosphorus (BP) [7], WTe_2 [8], and ReS_2. [9] The in-plane anisotropies lead to orientation-dependent transport and optical properties, such as orientation-dependent giant magnetoresistance [8], superconductivity [11], and out-of-plane spin-orbit torque [12]. The three-dimensional crystalline anisotropies give larger degrees of freedom to tailor the materials properties.

Black phosphorus (BP) is a stable phosphorus allotrope at ambient temperature and pressure. [13] The plane of BP is of a puckered honeycomb structure, where the directions orthogonal and parallel to the puckered directions are referred to as zigzag (*a*) and armchair (*c*) directions, respectively. (See Fig. 1.1(a))

In transition metal dichalcogenides (TMDs), MX_2, the stacking order of X-M-X hexagonal planes is different in 2*H* and 1*T* phases: a 2*H* phase is Bernal-stacked, i.e., the stacking order of the planes is A-B-A B-A-B, and the unit cell contains two X-M-X layers. In this geometry, M atoms are located at the center of triangular prisms of X atoms. The stacking order in a 1*T* phase is A-B-C A-B-C, and the unit cell contains only one X-M-X layer. In a 1*T* phase, M atoms have an octahedral coordination.

Some TMDs have distorted 1*T* phases, in which M atoms cluster to form anisotropic patterns within the layer [14]: metal atoms of d^2 electron configuration (e.g., Group VI) form zigzag chains (e.g., $MoTe_2$ and WTe_2) and those of d^3 configuration (e.g., Group VII) form diamond chains (e.g., ReS_2 and $ReSe_2$). The crystal symmetry and lattice parameters of BP, WTe_2, and ReS_2 are summarized in Table 1.1. Note that for WTe_2, *a*-axis is parallel to W chains and *c*-axis is normal to the planes, and for ReS_2, *a* and *b* axes are in-plane axes, and *b*-axis is parallel to the Re-chains. (See Fig. 1.1(b)-(c).) The electrical properties of BP, WTe_2, and ReS_2 are summarized in Table 1.2.

Research of thermal conductivity of 2D materials has been mostly concerned with high-symmetry materials, such as graphene [15–18] and TMDs in a hexagonal 2*H* phase, e.g., MX_2 (M=Mo, W and X=S, Se). [19–21] The six-fold in-plane symmetry of these materials results in isotropic in-plane thermal conductivity. Measurements of orientation-dependent in-plane thermal

conductivity has been challenging due to the difficulty in identifying and orienting samples along crystalline axes and the complexity in heat transport problems.

In this study, I use conventional [22] and beam-offset [23,24] time-domain thermoreflectance (TDTR), which account for through-plane and in-plane thermal transport, respectively. From measurements, I derive the 3D thermal conductivity tensors of BP, WTe_2, and ReS_2, along the three coordination axes. As BP [7] and ReS_2 [9] are semiconductors, and WTe_2 [8] is a semi-metal, as shown in Table 1.2, most of the thermal conductivities (i.e., >99%) of these three materials are carried by phonons and closely related with the crystal symmetries and constituent elements. The in-plane thermal conductivity is higher than the through-plane thermal conductivity by more than an order of magnitude, due to the layered structures. The specific orientation-dependency of in-plane thermal conductivity varies depending on the materials. The effects of the atomic elements, crystal structures, and interlayer bonding strength on the thermal conductivities of these materials are discussed, in comparison with high-symmetry 2D materials.

1.3. Non-equilibrium carrier dynamics in metals

Non-equilibrium among different thermal reservoirs following ultrafast laser irradiation occurs as follows: when a laser pulse of a visible wavelength is incident on the surface of a metal, the photon energy is absorbed by electronic excitations while other excitations, i.e., phonons and additionally magnons for metals including magnetic elements, remain cold. The photo-excited electrons (“hot electrons”) initially deviate from the Fermi-Dirac distribution and subsequently relax to a new thermal equilibrium. Initially, the hot electrons are predominantly scattered via electron-electron interactions—i.e., with ground-state electrons at a low excitation

density, $<10^{-3}$ of the total electron density—and further with other electronic excitations at a higher excitation density. [25] The electrons then reach equilibrium with the other excitations in the metal through electron-magnon and electron-phonon interactions.

If a sample is thicker than the optical absorption depth, part of energy relaxation of hot electrons and thermalized electrons proceeds by transport from one region of the sample to another. Hot electrons with excitation energy much larger than thermal energy, i.e., $E–E_F >> k_BT$, tend to propagate ballistically, as have been studied comprehensively in Au, [26,27] whereas thermal electrons propagate diffusively. Ballistic and diffusive transport are characterized by the propagation distance proportional to t and $t^{1/2}$, respectively, where t is the propagation time. Battiato *et al.* [28] discuss the importance of super-diffusive transport, the cross-over from ballistic to diffusive transport when hot electrons undergo few scattering events.

The laser-induced nonequilibrium dynamics have been commonly described by using a phenomenological three-temperature model (3TM) or reduced to a two-temperature model for non-magnetic metals. The 3TM is based on a set of differential equations for temperatures of electrons (T_e), phonons (T_{ph}), and magnons (T_m), as described by Eqs. (1.2–4). The energy transfer between thermal reservoirs i and j ($i, j=e, ph, m$) is described by a carrier coupling parameter, g_{ij}. I ignore phonon-magnon coupling, which I assume is much weaker than the other couplings in ferromagnetic metals. [29] C_i and Λ_j are the heat capacity and thermal conductivity of a thermal reservoir i, respectively. The absorption of photons by the electronic excitations is described via a source term, $S(z,t)$, see Eq. (1.5). $P(t)$ is a temporal profile of a pulse intensity and $A(z)$ is the absorption profile calculated using a transfer matrix method; S_0 is a pre-factor to normalize $S(z,t)$ to an absorbed laser fluence; w_0 is the $1/e^2$ beam radius. The temperature

evolutions of the three thermal reservoirs as a function of position and time, $T_i(z,t)$, are obtained by numerically solving the Eqs. (1.1–3).

$$C_e \frac{\partial T_e}{\partial t} = \Lambda_e \frac{\partial^2 T_e}{\partial z^2} - g_{ep}(T_e - T_{ph}) - g_{em}(T_e - T_m) + S(z,t) \tag{1.1}$$

$$C_{ph} \frac{\partial T_{ph}}{\partial t} = \Lambda_{ph} \frac{\partial^2 T_{ph}}{\partial z^2} + g_{ep}(T_e - T_{ph}) \tag{1.2}$$

$$C_m \frac{\partial T_m}{\partial t} = \Lambda_m \frac{\partial^2 T_m}{\partial z^2} + g_{em}(T_e - T_m) \tag{1.3}$$

$$S(z,t) = \frac{S_0}{\pi w_0^2} P(t) A(z) \tag{1.4}$$

However, the 3TM has been constantly criticized for its underlying assumption of internal thermal equilibrium of each reservoir, i.e., a single temperature can be defined for each reservoir. This assumption is not valid especially when the electrons are excited upon irradiation and deviate from the Fermi-Dirac distribution. The time for the excited electrons to thermalize to a new equilibrium of a higher temperature varies from 10 fs to 1 ps, depending on materials.

In this work, I choose Pt as a model system and investigate non-equilibrium dynamics in Pt and the applicability of the 3TM. Pt has been widely used in spintronics due to its large spin Hall angle [30] and well-established perpendicular magnetic anisotropy in multilayer structures with Co. [31] The behaviors of hot electrons in Pt are also crucial for catalytic applications with gases molecules. [32] As Pt is a transition metal having nine electrons in the 5*d* orbitals, the *d*-orbitals dominate the density of states near the Fermi level [33] and significantly influence the excitation and relaxation processes of electrons. (See Figure 1.2.) Therefore, Pt is expected to exhibit non-equilibrium carrier dynamics that are distinguished from those of noble metals.

Fermi liquid theory provides an estimate for the lifetimes of hot electrons, $\tau_{ee}(E)$, within the random phase approximation [25]

$$\frac{1}{\tau_{ee}(E)} = \frac{1}{\tau_0}\frac{(E-E_F)^2}{{E_F}^2} \tag{1.5}$$

where $\tau_0 = \frac{128}{\pi^2\sqrt{3}}\frac{1}{\omega_p}$ and ω_p is plasma frequency. Eq. (1.5) is based on the free-electron gas model and is a good approximation for intra-band transitions in simple metals. If the relaxation of hot electrons follows Fermi-liquid theory, $\tau_{ee}(E)\left[E-E_F\right]^2$ is constant and equal to $\tau_0 {E_F}^2$. Time-resolved photoemission spectroscopy [25] provides measurements of $\tau_{ee}(E)$. Noble metals show qualitative agreement with Fermi-liquid theory. While Eq. (1.1) predicts $\tau_0 {E_F}^2 \approx 30$ and 17 fs eV^2 for Cu and Au, respectively, photoemission spectroscopy measurements give $\tau_{ee}(E)\left[E-E_F\right]^2 \approx 45$ and 75 fs eV^2 for Cu and Au, respectively, in the energy range 0.5 eV $\leq E\text{-}E_F \leq 2$ eV. The disagreement between $\tau_{ee}(E)\left[E-E_F\right]^2$ predicted by Eq. (1.5) and the photoemission spectroscopy data for Cu and Au can be attributed to the screening effect of completely filled *d* bands lying >2 eV below the Fermi level, which is more effective in Au than Cu. [25]

For Pt, photoemission spectroscopy data is unavailable to the best of my knowledge, but first-principles calculations [34] incorporating the full band structure suggest that $\tau_{ee}(E)\left[E-E_F\right]^2$ deviates from Fermi-liquid theory and strongly depends on excitation energy, i.e., sharply increases with increasing excitation energy up to 3 eV with $\tau_{ee} \approx 5$ fs at $(E-E_F) = 1$ eV, as shown in Figure 1.3. Insight about the behavior of Pt can be drawn from experimental data for Pd as both Pd and Pt have similar valence electronic structures. Photoemission data for $\tau_{ee}(E)$ of Pd [25] shows similar energy-dependence and magnitude to those of the theoretical prediction of $\tau_{ee}(E)$ for Pt. [34]

Additional experimental insights on $\tau_{ee}(E)$ can be drawn from the electrical resistivity measurements at $T < 20$ K [35], where electron-electron scattering dominates over electron-phonon scattering. The electrical resistivity due to electron-electron scattering (ρ_{ee}) exhibits a T^2 dependence; extrapolation to 300 K gives $\rho_{ee} \approx 1$ μΩ cm, ≈10% of the total resistivity. According to Ref. [36], the product of $\rho\tau$ is determined by the shape of the Fermi surface and gives τ_{ee} of Pt at 300 K ≈ 100 fs. If I approximate the excitation energy of near-equilibrium conduction electrons at room temperature as $2k_BT = 0.05$ eV, $\tau_{ee}(E)\left[E - E_F\right]^2$ is ≈ 0.25 fs eV^2 and $\tau_{ee}(E) \approx 100$ fs. Thus, I estimate that the electron-electron thermalization time-scale in Pt is more than an order of magnitude shorter than in Cu or Au.

In this work, I examine whether Pt shows any deviations from the predictions of the 3TM and discuss the behaviors of the non-thermal electrons in comparison with other metals, e.g., Au. I also re-examine the electronic heat capacity coefficient of Pt, for which the value derived from the low temperature measurement at $T < 30$K is commonly used.

1.4. Seebeck effects in magnetic tunnel junctions

Magnetoresistance refers to the change in electrical resistance in response to the applied magnetic field. Giant magnetoresistance (GMR) occurs in a multilayer consisting of two ferromagnetic layers separated by a non-magnetic metal, in which electrical resistance changes depending on the relative orientation of magnetizations in the two ferromagnetic layers. A greater change in electrical resistance was observed by replacing a non-magnetic metal spacer with a thin layer of insulating oxide, whose thickness is so small, i.e., only about few nm, that electrons can tunnel through the insulating layer. This structure, consisting of an insulating layer

sandwiched by two ferromagnetic layers, is referred to as a magnetic tunnel junction (MTJ), and its change in electrical resistance is referred to as tunneling magnetoresistance (TMR).

The electrical resistance (R) in MTJs is lower for parallel alignment of magnetizations than for antiparallel alignment, i.e., $R_P < R_{AP}$. The effect of TMR is evaluated by the ratio of $(R_{AP}-R_P)/R_P$. A large magnetoresistance ratio is useful for magnetic field sensors and has been utilized for read-heads of hard disk drives since 1990s. [37] A higher magnetoresistance ratio and a lower tunneling resistance are further desired for next-generation spintronics devices, including magnetoresistive random-access memory (MRAM). [37] The widely adopted MTJs are based on CoFeB/MgO/CoFeB with a combination of Ta and Ru as seed layers and capping layers. The highest TMR ratio of 604% at room temperature was observed for CoFeB(4)/MgO(2)/CoFeB(5) MTJ with in-plane magnetic anisotropy, in which numbers in parentheses represent thicknesses in nm. [38] MTJs with perpendicular anisotropy were demonstrated with CoFeB of 1−1.7 nm thickness and exhibited the TMR ratio of 120%. [39]

When MTJs are subject to temperature gradient, interesting spin-dependent transport arises depending on the relative magnetic orientation, similar to the TMR effect. The tunnel magneto-Seebeck (TMS) effect refers to the change in Seebeck coefficient, or thermopower, for parallel and antiparallel magnetic configurations. [40,41] The TMS ratio is defined as analogous to the TMR ratio: $(S_P-R_{AP})/\min(|S_P|,|S_{AP}|)$. Walter *et al.* [40] first experimentally observed the Seebeck coefficient change of −8.8% across a 2.1-nm-thick MgO tunnel barrier in MTJ with CoFeB electrodes. The TMS ratio was further improved to −95% in MTJs using half-metallic Heusler compounds, e.g., Co_2FeAl, as one of the ferromagnetic electrodes. [42]

While the TMS effect is concerned with the change in charge-Seebeck coefficients, and irrespective of spin polarized current, a combination of a ferromagnetic layer and an insulating

tunnel barrier can generate a spin current under temperature gradient, which is referred to as Seebeck spin tunneling. Le Breton *et al.* [6] demonstrated thermal spin injection from $Ni_{80}Fe_{20}$ through 1.5-nm-thick AlO_x oxide to Si electrode. The spin accumulation in Si shows the opposite polarization depending on the direction of temperature gradient across the multilayer.

The magnetization-dependent transport induced by temperature gradient across MTJs and magnetic multilayers has potential for applications in spintronics devices, such as temperature sensors and thermally-driven scanning tunneling microscopes. [41] The generation of spin current can be useful for spin-transfer-torque MRAM. [6]

For successful applications for devices, it is essential to accurately describe a temperature profile across multilayers and evaluate the relevant performance parameters. However, it is challenging to determine the thermal conductivity of a tunnel barrier consisting of only a few monolayers along with interface thermal conductance with ferromagnetic metallic layers. The first report of TMS [40] used thermal conductivity of MgO thin films, i.e., 4 W m^{-1} K^{-1}, for calculating the temperature gradient and did not consider the interface thermal conductance of the tunnel barrier. Therefore, they overestimated the TMS ratio. Zhang *et al.* [43] estimated total thermal conductance across a Fe/MgO/Fe MTJ as 10^8 W m^{-2} K^{-1} using *ab initio* calculations. This thermal conductance is more than an order of magnitude smaller than the value used in Ref. [40]. Huebner *et al.* [44] determined the thermal conductivity of 2.6-nm-thick MgO and $MgAl_2O_4$ layers as 5.8 W m^{-1} K^{-1} and 0.7 W m^{-1} K^{-1} by comparing the TMS voltage and finite-element modeling.

In this work, I experimentally determine the thermal conductivity of MgO and $MgAl_2O_4$ tunnel barriers. The sample structures are Ru(50)/oxide(2)/CoFeB(1)/Ta(5)/substrate and Ru(50)/oxide(2)/Co(0.7)/Pt(5)/substrate. The oxide layer is either MgO or $MgAl_2O_4$ (MAO) of 2

nm thickness. The substrate is MgO(001). I use time-domain thermoreflectance (TDTR) with pump and probe beams on Ru surface to determine the total conductance between Ru and MgO substrate. Then I use time-resolved magneto-optical Kerr effect (TR-MOKE) with pump on Ru surface and probe on MgO substrate to separately determine the thermal conductance across the tunnel barrier and the thermal conductance between a seed layer (Ta or Pt) and a MgO substrate. TR-MOKE employs a thin ferromagnetic layer of either Co or CoFeB as a thermometer. The materials parameters of Co are investigated in Chap. 4. I prepare thicker layer of CoFeB, of 6.5 nm thickness, capped with a 2-nm-thick Pt layer, and use time-resolved quadratic magneto-optical Kerr effect (TR-QMOKE) to determine the properties of CoFeB.

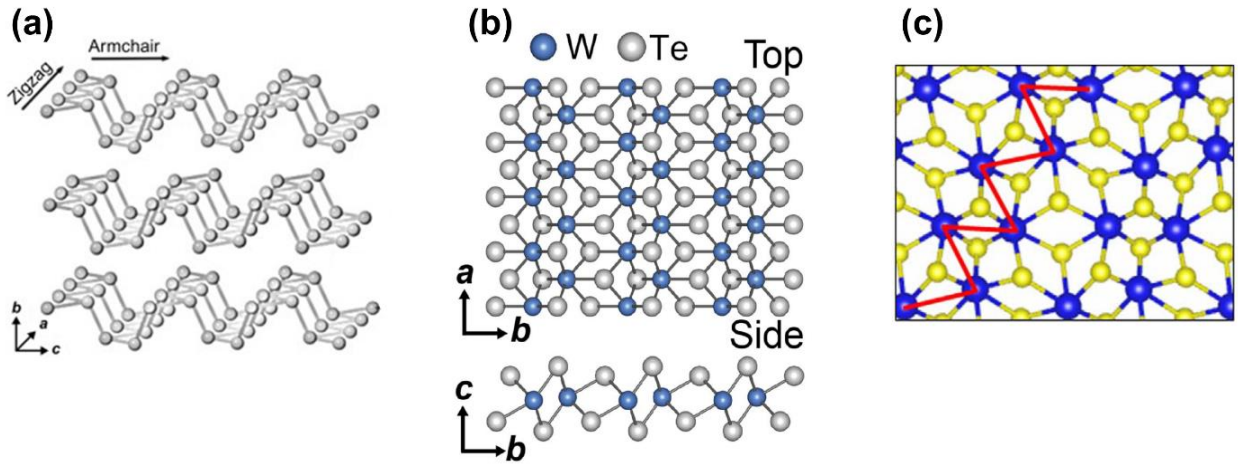

Figure 1.1. Crystal structures of (a) black phosphorus [45], (b) WTe_2 [46], and (c) ReS_2 [9]. (c) is a top-view of a ReS_2 plane where Re and S atoms are blue and yellow, respectively.

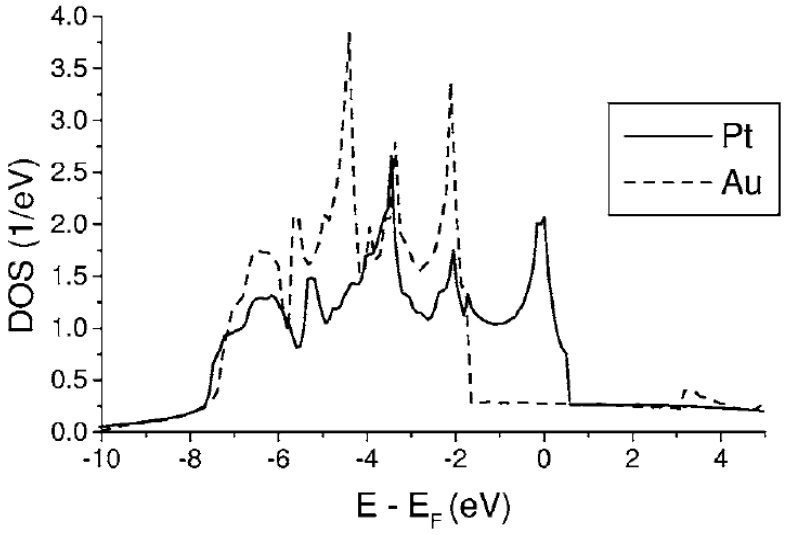

Figure 1.2. Density of states of Pt and Au taken from Ref. [34].

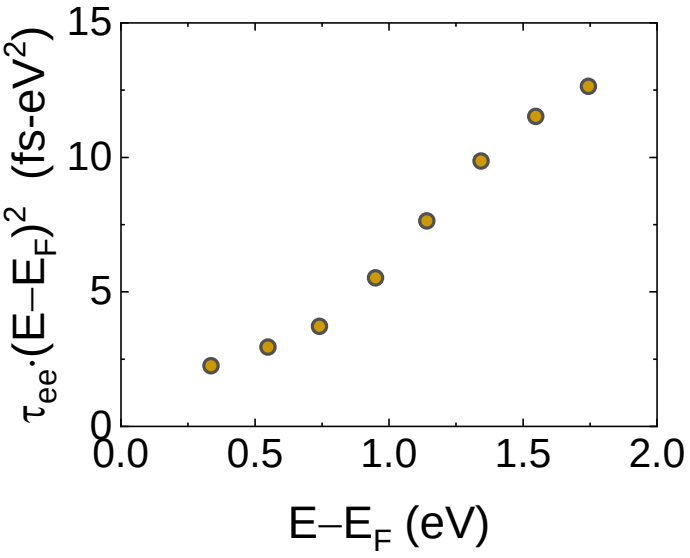

Figure 1.3. Electron-electron scattering time (τ_{ee}) of Pt as a function of excitation energy ($E-E_F$) from first-principles calculations. The data is re-plotted from Ref. [34].

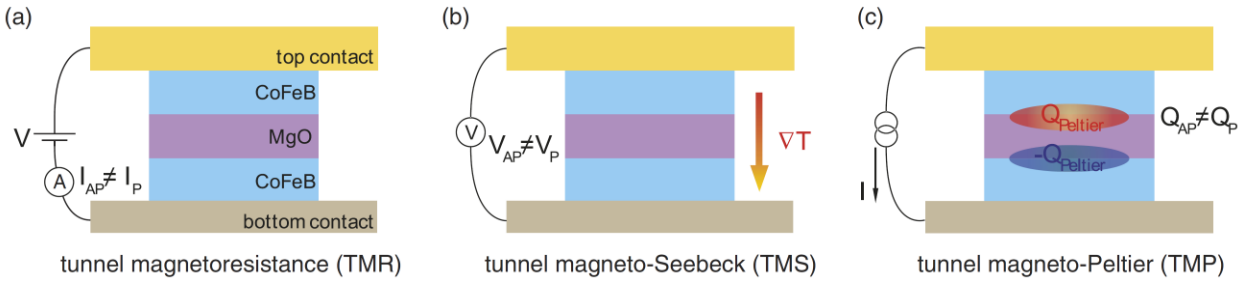

Figure 1.4. MgO-based magneto-tunnel junctions with CoFeB magnetic electrodes shows (a) tunnel magnetoresistance (TMR) with applied voltage (V), (b) tunnel magneto-Seebeck effect with applied temperature gradient (∇T), and (c) tunnel magneto-Peltier effect with applied charge current (I). The figure is taken from Ref. [41].

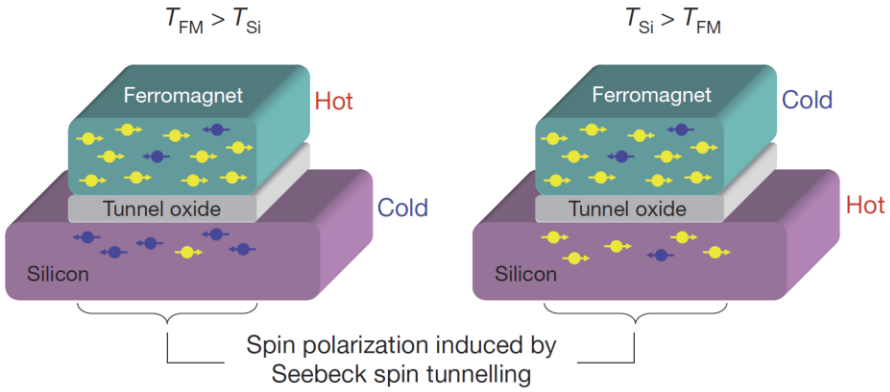

Figure 1.5. Seebeck spin tunneling that occurs between a ferromagnetic electrode and a non-magnetic electrode across an oxide tunnel barrier. The figure is taken from Ref. [6].

Table 1.1. Crystal symmetry and lattice parameters of black phosphorus, WTe_2, and ReS_2.

	black phosphorus	WTe_2	ReS_2
Space group Schönflies notation	*Cmca* (No. 64) D_{2h}^{18}	*Pmn*2_1 (No. 31) C_{2v}^{7}	$P\bar{1}$ (No. 2) C_{i}^{1}
Lattice system	orthorhombic	orthorhombic	triclinic
a (Å)	3.314 (zigzag)	3.284 (//W chain)	6.461
b (Å)	10.478 (⊥ planes)	6.265 (⊥W chain)	6.377 (//Re chain)
c (Å)	4.376 (armchair)	14.043 (⊥ planes)	6.417
α (°)	90	90	105.1
β (°)	90	90	91.6
γ (°)	90	90	119.1
Z formula unit	8 (2-layer)	4 (2-layer)	4 (1-layer)
Density (g cm^{-3})	2.70	9.51	7.58
Reference	[13]	[47,48]	[49]

Table 1.2. Energy band gap of black phosphorus, WTe_2, and ReS_2 in bulk and monolayer.

	black phosphorus	WTe_2	ReS_2
E_g in bulk	0.3 eV, indirect	semi-metal	1.35 eV, direct
E_g in monolayer	2 eV, direct	semi-metal	1.43 eV, direct
Ref.	[7,13]	[8,50]	[9]

1.5. Reference

[1] D. G. Cahill, P. V Braun, G. Chen, D. R. Clarke, S. Fan, K. E. Goodson, P. Keblinski, W. P. King, G. D. Mahan, A. Majumdar, H. J. Maris, S. R. Phillpot, E. Pop, and L. Shi, *Appl. Phys. Rev.* **1**, 11305 (2014).

[2] D. Pines and P. Nozières, *The Theory of Quantum Liquids* (W.A. Benjamin, New York, 1966).

[3] E. Beaurepaire, J. C. Merle, A. Daunois, and J. Y. Bigot, *Phys. Rev. Lett.* **76**, 4250 (1996).

[4] K. Uchida, S. Takahashi, K. Harii, J. Ieda, W. Koshibae, K. Ando, S. Maekawa, and E. Saitoh, *Nature* **455**, 778 (2008).

[5] J. Kimling, G.-M. Choi, J. T. Brangham, T. Matalla-Wagner, T. Huebner, T. Kuschel, F. Yang, and D. G. Cahill, *Phys. Rev. Lett.* **118**, 57201 (2017).

[6] J. C. Le Breton, S. Sharma, H. Saito, S. Yuasa, and R. Jansen, *Nature* **475**, 82 (2011).

[7] L. Li, Y. Yu, G. J. Ye, Q. Ge, X. Ou, H. Wu, D. Feng, X. H. Chen, and Y. Zhang, *Nat Nano* **9**, 372 (2014).

[8] M. N. Ali, J. Xiong, S. Flynn, J. Tao, Q. D. Gibson, L. M. Schoop, T. Liang, N. Haldolaarachchige, M. Hirschberger, N. P. Ong, and R. J. Cava, *Nature* **514**, 205 (2014).

[9] S. Tongay, H. Sahin, C. Ko, A. Luce, W. Fan, K. Liu, J. Zhou, Y.-S. Huang, C.-H. Ho, J. Yan, D. F. Ogletree, S. Aloni, J. Ji, S. Li, J. Li, F. M. Peeters, and J. Wu, *Nat Commun* **5**, 3252 (2014).

[10] P. M. Ajayan, P. Kim, and K. Banerjee, *Phys. Today* **69**, 38 (2016).

[11] Y. Qi, P. G. Naumov, M. N. Ali, C. R. Rajamathi, W. Schnelle, O. Barkalov, M. Hanfland, S.-C. Wu, C. Shekhar, Y. Sun, V. Süß, M. Schmidt, U. Schwarz, E. Pippel, P. Werner, R. Hillebrand, T. Förster, E. Kampert, S. Parkin, R. J. Cava, C. Felser, B. Yan, and S. A. Medvedev, *Nat. Commun.* **7**, 11038 (2016).

[12] D. MacNeill, G. M. Stiehl, M. H. D. Guimaraes, R. A. Buhrman, J. Park, and D. C. Ralph, *Nat. Phys.* **13**, 300 (2017).

[13] Y. Takao, H. Asahina, and A. Morita, *J. Phys. Soc. Japan* **50**, 3362 (1981).

[14] C. Rovira and M. H. Whangbo, *Inorg. Chem.* **32**, 4094 (1993).

[15] J. H. Seol, I. Jo, A. L. Moore, L. Lindsay, Z. H. Aitken, M. T. Pettes, X. Li, Z. Yao, R. Huang, D. Broido, N. Mingo, R. S. Ruoff, and L. Shi, *Science (80-.).* **328**, 213 (2010).

[16] L. Lindsay, D. A. Broido, and N. Mingo, *Phys. Rev. B* **82**, 115427 (2010).

[17] A. A. Balandin, *Nat. Mater.* **10**, 569 (2011).

[18] I. Jo, M. T. Pettes, L. Lindsay, E. Ou, A. Weathers, A. L. Moore, Z. Yao, and L. Shi, *AIP Adv.* **5**, 53206 (2015).

[19] I. Jo, M. T. Pettes, E. Ou, W. Wu, and L. Shi, *Appl. Phys. Lett.* **104**, 201902 (2014).

[20] J. Liu, G.-M. Choi, and D. G. Cahill, *J. Appl. Phys.* **116**, 233107 (2014).

[21] A. Pisoni, J. Jacimovic, R. Gaál, B. Náfrádi, H. Berger, Z. Révay, and L. Forró, *Scr. Mater.* **114**, 48 (2016).

[22] D. G. Cahill, *Rev. Sci. Instrum.* **75**, 5119 (2004).

[23] J. P. Feser and D. G. Cahill, *Rev. Sci. Instrum.* **83**, 104901 (2012).

[24] J. P. Feser, J. Liu, and D. G. Cahill, *Rev. Sci. Instrum.* **85**, 104903 (2014).

[25] M. Bauer, A. Marienfeld, and M. Aeschlimann, *Prog. Surf. Sci.* **90**, 319 (2015).

[26] S. D. Brorson, J. G. Fujimoto, and E. P. Ippen, *Phys. Rev. Lett.* **59**, 1962 (1987).

[27] J. Hohlfeld, S.-S. Wellershoff, J. Güdde, U. Conrad, V. Jähnke, and E. Matthias, *Chem. Phys.* **251**, 237 (2000).

[28] M. Battiato, K. Carva, and P. M. Oppeneer, *Phys. Rev. Lett.* **105**, 027203 (2010).

[29] A. Kirilyuk, A. V Kimel, and T. Rasing, *Rev. Mod. Phys.* **82**, 2731 (2010).

[30] H. L. Wang, C. H. Du, Y. Pu, R. Adur, P. C. Hammel, and F. Y. Yang, *Phys. Rev. Lett.* **112**, 197201 (2014).

[31] P. F. Carcia, *J. Appl. Phys.* **631**, 5066 (1988).

[32] C. Lei, M. Bauer, K. Read, R. Tobey, Y. Liu, T. Popmintchev, M. M. Murnane, and H. C. Kapteyn, *Phys. Rev. B* **66**, 245420 (2002).

[33] Z. Lin, L. V. Zhigilei, and V. Celli, *Phys. Rev. B - Condens. Matter Mater. Phys.* **77**, 075133 (2008).

[34] V. P. Zhukov, E. V. Chulkov, and P. M. Echenique, *Phys. Rev. B - Condens. Matter Mater. Phys.* **73**, 125105 (2006).

[35] N. V. Volkenshtein, V. P. Dyakina, V. E. Startsev, and N. V Volkense~tein, *Scattering Mechanisms of Conduction Electrons in Transition Metals at Low Temperatures* (Wiley-Blackwell, 1973), pp. 9–42.

[36] S. Dutta, K. Sankaran, K. Moors, G. Pourtois, S. Van Elshocht, J. Bömmels, W. Vandervorst, Z. Tokei, and C. Adelmann, *J. Appl. Phys.* **122**, 025107 (2017).

[37] S. Yuasa and D. D. Djayaprawira, *J. Phys. D. Appl. Phys.* **40**, R337 (2007).

[38] S. Ikeda, J. Hayakawa, Y. Ashizawa, Y. M. Lee, K. Miura, H. Hasegawa, M. Tsunoda, F. Matsukura, and H. Ohno, *Appl. Phys. Lett.* **93**, 082508 (2008).

[39] S. Ikeda, K. Miura, H. Yamamoto, K. Mizunuma, H. D. Gan, M. Endo, S. Kanai, J. Hayakawa, F. Matsukura, and H. Ohno, *Nat. Mater.* **9**, 721 (2010).

[40] M. Walter, J. Walowski, V. Zbarsky, M. Münzenberg, M. Schäfers, D. Ebke, G. Reiss, A. Thomas, P. Peretzki, M. Seibt, J. S. Moodera, M. Czerner, M. Bachmann, and C. Heiliger, *Nat. Mater.* **10**, 742 (2011).

[41] T. Kuschel, M. Czerner, J. Walowski, A. Thomas, H. W. Schumacher, G. Reiss, C. Heiliger, and M. Münzenberg, *J. Phys. D. Appl. Phys.* **52**, 133001 (2018).

[42] A. Boehnke, U. Martens, C. Sterwerf, A. Niesen, T. Huebner, M. Von Der Ehe, M. Meinert, T. Kuschel, A. Thomas, C. Heiliger, M. Münzenberg, and G. Reiss, (n.d.).

[43] J. Zhang, M. Bachman, M. Czerner, and C. Heiliger, *Phys. Rev. Lett.* **115**, 037203 (2015).

[44] T. Huebner, U. Martens, J. Walowski, M. Münzenberg, A. Thomas, G. Reiss, and T. Kuschel, *J. Phys. D. Appl. Phys.* **51**, 224006 (2018).

[45] J. O. Island and A. Castellanos-Gomez, in *Semicond. Semimetals* (Elsevier, 2016), pp. 279–303.

[46] M. Kim, S. Han, J. H. Kim, J.-U. Lee, Z. Lee, and H. Cheong, *2D Mater.* **3**, 34004 (2016).

[47] B. F. Mentzen and M. J. Sienko, *Inorg. Chem.* **15**, 2198 (1976).

[48] W.-D. Kong, S.-F. Wu, P. Richard, C.-S. Lian, J.-T. Wang, C.-L. Yang, Y.-G. Shi, and H. Ding, *Appl. Phys. Lett.* **106**, 81906 (2015).

[49] H. H. Murray, S. P. Kelty, R. R. Chianelli, and C. S. Day, *Inorg. Chem.* **33**, 4418 (1994).

[50] E. Torun, H. Sahin, S. Cahangirov, A. Rubio, and F. M. Peeters, *J. Appl. Phys.* **119**, 74307 (2016).

CHAPTER 2
EXPERIMENTAL METHODS

2.1. Pump-probe optical setup

All of the measurements in this thesis are performed using TDTR systems in the Materials Research Laboratory at the University of Illinois at Urbana-Champaign. The schematic of the typical optical setup is shown in Figure 2.1 and 2.2. A Ti:Sapphire laser (Spectra-Physics, Tsunami) is pumped by a Nd:YVO laser (Spectra-Physics, Millenia) at 532 nm and generates a train of pulses at the repetition rate of 80 MHz with a wavelength centered at 785 nm and the FWHM of ≈10 nm. The pulses are split into two beams of orthogonal polarizations by a polarizing beam splitter. The vertical and horizontal polarizations are used as pump and probe beams, respectively. The pump and probe beams are further separated spectrally by using a long-pass filter and a short-pass filter, respectively. [1] I use an ultrasteep long-pass edge filter with edge wavelength at 786.7 nm and steepness of 1.6 nm (SEMROCK, LP02-785RE-25) for pump, and an ultrasteep short-pass edge filter with edge wavelength at 778.6 nm and steepeness of 3.9 nm (SEMROCK, SP01-785RU-25) for probe. The same short-pass-filter is placed before the photodiode to block the leaked pump beam.

The pump beam is modulated as a square wave at the frequency (f) of 1−10 MHz by an electro-optic modulator (Conoptics, model 350-160) and a function generator (SRS, DS345). The probe beam is modulated by a mechanical chopper at 200 Hz (SRS, SR540). Both of the beams co-propagate and are focused by a microscope objective lens onto a sample surface. The arrival time of the pump pulse relative to the probe pulse is adjusted by a linear motorized stage. A fiber ring-light is mounted onto the objective lens to illuminate the sample. The dark-field image of

the sample surface and the images of pump and probe beams can be observed by a CCD camera (Pixelink, PL-B952). The reflected probe beam is collected by a Si photodiode detector (Thorlabs, DET10A). The polarizing beam splitter (Newport, 10FC16PB.5) that reflects the pump and the short-pass-filter before the photodiode effectively block the leaked pump signal from reaching the Si photodiode. I use a non-polarizing beam splitter (Newport, 10BC17MB.2) for reflection and transmission of the probe beam.

The output of the photodiode is connected to a resonant filter, which is basically a LC circuit and for which the resonant frequency is the same as the modulation frequency (*f*). The signal is fed into a preamplifier (SRS, SR445A) for 5× gain, and a low-pass-filter of 30 MHz, which blocks odd harmonics of the modulation frequency. The signal is read by a RF lock-in amplifier (SRS, SR844) synchronized with the modulation frequency. The typical setting of the low-pass filter of the lock-in amplifier is 6 dB/octave and a time constant of 100 μs. The output of the lock-in amplifier is further demodulated by a software lock-in amplifier synchronized to the chopper frequency. The low-pass-filter of the software lock-in amplifier is 6 dB/octave with a time constant of 700 ms, which determines the bandwidth of the overall measurements and leads to a low noise level, i.e., 0.17 μV $Hz^{-1/2}$, predominantly from the electronics noise. The dwell time for each data point is 500 ms. The double modulation scheme effectively removes coherent pickup.

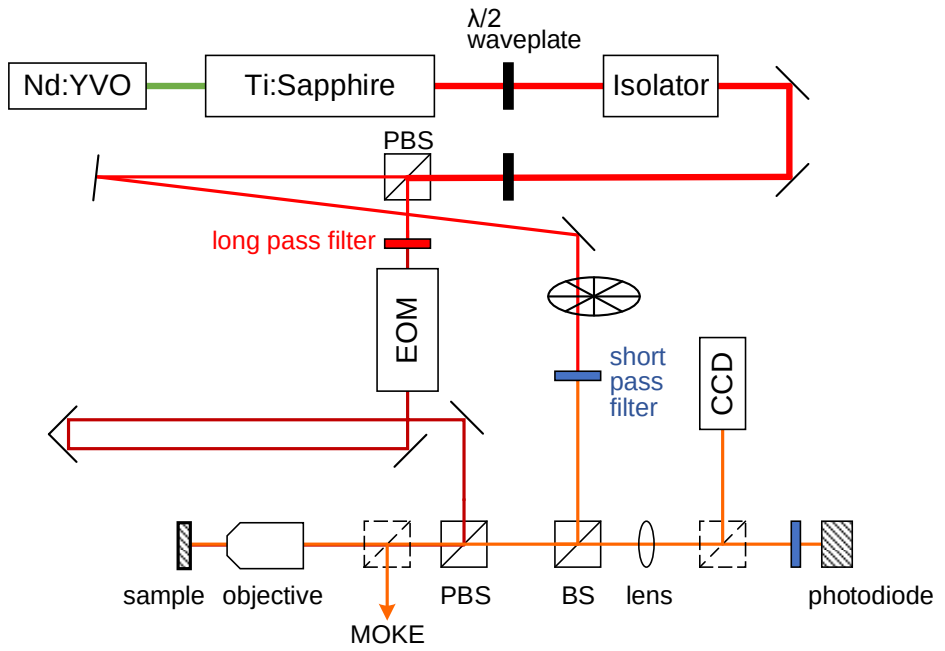

Figure 2.1. Schematic of TDTR system when pump and probe beams are co-aligned and incident on the top surface of a sample.

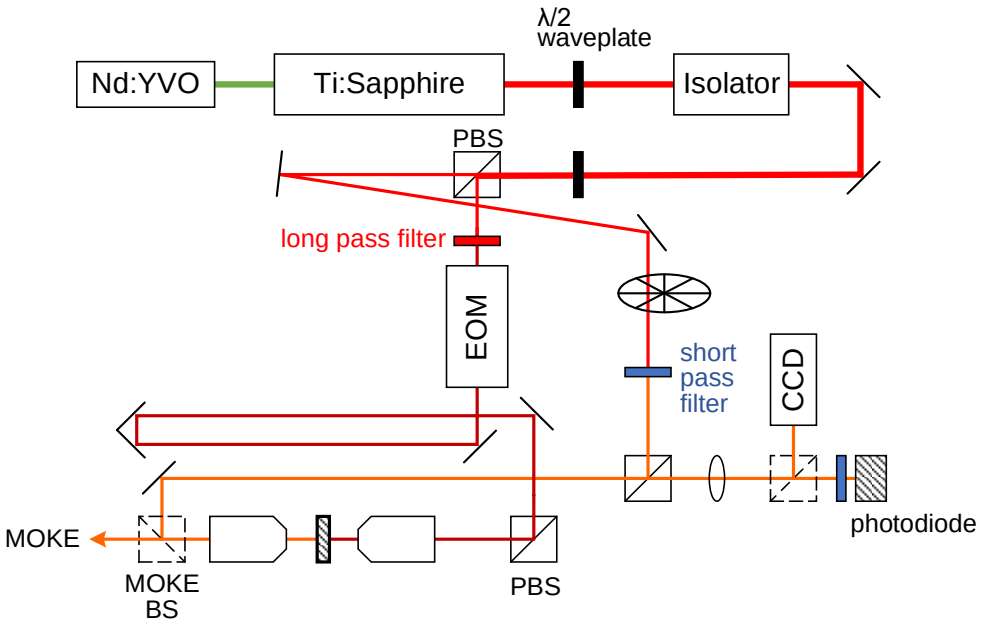

Figure 2.2. Schematic of TDTR system when pump and probe beams are co-aligned but incident on the opposite sides of a sample.

2.2. Time-domain thermoreflectance

The conventional geometry of TDTR measurement is to co-align the pump and probe beams on the same surface of a sample and collect the reflected probe beam as a function of delay time between the pump and probe pulses. A sample is typically coated with an optically thick layer of Al ≈ 80 nm thickness as Al has large a thermoreflectance coefficient, $dR/dT \approx 10^{-4}$, at wavelength of 785 nm. [2] In a small temperature excursion limit, i.e., $\Delta T < 10$ K, the reflectance change can be assumed to be linear with the temperature change of metal surface. Therefore, time-resolved measurements of a thermoreflectance signal, i.e., TDTR, have been extensively used for studying thermal transport properties of materials at nanoscale and of picosecond time scales. [3]

Figure 2.3 shows the temperature evolution at Al surface in time-domain due to the absorption of a series of pump pulses modulated at 5 MHz. In Fig. 2.3, only the first harmonic of the square wave is considered, which is the signal output of the RF lock-in amplifier. Both the in-phase and out-of-phase of the thermoreflectance signal change as a function of time delay. The analytic solution for surface temperature evolution is provided in Ref. [4] by solving a heat diffusion equation in a multilayer of cylindrical geometry in frequency domain. Ref. [4] also provides the expressions for in-phase and out-of-phase thermoreflectance signals weighted by Gaussian intensity profiles of pump and probe beams. The analytic solution for the heat diffusion equation is further extended to include in-plane anisotropy of materials. [5,6] For the analysis of TDTR data, I compare the ratio of the measured in-phase to out-of-phase signals with the ratio calculated from the model in Ref. [4].

In my experiments, the unknown parameters are usually the thermal conductivity (Λ) of a layer below the metal transducer and the interface thermal conductance (G) between the layer

and the metal transducer. Thus, I analyze the ratio at time delays between 100 ps and 4 ns, i.e., after heat propagates beyond the metal transducer. At this range of time delay, the dominant materials parameters are the thickness (h) and heat capacity (C) of the metal transducer. The sensitivities of the TDTR ratio to Λ and G of the layer below the transducer depend on the specific values and tend to be higher for smaller Λ and G.

The thickness of a metal transducer can be accurately determined by using picosecond acoustics. [7] The absorption of an optical pump pulse generates a longitudinal strain pulse into the through-plane direction, and the strain pulse returns to the surface after reflection at the bottom interface of a metal transducer. The thickness of a metal transducer can be estimated as the time interval of a round-trip divided by the known speed of sound (v_L).

For Al, the speed of sound is 6.42 nm ps^{-1} but I add 3 nm as a fudge factor to the thickness of Al estimated from picosecond acoustics and use as an input for the thermal model. This fudge factor has its origin in non-equilibrium between electrons and phonons in Al induced by the absorption of a laser pulse. Figure 2.4 shows TDTR signals across zero-time-delay for Al and NbV metal transducers. NbV is the transducer for beam-offset TDTR. [5] The zero-time-delay is defined as the midpoint of the maximum temperature-rise. In Fig. 2.4, while the midpoint of reflectance change (ΔR) in NbV matches with the zero-time-delay measured by a GaP photodiode, the midpoint of ΔR in Al is delayed by ≈0.4 ps, which corresponds to the thickness of ≈1.3 nm.

I attribute the delay in ΔR, and thus the temperature rise, of Al to delayed heating of phonons in Al: ΔR in Al is more affected by phonon temperature (ΔT_{ph}) than electron temperature (ΔT_e), since ΔR does not overshoot across the zero-time-delay. Heating of phonons in Al occurs slowly as electronic excitations tend to travel ballistically from the surface before

transferring energy to phonons. Ref. [8] estimates the travel distance of electronic excitations in Al as 40 nm, which is significantly longer than the optical absorption depth, ≈13 nm. Note that the electron-phonon coupling (g_{ep}) of Al is 4×10^{17} W m^{-3} K^{-1} [9] and significantly higher than g_{ep} of Au and Cu, i.e., 2×10^{16} and 7.5×10^{17} W m^{-3} K^{-1}. [10,11] Thus the slow heating of phonons in Al cannot be solely attributed to the low rate of electron-phonon energy exchange in Al. A delay in ΔR is not significant in NbV as the lifetimes of electronic excitations in transition metals are much shorter. [12]

The conventional geometry of TDTR can be modified for studying different heat transport properties. Feser *et al.* [5,6] proposed beam-offset TDTR and modified solutions for TDTR signals by taking account of in-plane anisotropy of materials. The beam-offset TDTR is a powerful technique that can measure in-plane thermal conductivity in any arbitrary orientation. The conventional TDTR employs a large beam size and a high modulation frequency to ensure one-dimensional heat transport in the through-plane direction. The combination of a smaller beam size and a low modulation frequency increases the in-plane thermal diffusion length to be comparable to the beam size, and the TDTR signal is significantly affected by in-plane heat transport. In beam-offset TDTR, the out-of-phase TDTR signal is collected as a function of beam-offset distance between the pump and probe at a fixed time delay, e.g., −100 ps. The in-phase TDTR signal at time delay of +20 ps at a high modulation frequency is also useful to measure the intensity profile of cross-correlation of the pump and probe pulse. I use the beam-offset TDTR to measure the three-dimensional thermal conductivity tensors of 2D materials, as presented in Chap. 3.

The probe beam path can also be changed so that the pump and probe beams are incident on the opposite sides of the sample, as shown in Fig. 2.2. In this geometry, the absorption layer

and the thermometer layer are separated. Thus, this geometry is useful to study non-equilibrium heat transport (Chap. 4) and to separately investigate the heat transport properties of layers above and below the thermometer layer (Chap. 5). The determination of zero-time-delay here is more challenging, and I provide the method employing the optical Kerr effect or inverse Faraday effect in the section. 2.3.

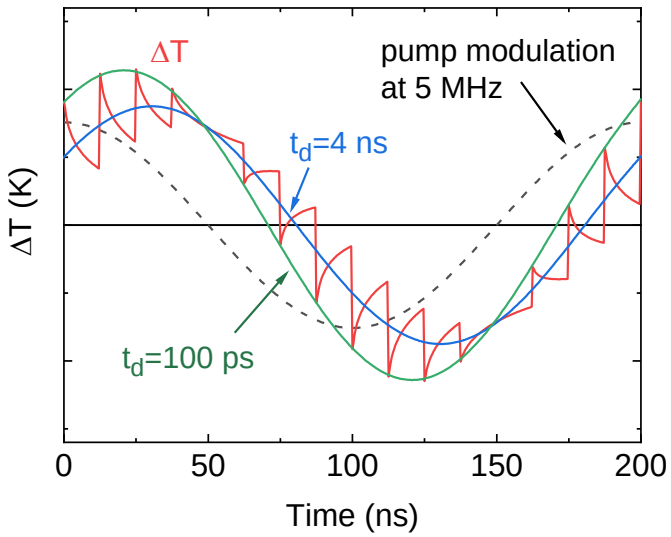

Figure 2.3. Temperature evolution of Al surface in time-domain due to a series of pump pulses modulated at *f*=5 MHz. The temperature response (red) due to only the first harmonic component of the square wave at *f* (dotted black) is shown. Blue and green lines are the thermoreflectance signal at time delay of 100 ps and 4 ns, respectively. The sample structure is Si with 500-nm-thick thermal oxide coated with 80-nm-thick Al.

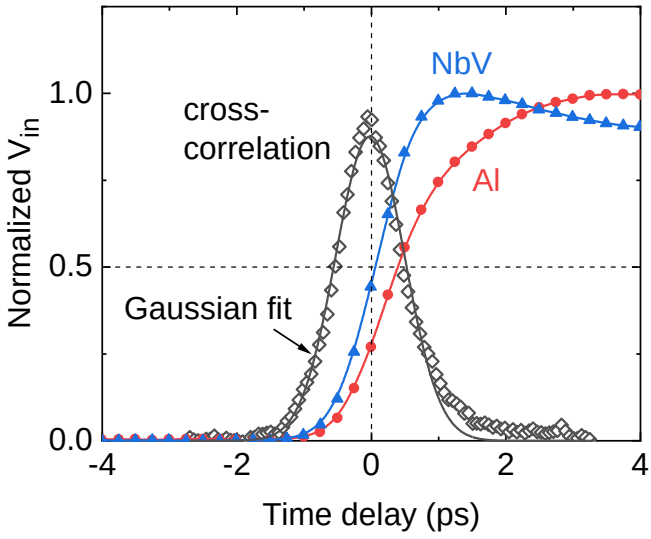

Figure 2.4. Normalized in-phase TDTR signal of NbV (blue) and Al (red) transducers on Si with 500-nm-thick thermal oxide across zero-time-delay measured using TDTR-2 system. The solid lines are for visual guidance only. Black symbol is the temporal profile of cross-correlation of pump and probe pulses measured by a GaP photodiode, and black line is the Gaussian fit.

2.3. Time-resolved linear and quadratic magneto-optical Kerr effects

Magneto-optical Kerr effect (MOKE) is a phenomenon that a polarization of light changes upon reflection from a magnetized medium. The interaction of light and a matter is described by a dielectric tensor. The dielectric tensor (ε) of a material having cubic symmetry with magnetization along the *z*-axis is shown in Eq. (2.1). The diagonal components are even functions of magnetization, and the off-diagonal component (ε_{xy}) is an odd function of magnetization. [13,14]

$$\varepsilon = \begin{pmatrix} \varepsilon_{xx} & \varepsilon_{xy} & 0 \\ -\varepsilon_{xy} & \varepsilon_{xx} & 0 \\ 0 & 0 & \varepsilon_{zz} \end{pmatrix} \tag{2.1}$$

The MOKE is categorized by the geometry of light propagation relative to the magnetization of a material: the polar MOKE is when a sample has out-of-plane magnetization and the light propagation vector has a component parallel to the magnetization direction. For a sample with in-plane magnetization, the longitudinal MOKE is when the projection of light propagation onto the sample surface is parallel to the in-plane magnetization; the transverse MOKE is when the projection is perpendicular to the magnetization. The polar, longitudinal, and transverse MOKE are caused by the off-diagonal components of the dielectric tensor and linear effects for a small perturbation limit of magnetization, i.e., the Kerr rotation changes a sign when a magnetization is reversed.

The complex Kerr rotation (Φ_K) has real and imaginary parts, which are referred to as Kerr rotation (θ_K) and ellipticity (ε_K), respectively, i.e., $\Phi_K = \theta_K + i\varepsilon_K$. You and Shin [13] showed that complex Kerr rotations of polar and longitudinal MOKE can be expressed by a single equation, which is a product of a geometry term for angle of incidence and the other term

dependent on optical constants of media. The polar MOKE shows a maximum Kerr rotation for normal incidence, which is as follows for an optically thick magnetic medium [13]:

$$\Phi_K = \frac{\varepsilon_{xy}}{(\varepsilon_{xx}-1)\sqrt{\varepsilon_{xx}}} \tag{2.2}$$

The complex Kerr rotation of the longitudinal MOKE requires an oblique incidence and is as follows for s- and p-polarizations [13]:

$$\Phi_K^s = \frac{\cos\theta_1 \tan\theta_2}{\cos(\theta_1-\theta_2)} \frac{\varepsilon_{xy}}{(\varepsilon_{xx}-1)\sqrt{\varepsilon_{xx}}} \tag{2.3}$$

$$\Phi_K^p = \frac{\cos\theta_1 \tan\theta_2}{\cos(\theta_1+\theta_2)} \frac{\varepsilon_{xy}}{(\varepsilon_{xx}-1)\sqrt{\varepsilon_{xx}}} \tag{2.4}$$

θ_1 and θ_2 are the complex angle of incidence in a medium 1, i.e., air with complex refractive index $\tilde{n}_1$=1, and the complex angle of refraction in a magnetized medium 2 ($\tilde{n}_2$), respectively. θ_1 and θ_2 are related through Snell's law. Eqs.(2.3-4) imply that the Kerr rotation of the longitudinal MOKE is much smaller than that of polar MOKE due to the geometry term.

The quadratic MOKE (QMOKE) or magnetic dichroism refers to Kerr rotation caused by different values of diagonal components of two in-plane axes. In addition to the longitudinal MOKE, QMOKE can be used to measure dynamics of in-plane magnetization. Moreover, QMOKE is present at normal incidence, on the contrary to the longitudinal MOKE. If I define the coordinate system such that the magnetization lies along *x*-axis and the light propagates along the *z*-axis, the dielectric tensor of a material in this coordinate system is below.

$$\varepsilon = \begin{pmatrix} \varepsilon_{xx} & 0 & 0 \\ 0 & \varepsilon_{zz} & \varepsilon_{yz} \\ 0 & -\varepsilon_{yz} & \varepsilon_{zz} \end{pmatrix} \tag{2.5}$$

The x and y components of electric field of light interact with a material via ε_{xx} and ε_{zz}, which are quadratic in magnetization. If α is the angle between the light polarization and magnetization, the Kerr rotation has a dependence of $\sin(2\alpha)$ and would be at maximum when $\alpha=\pm45°$. [14]

For samples with perpendicular magnetic anisotropy, I use polar MOKE to study the magnetization dynamics of out-of-plane magnetization. For samples with in-plane magnetic anisotropy, I use QMOKE. I note that the longitudinal MOKE has been frequently used to measure in-plane magnetization. However, the angle of incidence that I can conveniently use is limited by a numerical aperture of an objective lens and is about <10°. The small angle of incidence limits the Kerr rotation signal of the longitudinal MOKE in my setup, according to Eq. (2.3-4). For example, for the angle of incidence of 10° to an optically thick Co layer ($\tilde{n}$ =2.5+i4.8), the longitudinal Kerr rotation is smaller than the polar Kerr rotation by a factor of (0.015−i0.028). QMOKE has an advantage that the measurements can be performed at normal incidence. The conversion between polar MOKE and QMOKE in my experiments requires only the insertion of a half-wave-plate in the probe beam path, as will be discussed in detail below.

For time-resolved MOKE (TR-MOKE) measurement, only the detection scheme is different from the TDTR setup described in Sec. 2.1 and shown in Figure 2.5. The probe beam is initially horizontally polarized by the polarizing beam splitter, and the polarization is rotated as being reflected from a magnetized surface. The reflected probe beam is directed to the MOKE setup by a non-polarizing beam splitter (Thorlabs, BS014). The probe beam is then rotated by 45° by a half-wave-plate (Newport, 10RP02-28, quartz zero-order waveplate at 780 nm) whose fast axis is at 22.5° relative to the horizontal axis and split into the horizontally and vertically polarized components by a Wollaston prism. Without any Kerr rotation, the intensities of the two

polarization components should be equal. The small difference in the intensities inform the rotation of the polarization. The Kerr ellipticity can be measured by replacing the half-waveplate with a quarter waveplate (Thorlabs, WPQ05M-780, zero-order waveplate at 780 nm). The intensities of the two beams are detected by a balanced amplified photodetector (Thorlabs, PDB450C), which consists of two photodetectors and a transimpedance amplifier. The outputs of the two photodetectors are monitored by an audio-frequency (AF) lock-in amplifier referenced to the chopper frequency, 200 Hz. The differential voltage of the balanced detector is filtered by a band-pass-filter at 10.7 MHz and read by an RF lock-in amplifier referenced to the modulation frequency of the pump beam, 10.7 MHz. The noise level is 0.3 μrad/$\sqrt{Hz}$, regardless of the laser intensity. The TR-MOKE is taken as a difference of the MOKE signals at remanence of the opposite magnetic polarities.

To convert between the measured voltage in a lock-in amplifier and Kerr rotation, I perform a calibration: I rotate the polarization angle of the pump beam using a half-wave-plate and measure the voltage change in the RF lock-in. Note that the rotation of the polarization of the light is twice the rotation of the half-wave-plate. For this procedure, I block the probe and remove the short-pass-filter in front of the detector to pass only the pump. I obtain the proportionality factor as $dV_{RF}/d\theta \approx 10.6\ \mathrm{mV_{rms}\ deg^{-1}}$ for the pump intensity of $V_{A,AF} = 1.0\ \mathrm{V_{rms}}$, which is the monitor output of the balanced detector read by an AF lock-in. This calibration gives the conversion factor as below in Eq. (2.6). V_{RF} is the differential voltage read by the RF lock-in, and $V_{A,AF}$ is the monitor output read by the AF lock-in.

$$\Delta\theta_K = 1.65\frac{V_{RF}}{V_{A,AF}}\ \text{[rad]} \tag{2.6}$$

For a small fluence limit, a magnetization change can be assumed to be linear with a temperature change. Then the Kerr rotation of a magnetic layer can be employed as a thermometer. I obtain $(1/\theta_K)(d\theta_K/dT) \approx 10^{-3}$ K^{-1} for a 0.8-nm-thick Co layer sandwiched by two Pt layers.

For TR-QMOKE measurement, the polarization angles of both pump and probe beams relative to the in-plane magnetization should be chosen carefully. The magnetization following laser irradiation undergoes both precession due to the sudden change of the magneto-crystalline easy-axis to a new quasi-equilibrium direction and demagnetization. The expression for the resulting Kerr rotation, Φ_K, [14,15] as a function of the probe polarization angle relative to the magnetization (α) is given by Eq. (2.7) and in Figure 2.6.

$$\Phi_K(\alpha) = A_1 + A_2\cos(2\alpha) + B\sin(2\alpha) \tag{2.7}$$

The first term, independent of α, results from the polar MOKE detecting the out-of-plane component of the precessing magnetization; the second term results from the in-plane component of the precession. The precession motion corresponds to the rotation of the coordinate axes for eigen vectors of a dielectric tensor, and results in the dependence of $\cos(2\alpha)$; the third term is caused by demagnetization, which corresponds to the change in dielectric constants and gives the dependence of $\sin(2\alpha)$. Therefore, the demagnetization dynamics of the in-plane magnetization can be obtained by taking the difference of two measurements, $\Phi_K(+45°)-\Phi_K(-45°)$. The sum, $\Phi_K(+45°)+\Phi_K(-45°)$, gives the out-of-plane precession.

Moreover, I change the polarization direction of the pump to keep the pump and probe polarizations perpendicular to each other using a half-wave-plate added before the objective lens. This geometry minimizes the optical Kerr effect, [16,17] in which the linear polarization of a pump pulse creates transient linear birefringence that persists for a time-scale that is approximately equal to the momentum scattering time of the excited electrons. This form of the

optical Kerr effect has a similar physical origin as the inverse Faraday effect [17], in which a circular polarization of a laser pulse creates transient magnetization perpendicular to the sample plane.

In TR-QMOKE measurement, the pump and probe beams pass an additional half-wave-plate before the objective lens and are incident on the same side of a sample. The half-wave-plate is mounted on a motorized precision rotation mount. (Thorlabs, PRM1Z8) The fast axis of the half-wave-plate is at either 22.5° or 67.5° to set the polarizations of the pump and probe at +45° and –45°, or -45° and +45°, respectively. A magnetic field of ≈0.3 T at the sample position is applied from the side of a sample using a permanent magnet or an electromagnet during the measurement. The reflected probe is directed to the detection optics in the same manner as in TR-MOKE measurements (see Fig. 2.5) and does not pass through the half-wave-plate again after reflecting from the sample.

The zero-time-delay when the pump and probe are incident on the same surface of the samples can be determined using the GaP detector. The zero-time-delay when the pump and probe are incident on the opposite sides of the samples is determined via either the inverse Faraday effect or the optical Kerr effect [17], whichever has the a larger signal. For the inverse Faraday effect, the pump beam is circularly-polarized by a quarter-wave-plate and creates circular birefringence upon incidence on the sample surface. The lifetime of this birefringence is set by the momentum scattering time of the excited electrons. If the metal layer that the pump pulse is incident on is sufficiently optically transparent, the transient birefringence can be detected by the probe beam. The TR-MOKE signal then displays a narrow peak across zero-time-delay. (See Figure 2.7.) For thicker metal layers, the nonlinear response of the detector generated by the leaked pump in the absence of the optical filter is used to determine the zero-

time-delay. I correct the zero-time-delay if needed to take into account insertion or removal of various optical elements from the pump or probe beam paths. I estimate that the uncertainty in the position of zero-time-delay is approximately 0.1 ps.

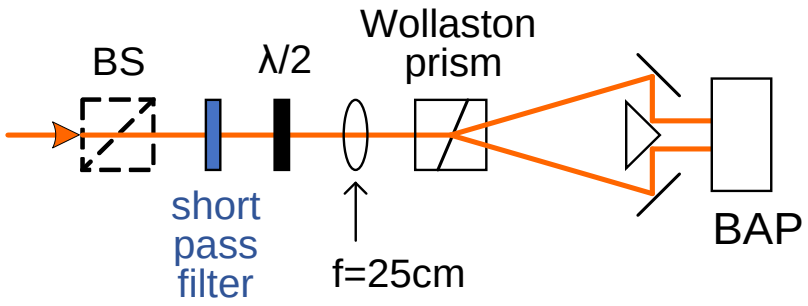

Figure 2.5. Detection scheme of magneto-optical Kerr effect. “BS” and “BAP” stand for (non-polarizing) beam splitter and balanced amplified photodiode, respectively. The non-polarizing beam splitter is placed after the microscope objective lens to direct the reflected probe beam into the MOKE detector.

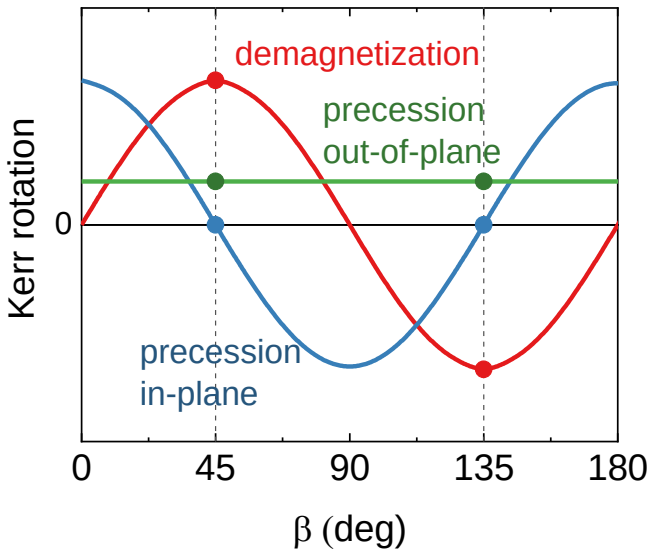

Figure 2.6. Quadratic magneto-optical Kerr effect as a function of the polarization angle of probe beam relative to the in-plane magnetization. QMOKE signal includes the out-of-plane (green) and in-plane (blue) components of precession motion of magnetization, and demagnetization (red). The magnitudes are not drawn in scale.

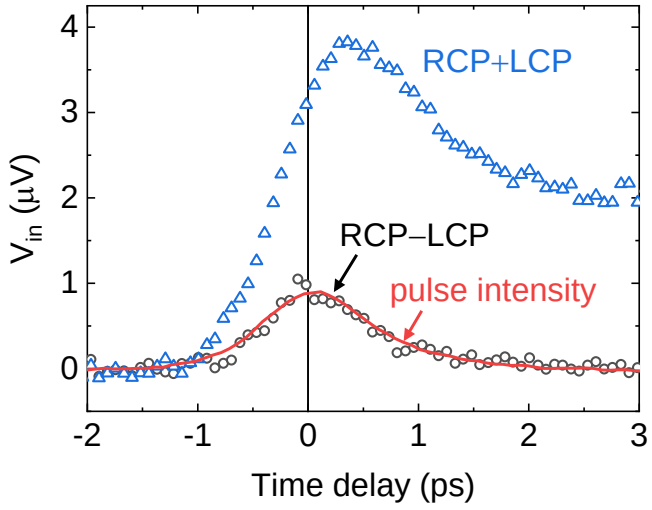

Figure 2.7. Determination of zero-time-delay via inverse Faraday effect. Open symbols are TR-MOKE data of Pt(16)/Co(0.8)/Pt(24)/sapphire when a circularly polarized pump beam is incident on Pt(24) surface, and a linearly polarized probe beam is incident on Pt(16) surface. The sum of TR-MOKE data for right- and left-circularly polarized pump beams ("RCP+LCP", blue symbol) represents magnetization dynamics in Co, and the difference ("RCP−LCP", black symbol) represents the inverse Faraday effect. Red solid line is the scaled intensity of a correlated pump-probe pulse measured via two-photon absorption.

2.4. Reference

[1] K. Kang, Y. K. Koh, C. Chiritescu, X. Zheng, and D. G. Cahill, *Rev. Sci. Instrum.* **79**, 114901 (2008).

[2] R. B. Wilson, B. A. Apgar, L. W. Martin, and D. G. Cahill, *Opt. Express* **20**, 28829 (2012).

[3] D. G. Cahill, P. V Braun, G. Chen, D. R. Clarke, S. Fan, K. E. Goodson, P. Keblinski, W. P. King, G. D. Mahan, A. Majumdar, H. J. Maris, S. R. Phillpot, E. Pop, and L. Shi, *Appl. Phys. Rev.* **1**, 11305 (2014).

[4] D. G. Cahill, *Rev. Sci. Instrum.* **75**, 5119 (2004).

[5] J. P. Feser and D. G. Cahill, *Rev. Sci. Instrum.* **83**, 104901 (2012).

[6] J. P. Feser, J. Liu, and D. G. Cahill, *Rev. Sci. Instrum.* **85**, 104903 (2014).

[7] G. T. Hohensee, W.-P. Hsieh, M. D. Losego, and D. G. Cahill, *Rev. Sci. Instrum.* **83**, 114902 (2012).

[8] Y. Li, Q. Miao, A. V Nurmikko, and H. J. Maris, *J. Appl. Phys.* **105**, 83516 (2009).

[9] G. Tas and H. J. Maris, *Phys. Rev. B* **49**, 15046 (1994).

[10] W. Wang and D. G. Cahill, *Phys. Rev. Lett.* **109**, 175503 (2012).

[11] G.-M. Choi, R. B. Wilson, and D. G. Cahill, *Phys. Rev. B* **89**, 64307 (2014).

[12] M. Bauer, A. Marienfeld, and M. Aeschlimann, *Prog. Surf. Sci.* **90**, 319 (2015).

[13] C.-Y. You and S.-C. Shin, *J. Appl. Phys.* **84**, 541 (1998).

[14] N. Tesařová, T. Ostatnický, V. Novák, K. Olejník, J. Šubrt, H. Reichlová, C. T. Ellis, A. Mukherjee, J. Lee, G. M. Sipahi, J. Sinova, J. Hamrle, T. Jungwirth, P. Němec, J. Černe, and K. Výborný, *Phys. Rev. B* **89**, 085203 (2014).

[15] N. Tesařová, P. Němec, E. Rozkotová, J. Zemen, T. Janda, D. Butkovičová, F. Trojánek, K. Olejník, V. Novák, P. Malý, and T. Jungwirth, *Nat. Photonics* **7**, 492 (2013).

[16] R. Wilks, N. D. Hughes, and R. J. Hicken, *J. Phys. Condens. Matter* **15**, 5129 (2003).

[17] R. Wilks and R. J. Hicken, *J. Phys. Condens. Matter* **16**, 4607 (2004).

CHAPTER 3
THERMAL TRANSPORT IN TWO-DIMENSIONAL MATERIALS WITH IN-PLANE ANISOTROPY

Parts of this chapter were published in "Anisotropic Thermal Conductivity of Exfoliated Black Phosphorus," H. Jang, J. D. Wood, C. R. Ryder, M. C. Hersam, and D. G. Cahill, *Advanced Materials* **27**, 8017 (2015), "Direct Synthesis of Large-Scale WTe_2 Thin Films with Low Thermal Conductivity," Y. Zhou, H. Jang, J. M. Woods, Y. Xie, P. Kumaravadivel, G. A. Pan, J. Liu, Y. Liu, D. G. Cahill, and J. J. Cha, *Advanced Functional Materials*, **27**, 1605928 (2017), and "3D Anisotropic Thermal Conductivity of Exfoliated Rhenium Disulfide," H. Jang, J. D. Wood, C. R. Ryder, M. C. Hersam, and D. G. Cahill, *Advanced Materials*, **29**, 1700650 (2017).

3.1. Sample characterization

The samples for TDTR measurements are prepared by mechanical exfoliation onto Si wafers with native oxide of ≈2 nm thickness or thermal oxide of ≈500 nm thickness. The exfoliated BP and ReS_2 flakes are provided from Prof. Hersam's group at Northwestern University. These flakes are encapsulated with an AlO_x passivation layer of ≈2.6 nm thickness by atomic layer deposition after exfoliation, as described in Ref. [7]. The single crystals of WTe_2 are provided from Prof. Cha's group at Yale University. The height profile and topography of the exfoliated flakes are confirmed by atomic force microscopy (AFM). Before performing TDTR measurements, I coat the flakes with a 70-nm thick transducer of either Al or NbV. Figure 3.1 shows an optical micrograph and AFM image of an exfoliated ReS_2 of 203 nm thickness.

The crystalline orientation of the exfoliated flakes can be determined by using angle-resolved polarized Raman spectroscopy. Figure 3.2 shows the Raman spectra of BP as a function of sample rotation angle. BP has D_{2h}^{18} point group symmetry and six Raman-active vibration modes. [8,9] For incident and scattered light propagating normal to the planes of the flakes, the selection rules permit observation of three modes at 363 cm^{-1} (A_g^1), 440 cm^{-1} (B_{2g}), and 467 cm^{-1} (A_g^2). The A_g^1, B_{2g}, and A_g^2 intensities depend on the polarization direction in the *a*-*c* plane and can be used to determine the crystal orientation. Further, I note that the Raman intensity of the Si TO phonon (~521 cm^{-1}) varies with sample orientation, as both the intrinsic Si Raman tensor and BP's optical constants are angle-dependent.

In Fig. 3.2(b), I subtract polynomial baselines from the spectra in Fig. 3.2(a), Lorentzian fit them, and normalize the peak intensity values. According to Wu *et al*. [9], the B_{2g} peak intensity is maximum when the scattered polarization is halfway between the zigzag and armchair direction. Conversely, the A_g^2 peak intensity is maximum when the polarization is along the armchair direction.

For orienting the ReS_2 flakes, the Raman measurements are acquired by orienting polarizers of the excitation laser and detector parallel to each other and rotating the sample in fifteen-degree increments. The intensities of five modes, namely mode *I* to *V*, located at approximately 131–212 cm^{-1}, are measured to fluctuate in intensity with sample rotation. The intensity of mode *V*, as determined by a Gaussian fit, is fit to the polarization dependence described in Ref. [10]. The main axis (containing the maxima) of the polarization dependence of mode *V* is assigned to the Re chain direction. [5,10]

For WTe_2, I do not collect the angle-resolved Raman spectra. Instead, I perform the two-dimensional mapping of the beam-offset TDTR measurement to see the orientation-dependent in-plane thermal conductivity. Prof. Cha's group also prepared polycrystalline films of WTe_2 via chemical vapor deposition (CVD). The details of sample preparation is provided in Ref. [6]. The polycrystalline samples are also measured using TDTR and compared with single crystalline exfoliated flakes.

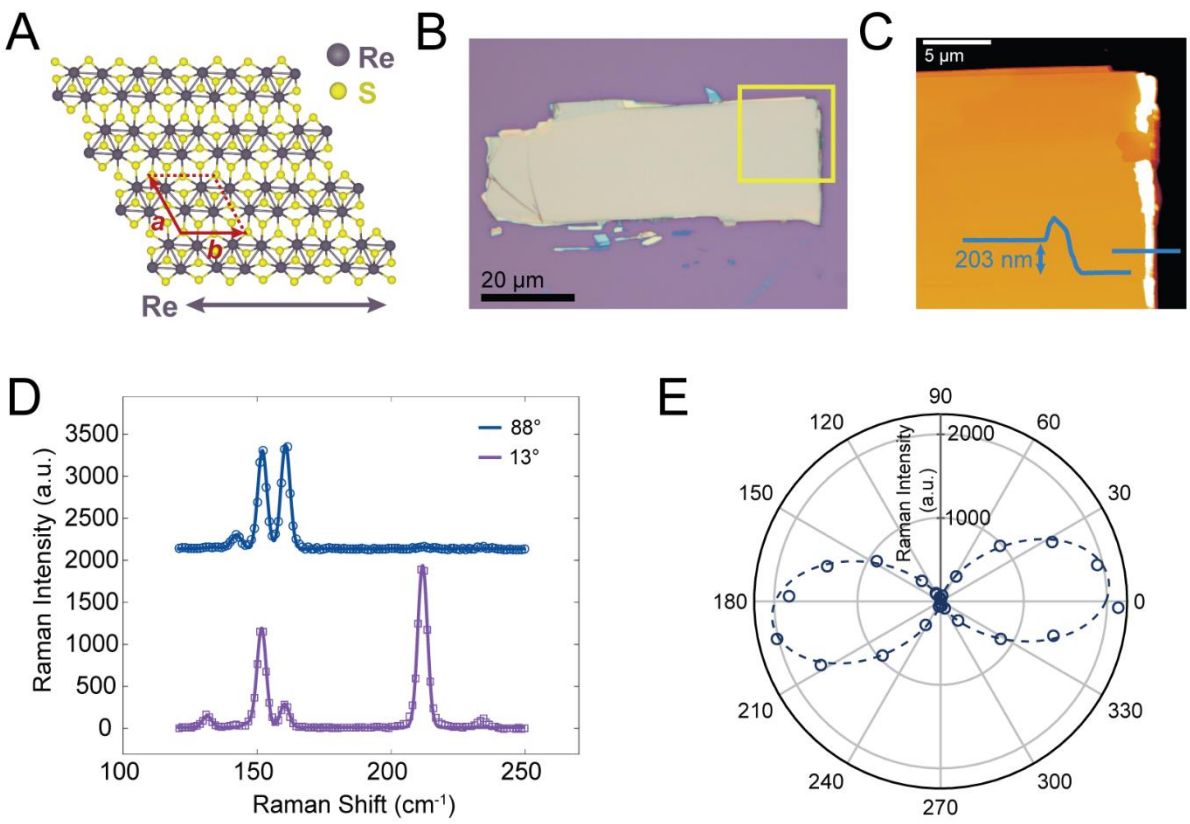

Figure 3.1. Characterization of exfoliated ReS_2. (a) Anisotropic crystal structure of ReS_2 showing the basal plane of the distorted 1T phase. Rhenium atoms are depicted as gray and sulfur atoms as yellow. The unit cell vectors *a* and *b* are shown in red, the unit cell is shown in dashed red, and the Re chain direction (along *b*) is shown as a gray arrow. (b) Optical micrograph of an exfoliated ReS_2 flake with large lateral dimensions on a SiO_2 substrate. The yellow box indicates the area characterized by AFM. (c) AFM of a 20 μm region of the ReS_2 flake with inset step height profile. Flake height is 203 nm. (d) Polarized Raman spectroscopy of the ReS_2 flake in (n), acquired in parallel configuration showing modes I–V at 131, 142, 152, 161, and 212 cm^{-1}, respectively. The bottom spectrum was taken near the orientation where the mode V had maximum intensity and the top spectrum near the mode V minimum intensity. Data is in open symbols while the solid lines are the fits. (e) Plot of the polarized Raman intensity of mode V with varying sample rotation. The data has been rotated so that 0 degrees and 90 degrees correspond to the horizontal and vertical directions of (b), respectively. Open circles are the intensities determined from a Gaussian fit while the dashed line is the fit of the polarization dependence. The figure is on the courtesy of Chris Ryder in Prof. Hersam's group.

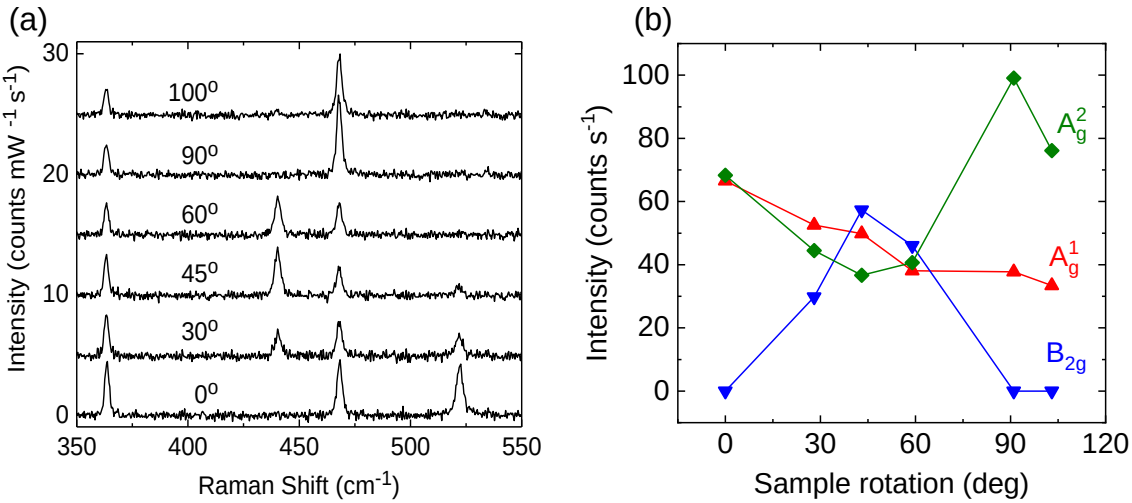

Figure 3.2. (a) Angle-dependent Raman point spectra of BP. Spectra taken with parallel polarization of the incident and backscattered light, and spectra normalized and offset for clarity. The BP flake was rotated with respect to the polarization of the light in the *a*-*c* plane. The *y*-axis is the spectral CCD readout, divided by the incident laser power in mW and the integration time in s. (b) Normalized intensities of the three Raman peaks of a BP flake as a function of sample rotation angle with parallel polarization of the incident and backscattered light. The BP flake was rotated in the *a*-*c* plane with respect to the polarization of the light. The rotation angles of 0° and 90° correspond to the zigzag and the armchair directions, respectively.

3.2. Through-plane thermal conductivity

I measure the thermal conductivity in the through-plane direction using time-domain thermoreflectance (TDTR) of the conventional geometry, i.e., pump and probe beams are co-aligne, as shown in Figure 3.3. For the through-plane analysis, I compare the ratio of the in-phase voltage (V_{in}) to the out-of-phase voltage (V_{out}) of the measured TDTR signals with the ratio calculated from a thermal model [7]. The modeling requires material parameters such as heat capacity (C), thickness (h), and thermal conductivity (Λ). I use the heat capacities that are experimentally determined in prior work: 1.87, 1.68, and 2.06 J K^{-1} cm^{-3} for BP [8], WTe_2 [9], and ReS_2 [10], respectively. The thickness of the metal transducer is determined by picosecond acoustics (See Fig. 3.3(a)). The remaining free parameters are the through-plane thermal conductivity of the flakes (Λ_z), the thermal conductance of the interface with a metal transducer (G_1), and the thermal conductance of the interface with a substrate (G_2). I use two modulation frequencies (f), 9−10 MHz and 1 MHz, to vary the penetration depth of the thermal waves into the flake, ≈100 nm and ≈300 nm, respectively. I include the in-plane thermal conductivity of the 2D materials in the thermal model, although its effect is significant only at f =1 MHz and a smaller $1/e^2$ beam radius of 2.7 μm. Therefore, I perform the through-plane analysis iteratively with the in-plane analysis of the beam-offset TDTR. Fig. 3.3(b) shows an example TDTR data of the 55-nm-thick BP flake with NbV measured at f = 9.1 MHz and fits to the thermal model.

Rapid heating of the metal transducer by the pump optical pulses generates a longitudinal acoustic pulse. Reflections of this acoustic pulse that return to the surface, i.e., acoustic echoes, can be used to measure sound velocities if the layer thickness is known. Similarly, acoustic echoes can be used to measure the layer thickness if the sound velocity is known. The sign of the echo depends on the acoustic impedance, $Z = \rho v_L$, where ρ is the mass density and v_L the

longitudinal sound velocity of the two materials on the opposing sides of an interface. If the medium underneath has a smaller Z, then the acoustic echo undergoes a π-phase shift. [11]

Picosecond acoustics data for a 55-nm-thick BP sample on Si with native oxide and coated with NbV are compared to those for the substrate in Figure 3.3(a). The first upward echo at 28 ps that repeats periodically is a combination of the reflections from the NbV/AlO_x and AlO_x/BP interfaces having a similarly large contrast in Z (see Table 3.1). When I repeat the measurement on a region of the substrate adjacent to the BP sample, the first peak appears ≈0.5 ps earlier than in the flake, which is reflected predominantly from the NbV/AlO_x interface. This is due to the larger Z ratio of the NbV/AlO_x interface, as compared to that of the AlO_x/Si interface. The native oxide of Si, SiO_x, generally has a weak effect on picosecond acoustics. The echo at 50 ps is the reflection at the BP/substrate interface. Although the acoustic impedance of BP is smaller than Si, I do not expect an intimately bonded interface between BP and Si, as there is finite roughness for both the exfoliated BP surface and Si substrate.

The longitudinal speeds of sound of BP, WTe_2, and ReS_2 are determined from the picosecond acoustics measurements and summarized in Table 3.1. All three materials do not show a distinct thickness-dependency of v_L. The elastic constant in the through-plane direction, C_{33}, can also be determined from the longitudinal speed of sound as $C_{33} = \rho v_L^2$.

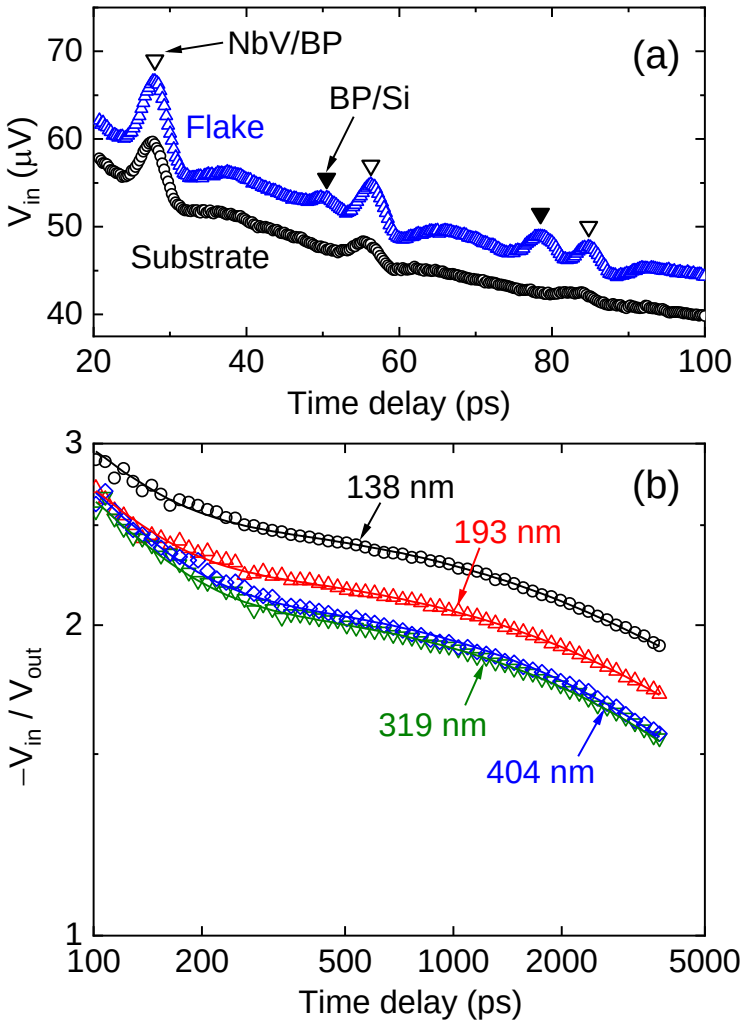

Figure 3.3. Through-plane measurements of the BP flakes coated with the NbV film. (a) Picosecond acoustics data for a 55 nm thick BP flake. (b) TDTR data for the BP flakes of 138–404 nm thicknesses. The open symbols are the measurement data at 9.1 MHz and the solid lines are the best fits to a thermal model used to determine the through-plane thermal conductivity.

materials	ρ **(g cm^{-3})**	v_L **(nm ps^{-1})**	$Z = \rho v_L$	$C_{33} = \rho v_L^2$
black phosphorus	2.7	4.76±0.16	13	61±4
WTe_2	9.5	2.00±0.12	19	38±5
ReS_2 [a]	7.7	2.36±0.14	18	43±5
Al	2.7	6.42	17	111
NbV [16]	7.4	5.4	40	216
AlO_x [17]	2.5	8.7	22	189
SiO_x [18]	2.2	5.97	13	78
Si [18]	2.33	8.48	20	168

Table 3.1. Elastic properties of materials in TDTR measurements. ρ, v_L, Z, and C_{33} are the density, longitudinal speed of sound, and acoustic impedance, and elastic modulus, respectively.

a. For ReS_2, the unit cell is triclinic, and the through-plane direction does not correspond to the crystalline axis. The reported values here are the "effective" values along the through-plane direction.

3.3. In-plane thermal conductivity

An example of beam-offset TDTR measurement is shown for a 384-nm-thick BP flake coated with NbV at f=1.6 MHz in Figure 3.4. I fit the TDTR data to Gaussian curves and use the FWHM values for quantitative analysis. The FWHM of V_{out} in the zigzag direction, 6.06±0.04 μm, is larger than that of the armchair direction, 5.32±0.03 μm, and both are significantly larger than the width of the laser beam profile, 4.17±0.06 μm. Although these FWHM data of the two orthogonal directions can be analyzed using a thermal model [12] that takes account of the 3D thermal conductivity tensor for BP, this 3D model requires multi-dimensional integrations that need significant computational time.

To expedite the analysis, I first constrain the range of possible thermal conductivities using a 2D anisotropy model that assumes an in-plane symmetry, [15] but I allow the in-plane thermal conductivity to vary depending on the beam-offset direction. Analysis based on the 2D model tends to exaggerate the in-plane anisotropy, due to the incorrect assumption that the in-plane temperature fields are isotropic. For the BP data, the difference between fits to the 2D and 3D models are ≈10%; thus, the 2D model can be used as a useful tool for constraining the values in the thermal conductivities prior to the 3D model's use. All the reported thermal conductivities are derived from the TDTR data using the full 3D model.

To aid in the experimental design and evaluate the propagation of errors, I analyze the sensitivity of the beam-offset FWHM to various experimental parameters. [16] I define the sensitivity parameter for the FWHM as

$$\Sigma(\alpha) = \frac{\partial[\ln(FWHM)]}{\partial[\ln(\alpha)]} \tag{3.1}$$

The sensitivities to the experimental parameters over a range of the in-plane thermal conductivities calculated by the 2D anisotropy model are plotted in Figure 3.5. The parameter h

is the thickness of the flake. The FWHM is most sensitive to the beam size (*w),*which can be determined precisely during beam-offset measurements. The uncertainty in the in-plane thermal conductivity (Λ_r) originating from a parameter α can be estimated as $\delta(\alpha)\cdot\Sigma(\alpha)/\Sigma(\Lambda_r)$, where $\delta(\alpha)$ is the fractional error of α. Error propagation from uncertainties in w to uncertainties in the in-plane thermal conductivity produces an overall error of ≈10%. The second largest error arises from the determination of thickness (h) of flakes from AFM measurement; the thickness uncertainty is especially important in the case of higher thermal conductivity. Ultimately, I find a 5% uncertainty in the thickness from ten fitted height profiles from AFM, leading to an uncertainty of ≈3% in the in-plane thermal conductivity. The sensitivity to the in-plane thermal conductivity, $\Sigma(\Lambda_r)$, is maximized when the FWHM of V_{out} is larger but comparable to the beam width. (See Fig. 3.4) The $\Sigma(\Lambda_r)$ is maximum at approximately $\Lambda_r = 30$ W m^{-1} K^{-1} for $w = 1$ μm; $w = 2.5$ μm is a better choice for $50 < \Lambda_r < 100$ W m^{-1} K^{-1}.

I use the $1/e^2$ beam radius of 2.7 μm using a 20× objective lens for BP and ReS_2 flakes and 1.1 μm using 50× lens for WTe_2 for the in-plane thermal conductivity measurements. The BP and ReS_2 flakes are mounted on a rotation stage. The BP flakes are oriented such that either zigzag or armchair axes is parallel to the beam-offset direction. The ReS_2 flakes are oriented along the Re-chain direction. The measurement results of a ReS_2 flake of 203 nm thickness is shown in Figure 3.6. For WTe_2, instead of aligning the flakes along certain directions, I perform a two-dimensional beam-offset scan, as shown in Figure 3.7. The laser beam is circular on the sample surface, i.e., the horizontal and the vertical radii differ by < 3%, and the TDTR signals of the sample are also circular, which means the in-plane thermal conductivity of the sample is isotropic on a bulk level.

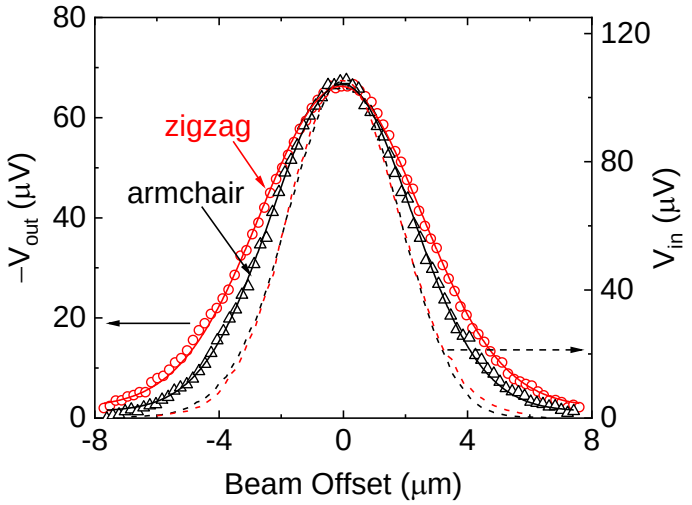

Figure 3.4. In-plane measurements (open symbol) and the Gaussian fitting curves (solid line) of the 384 nm thick BP flake for the zigzag (red) and the armchair (black) directions at low modulation frequency of 1.6 MHz and negative time delay of −50 ps. The dashed lines show the laser beam profiles for each direction determined from the in-phase signal at 9.1 MHz. The $1/e^2$ radius of the pump and probe laser beams is ≈2.5 μm.

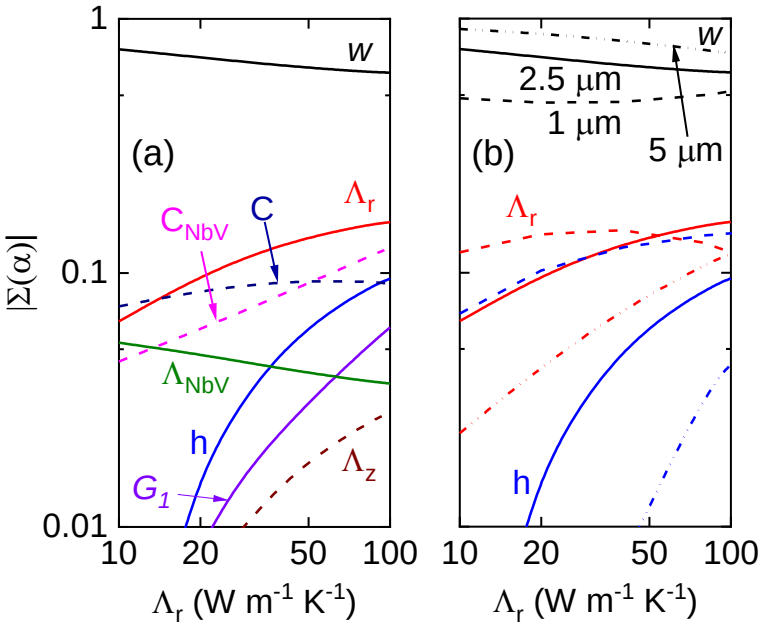

Figure 3.5. Sensitivity of FWHM of the out-of-phase thermoreflectance signal (V_{out}) to the experimental parameters for the 552 nm thick BP flake, calculated by the 2D anisotropy model at 1.6 MHz and time delay of −50 ps. (a) The sensitivities at the beam size of w ≈ 2.5 μm. Dashed lines are sensitivities having negative values. (b) The sensitivities of the major parameters at the different beam radii: 1 μm (dashed), 2.5 μm (solid), and 5 μm (dashed-dotted).

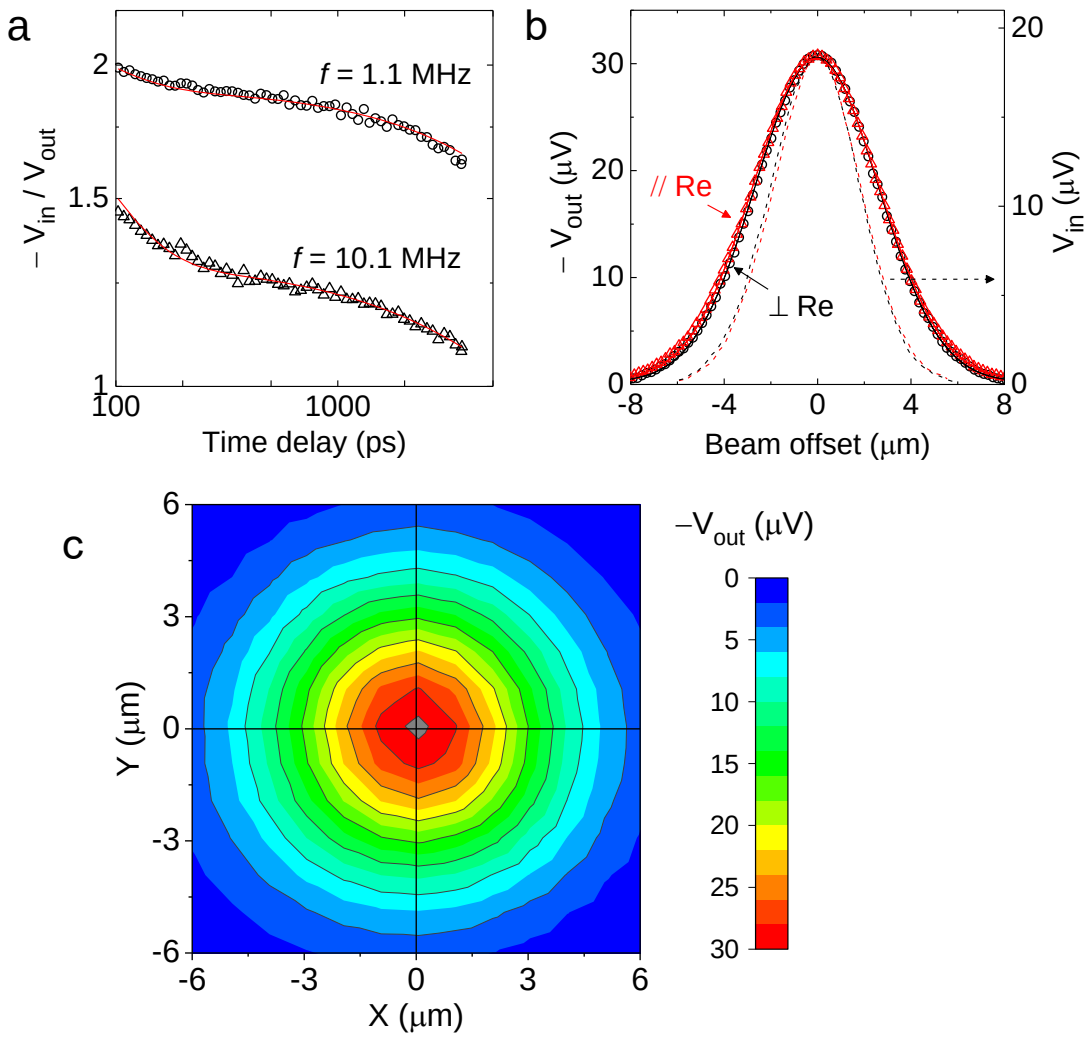

Figure 3.6. Thermal conductivity measurement of the 203 nm thick ReS_2 flake, coated with a NbV transducer. (a) Through-plane TDTR data at two modulation frequencies. The solid lines are the best-fit. (b) In-plane TDTR data at f = 1.1 MHz and time delay of –50 ps. The dashed lines are the intensity profile of the laser beam. (c) 2D beam-offset scan of the TDTR signal.

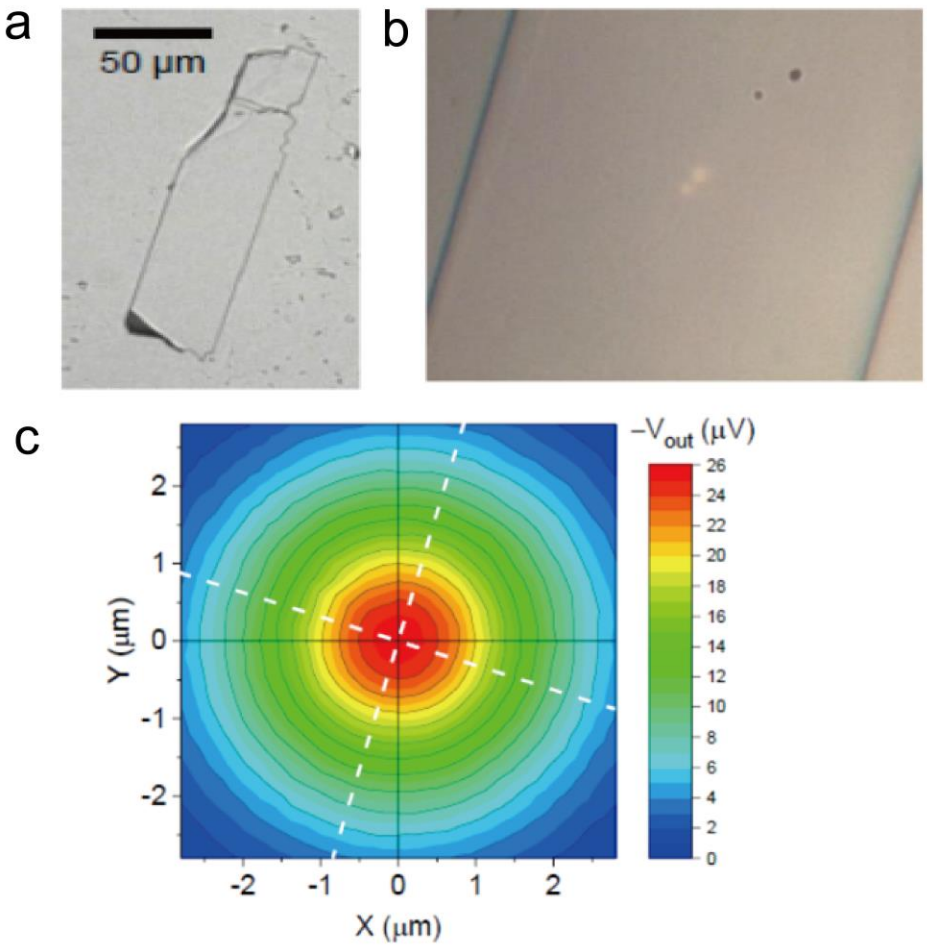

Figure 3.7. The beam-offset TDTR measurements on the 540-nm-thick single crystalline flake. (a) The optical microscope image of the NbV-coated flake, (b) the image taken during TDTR showing the orientation of the flake, and (c) two-dimensional beam-offset scan on the flake. The white dotted lines are drawn as parallel to the sharp edge of the flake.

3.4. Discussion

Figure 3.8 shows the thermal conductivity of BP as a function of flake thickness. I note that the beam-offset TDTR measurements are for thicker (h > 300 nm) BP flakes, versus the less sensitive conventional TDTR measurements (h > 100 nm) for through-plane BP thermal conductivity determinations. As expected from the weak van der Waals bonding between layers compared to the strong covalent bonding within layers, the through-plane thermal conductivity is lower than the in-plane thermal conductivity by an order of magnitude for the exfoliated flakes. The fitted thermal conductivities are 62–86 W m^{-1} K^{-1} for the zigzag direction and 26–34 W m^{-1} K^{-1} for the armchair direction. Variance in the determined values stems from the experimental uncertainty and marginal BP oxidation from changing relative humidity in sample preparation. While strongly anisotropic in the plane, the thermal conductivities do not show a statistically significant trend over the range of flake thicknesses investigated.

Anisotropic and in-plane thermal conductivities of BP have been predicted for single-layer BP (i.e., phosphorene) from first principles calculations for the phonon dispersions and three-phonon scattering rates. [17–20] Therein, the phosphorene thickness is set to the inter-layer (b axis) separation of 5.25 Å. [20] Additionally, Luo *et al.* [21] reported the thermal conductivity for few-layer BP, where they reconciled the thickness dependence of the thermal conductivity through a boundary scattering term to the intrinsic three-phonon scattering rate. Due to the large thickness of the BP flakes I studied in this work, surface scattering should be less significant in my experiments than in those of Ref. [21]. Further, the BP flakes of this work are encapsulated by both AlO_x and NbV, making ambient oxidation [1] or photodegradation [22] less significant, giving us an intrinsic measurement of BP's anisotropic thermal conductivities.

The thermal conductivity of the exfoliated WTe_2 flakes is shown in Figure 3.9. The in-plane thermal conductivity is isotropic, at (15±3) W m^{-1} K^{-1}, within the experimental uncertainty, in contrast to the atomic arrangement of low symmetry in the layers. These results are in accordance with the theoretical prediction [23] of the lattice thermal conductivity, 10 (*a*-axis) and 11 W m^{-1} K^{-1} (*b*-axis), and 1.0 W m^{-1} K^{-1} (*c*-axis), and higher than the estimated in-plane thermal conductivity, 2.5 to 11 W m^{-1} K^{-1}, for few-layer WTe_2 flakes. [24] Although the orientation-dependent in-plane electrical resistivity has not been reported for WTe_2, the electronic contribution to the thermal conductivity is expected to be small ≈1.0 W m^{-1} K^{-1} (assuming the Lorentz number as 2.44 ×10^{-8} W Ω K^{-2}).

The thermal conductivity of ReS_2 is shown in Figure 3.10. Both the in-plane and the through-plane thermal conductivities are insensitive to the thickness of the flakes in the regime studied here, i.e., from 60 to 450 nm. The through-plane thermal conductivity is notably low and independent of thickness at 0.55 W m^{-1} K^{-1} within experimental uncertainty. This low through-plane thermal conductivity can be attributed to the extremely weak interlayer coupling strength of ReS_2 [25] which leads to reduced group velocity of lattice vibrations along the through-thickness direction. The lack of sensitivity to flake thickness suggests that the mean free paths (MFPs) of phonons in ReS_2 are less than the thicknesses of the flakes in this study, which were greater than 60 nm. In comparison, graphite has a narrow distribution of phonon MFPs in the through-plane axis between 40 and 250 nm at room temperature [26] and experiments [26,27] showed the through-plane thermal conductivity of graphite significantly decreases at the thickness around 200 nm.

This result is further supported by the fact that the speed of sound along the through-plane direction as determined from picosecond acoustics is v = (2.36 ± 0.14) nm ps^{-1} (Table 3.1),

which is relatively low compared to other 2D materials, e.g., v = 3.2 nm ps^{-1} for MoS_2 [28]. ReS_2 has a triclinic unit cell, and the through-plane direction does not correspond precisely to one of the crystalline axes. Thus, I use the effective elastic constant along the through-plane direction as $C_{33}' = \rho v^2$ = (43 ± 5) GPa, expecting that the true C_{33} would be slightly higher than C_{33}'. By contrast, C_{33} of MoS_2 is 52 GPa. [28] I note that the elastic constant results are not consistent with the results of Ref. [25]: considering that the curvature of interlayer coupling energy is an elastic constant, the difference of the elastic constant between ReS_2 and MoS_2 is more dramatic in Ref. [25] compared to our experimental results. The interface thermal conductance is G_1 (metal/ReS_2) ≈16 MW m^{-2} K^{-1} and G_2 (ReS_2/substrate) ≈10 MW m^{-2} K^{-1} and also insensitive to the flake thickness. The difference between Al or NbV alloy transducers was negligible.

The in-plane thermal conductivity of ReS_2 is higher along the Re-chains, (70±18) W m^{-1} K^{-1}, compared to transverse to the chains, (50±13) W m^{-1} K^{-1}. These values are the maximum and the minimum of the in-plane thermal conductivity, respectively. Therefore, the orientation-dependence of the in-plane thermal conductivity of ReS_2 will appear as an ellipse. From this, the thermal conductivity along the *a*-direction can be estimated as (53±13) W m^{-1} K^{-1}. Tongay *et al.* [25] gives a rough estimate of lattice thermal conductivity as ≈70 and 0.05 W m^{-1} K^{-1} for the in-plane and out-of-plane, respectively, without elaborating on potential in-plane anisotropy.

The one-dimensional (1D) metallic chains of Re atoms in ReS_2 are related to the formation of charge density waves (CDWs), [29] which implies a possibile contribution of CDWs to the thermal conductivity of ReS_2. In $K_{0.3}MoO_3$, [30] a CDW compound having 1D chains made up of MoO_6 octahedra, CDWs contribute to heat conduction in the chain direction and less significantly in the direction transverse to the chains. Similar contributions of CDW excitations to thermal conductivity have been reported for $(NbSe_4)_{10}I_3$ [31] and $(TaSe_4)_2I$. [32] At

the present time, I do not know if CDWs contribute significantly to thermal conductivity of ReS_2. WTe_2 has a crystal structure similar to that of ReS_2, i.e., having 1D zigzag chains of W atoms on the planes, but the in-plane thermal conductivity of WTe_2 is isotropic within experimental uncertainty.

Figure 3.11(a) shows a summary of 2D materials whose in-plane and through-plane thermal conductivities have been experimentally determined in the bulk limit at room temperature, together with BP, WTe_2, and ReS_2 from this work. Other than graphite, sulfides like MoS_2, WS_2, and ReS_2 present the highest in-plane thermal conductivities, followed by a selenide (WSe_2) and a telluride (WTe_2). Although the experimental data for $MoSe_2$ and $MoTe_2$ are lacking, theory shows that the thermal conductivity of TMDCs in the 2*H* structure is mainly determined by the chalcogen element. [33] The transition metal element, whether it is Mo or W, is much less significant for thermal conductivity, especially for selenides and tellurides. [33]

I note that the through-plane thermal conductivity of materials in a distorted 1*T* structure, e.g., ReS_2 and WTe_2, is lower than 1 W m^{-1} K^{-1}, while those in a 2*H* phase or BP span from 1.5 to 5.4 W m^{-1} K^{-1}. Consequently, due to the high in-plane thermal conductivity and the low through-plane thermal conductivity, ReS_2 shows a notably high anisotropy of the in-plane to the through-plane thermal conductivity, $\approx$130 and 90 for the two in-plane directions, which is only exceeded by graphite. [15]

It is possible that a phonon focusing effect contributes significantly to the high anisotropy of ReS_2. A strong phonon focusing effect in anisotropic layered materials [34,35] implies a negative correlation between the in-plane and through-plane thermal conductivities. Both ReS_2 and WTe_2 have a distorted 1*T* strucure with 1D metallic chains within the plane of the crystal; and both ReS_2 and WTe_2 have weak bonding in the through-plane direction: the group velocity

of the longitudinal acoustic mode in the through-plane direction of WTe_2 is (2.00±0.12) nm ps^{-1}, which is smaller than but comparable to that of ReS_2, (2.36±0.14) nm ps^{-1}. (See Table 5.1) However, the in-plane thermal conductivity of ReS_2 is much larger than that of WTe_2, by more than a factor of five, while the through-plane thermal conductivity is smaller, i.e., 0.55 and 0.8 W m^{-1} K^{-1} for ReS_2 and WTe_2, respectively. This is in agreement with one of the implications of the phonon focusing effect [35] that, for a fixed value of a group velocity of the through-plane direction, an increase in the group velocity of the in-plane axis decreases the thermal conductivity along the through-plane direction.

Interface thermal conductance is another important property, especially in nanoscale devices where thermal management requires that excess heat can be dissipated into high thermal conductivity electrical contacts. Figure 3.11(b) shows the interface thermal conductances (G_1) between a metal and a 2D material that have been measured by TDTR as a function of the through-plane thermal conductivity of the materials. G_1 has been reported to be < 80 MW m^{-2} K^{-1}, consistently low compared to Al on Si or on Si thermal oxide showing $G_1 \approx$ 150–200 MW m^{-2} K^{-1}. G_1 appears to decrease with decreasing through-plane thermal conductivity. This trend can also be explained by a phonon focusing effect, namely a high in-plane group velocity of an anisotropic material reduces the heat transfer across the interface in the plane-normal direction, as well as the through-plane thermal conductivity. [34] I note that the AlO_x overlayer in ReS_2 and in BP or a thin oxidized layer at the top of the flakes modifies the interface and changes the G_1 values. However, low G_1 has also been observed in a bulk specimen with minimal air exposure. Thus, the relatively low G_1 appears to be intrinsic to the interface between a metal and a highly anisotropic 2D material, although the details of the thermal conductance will likely depend on the specific material properties.

The thermal conductance for the interface between a ReS_2 flake and a Si substrate is also small, G_2 =(9±3) MW m^{-2} K^{-1}. However, as the flakes are physically placed on the substrates, the interfaces between a flake and a substrate are not well characterized in terms of roughness, contamination by adsorbed hydrocarbons and water, or strength of interfacial bonding. Thus, I prefer not to speculate on mechanisms that produce the low values of G_2.

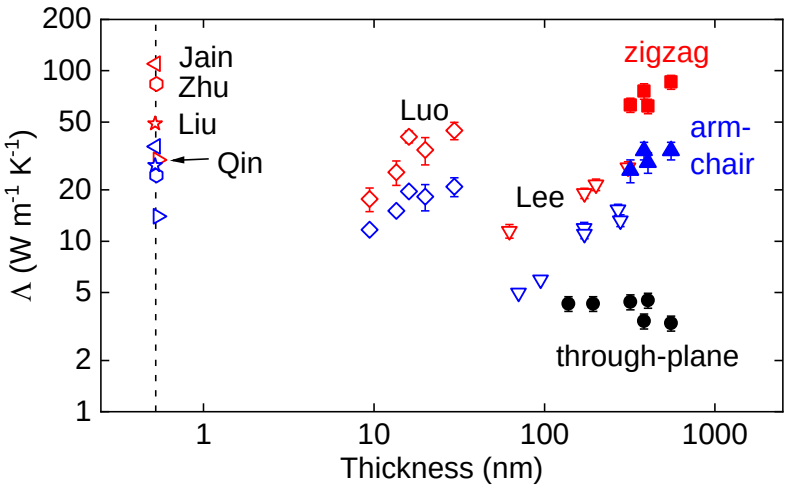

Figure 3.8. Thermal conductivities of BP for the zigzag (red), the armchair (blue), and the through-plane direction (black), plotted in comparison to the reported values as a function of thickness of BP. The monolayer properties are predicted by first-principles calculations (open symbols) and plotted for thickness of 5.25 Å. The measured data are reported for few-layered BP. The data of prior work are taken from Ref. [18,20,21,36–38].

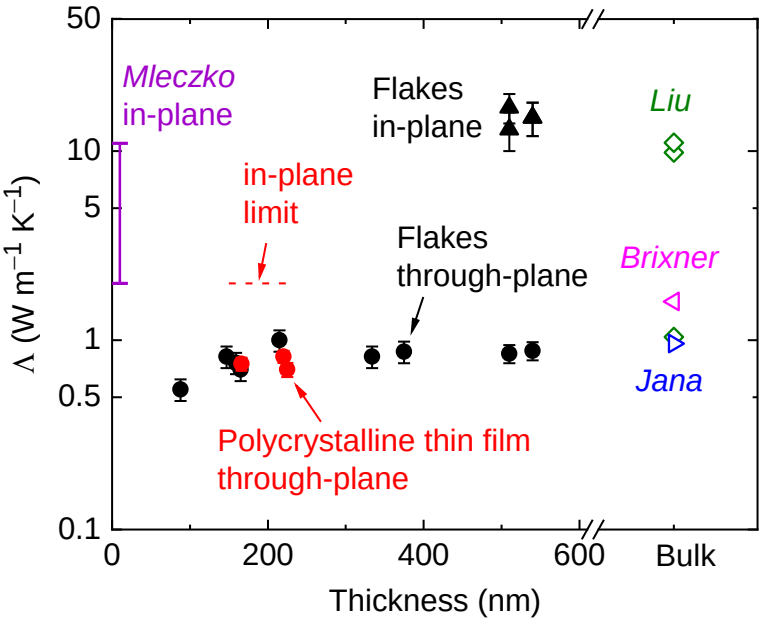

Figure 3.9. Summary of thermal conductivity of WTe_2 as a function of thickness at room temperature. The solid symbols are measured by TDTR for the exfoliated flakes and the poly-crystalline thin films. The dotted line is the upper limit of the in-plane thermal conductivity of the polycrystalline thin films. The open symbols are from literature of Ref. [23,24,39,40].

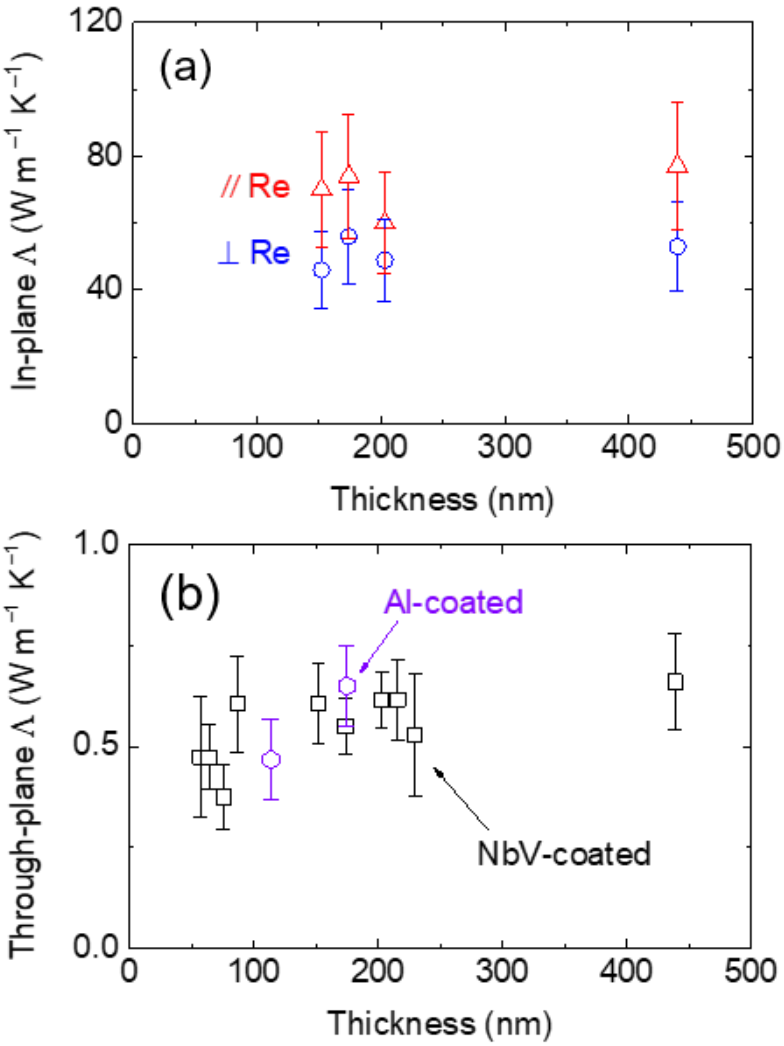

Figure 3.10. (a) In-plane and (b) through-plane thermal conductivity of exfoliated ReS_2 flakes as a function of thickness. All the flakes are coated with NbV transducer, except for the two flakes in (b) (purple symbol), which are coated with Al.

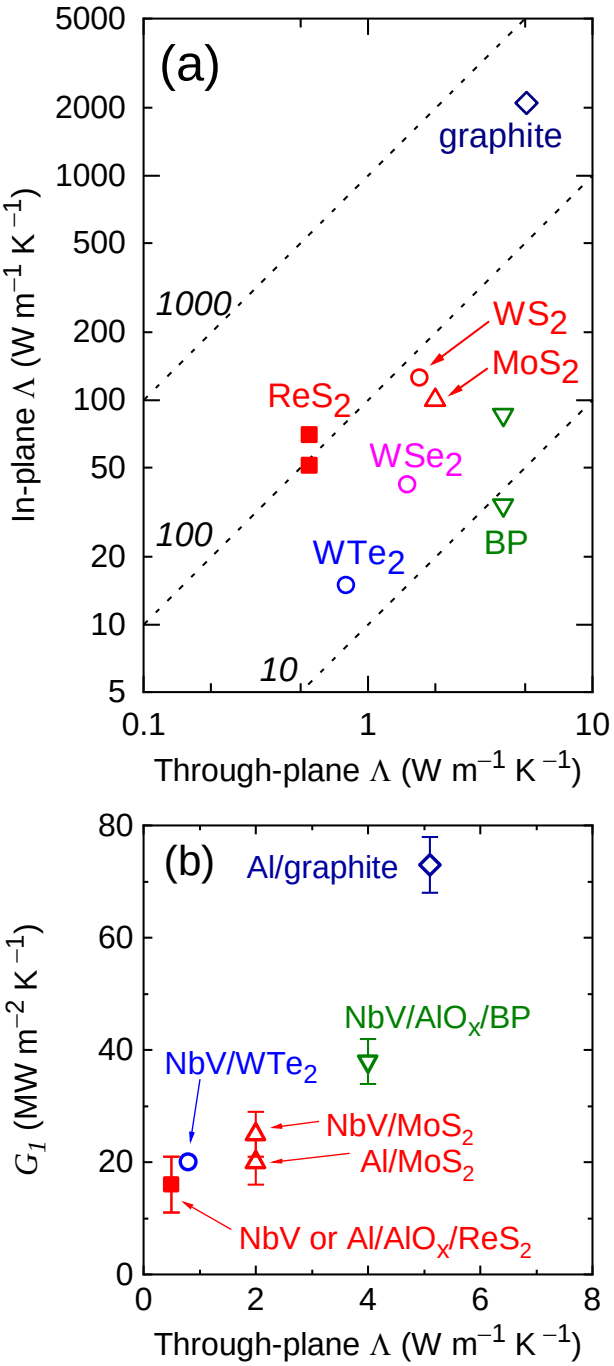

Figure 3.11. (a) Thermal conductivity of 2D materials for which in-plane and through-plane thermal conductivities in bulk limit are experimentally determined at room temperature. The dashed lines represent constant anisotropy ratio, i.e., in-plane to through-plane thermal conductivity. (b) Interface thermal conductance between a metal and a 2D material. The data are taken from: graphite [15], MoS_2 [16], WS_2 [41], WSe_2 [42].

3.5. Reference

[1] J. D. Wood, S. A. Wells, D. Jariwala, K. S. Chen, E. Cho, V. K. Sangwan, X. Liu, L. J. Lauhon, T. J. Marks, and M. C. Hersam, *Nano Lett.* **14**, 6964 (2014).

[2] S. Sugai and I. Shirotani, *Solid State Commun.* **53**, 753 (1985).

[3] J. Wu, N. Mao, L. Xie, H. Xu, and J. Zhang, *Angew. Chemie* **127**, 2396 (2015).

[4] D. A. Chenet, O. B. Aslan, P. Y. Huang, C. Fan, A. M. van der Zande, T. F. Heinz, and J. C. Hone, *Nano Lett.* **15**, 5667 (2015).

[5] L. Hart, S. Dale, S. Hoye, J. L. Webb, and D. Wolverson, *Nano Lett.* **16**, 1381 (2016).

[6] Y. Zhou, H. Jang, J. M. Woods, Y. Xie, P. Kumaravadivel, G. A. Pan, J. Liu, Y. Liu, D. G. Cahill, and J. J. Cha, *Adv. Funct. Mater.* **27**, 1605928 (2017).

[7] D. G. Cahill, *Rev. Sci. Instrum.* **75**, 5119 (2004).

[8] C. C. Stephenson, R. L. Potter, T. G. Maple, and J. C. Morrow, *J. Chem. Thermodyn.* **1**, 59 (1969).

[9] J. E. Callanan, G. A. Hope, R. D. Weir, and E. F. Westrum, *J. Chem. Thermodyn.* **24**, 627 (1992).

[10] SGTE, *Pure Substances. Part 4 Compounds from HgH_g to ZnTe_g* (Springer-Verlag Berlin Heidelberg, 2001).

[11] G. T. Hohensee, W.-P. Hsieh, M. D. Losego, and D. G. Cahill, *Rev. Sci. Instrum.* **83**, 114902 (2012).

[12] J. P. Feser, J. Liu, and D. G. Cahill, *Rev. Sci. Instrum.* **85**, 104903 (2014).

[13] M. D. Groner, F. H. Fabreguette, J. W. Elam, and S. M. George, *Chem. Mater.* **16**, 639 (2004).

[14] K. E. O'Hara, X. Hu, and D. G. Cahill, *J. Appl. Phys.* **90**, 4852 (2001).

[15] J. P. Feser and D. G. Cahill, *Rev. Sci. Instrum.* **83**, 104901 (2012).

[16] J. Liu, G.-M. Choi, and D. G. Cahill, *J. Appl. Phys.* **116**, 233107 (2014).

[17] L. Zhu, G. Zhang, and B. Li, *Phys. Rev. B* **90**, 214302 (2014).

[18] G. Qin, Q.-B. Yan, Z. Qin, S.-Y. Yue, M. Hu, and G. Su, *Phys. Chem. Chem. Phys.* **17**, 4854 (2015).

[19] T.-H. Liu and C.-C. Chang, *Nanoscale* **7**, 10648 (2015).

[20] A. Jain and A. J. McGaughey, *Sci. Rep.* **5**, 8501 (2015).

[21] Z. Luo, J. Maassen, Y. Deng, Y. Du, M. S. Lundstrom, P. D. Ye, X. Xu, R. P. Garrelts, M.

S. Lundstrom, P. D. Ye, and X. Xu, *Nat Commun* **6**, 9572 (2015).

[22] X. Ling, L. Liang, S. Huang, A. A. Puretzky, D. B. Geohegan, B. G. Sumpter, J. Kong, V. Meunier, and M. S. Dresselhaus, *Nano Lett.* **15**, 4080 (2015).

[23] G. Liu, H. Y. Sun, J. Zhou, Q. F. Li, and X.-G. Wan, *New J. Phys.* **18**, 33017 (2016).

[24] M. J. Mleczko, R. L. Xu, K. Okabe, H.-H. Kuo, I. R. Fisher, H. S. P. Wong, Y. Nishi, and E. Pop, *ACS Nano* (2016).

[25] S. Tongay, H. Sahin, C. Ko, A. Luce, W. Fan, K. Liu, J. Zhou, Y.-S. Huang, C.-H. Ho, J. Yan, D. F. Ogletree, S. Aloni, J. Ji, S. Li, J. Li, F. M. Peeters, and J. Wu, *Nat Commun* **5**, 3252 (2014).

[26] H. Zhang, X. Chen, Y.-D. Jho, and A. J. Minnich, (n.d.).

[27] Q. Fu, J. Yang, Y. Chen, D. Li, and D. Xu, *Appl. Phys. Lett.* **106**, 31905 (2015).

[28] G. Zhu, J. Liu, Q. Zheng, R. Zhang, D. Li, D. Banerjee, and D. G. Cahill, *Nat. Commun.* **7**, 13211 (2016).

[29] C. Rovira and M. H. Whangbo, *Inorg. Chem.* **32**, 4094 (1993).

[30] M. Z. Bihar, D. Starešini, K. Biljakovi, and T. Sambongi, *Eur. Lett* **40**, 73 (1997).

[31] A. Smontara, K. Biljaković, and S. N. Artemenko, *Phys. Rev. B* **48**, 4329 (1993).

[32] R. S. Kwok and S. E. Brown, *Phys. Rev. Lett.* **63**, 895 (1989).

[33] D. O. Lindroth and P. Erhart, *Phys. Rev. B* **94**, 115205 (2016).

[34] Z. Chen, Z. Wei, Y. Chen, and C. Dames, *Phys. Rev. B* **87**, 125426 (2013).

[35] A. J. Minnich, *Appl. Phys. Lett.* **107**, 183106 (2015).

[36] J. Zhu, J.-Y. Chen, H. Park, X. Gu, H. Zhang, S. Karthikeyan, N. Wendel, S. A. Campbell, M. Dawber, X. Du, M. Li, J.-P. Wang, R. Yang, and X. Wang, *Adv. Electron. Mater.* n/a (2016).

[37] X. Liu, J. D. Wood, K.-S. Chen, E. Cho, and M. C. Hersam, *J. Phys. Chem. Lett.* **6**, 773 (2015).

[38] S. Lee, F. Yang, J. Suh, S. Yang, Y. Lee, G. Li, H. Sung Choe, A. Suslu, Y. Chen, C. Ko, J. Park, K. Liu, J. Li, K. Hippalgaonkar, J. J. Urban, S. Tongay, and J. Wu, *Nat Commun* **6**, 9573 (2015).

[39] L. H. Brixner, *J. Inorg. Nucl. Chem.* **24**, 257 (1962).

[40] M. K. Jana, A. Singh, D. J. Late, C. R. Rajamathi, K. Biswas, C. Felser, U. V Waghmare, and C. N. R. Rao, *J. Phys. Condens. Matter* **27**, 285401 (2015).

[41] A. Pisoni, J. Jacimovic, R. Gaál, B. Náfrádi, H. Berger, Z. Révay, and L. Forró, *Scr. Mater.* **114**, 48 (2016).

[42] C. Chiritescu, D. G. Cahill, N. Nguyen, D. Johnson, A. Bodapati, P. Keblinski, and P. Zschack, *Science (80-.).* **315**, 351 (2007).

CHAPTER 4
NON-EQUILIBRIUM THERMAL TRANSPORT IN PT AND CO

4.1. Design of experiments using an ultrathin Co layer as a thermometer

To examine the non-equilibrium dynamics in Pt within the framework of the 3TM and any possible discrepancy from the 3TM, I disturb Pt thin films optically with a laser pulse of 1.58 eV energy and ≈1 ps duration and monitor subsequent temperature changes. The use of an accurate thermometer is essential, particularly when the thermal reservoirs are driven out of equilibrium. Previous reports on the electron-phonon coupling of Pt are relatively few [1–5]. Ref. [2] directly probes the electron dynamics of a Pt thin film using time-resolved photoemission spectroscopy at 77 K. The other works rely on transient reflectivity either at the irradiated Pt surface [1,3] or at the Cu surface on the opposite side of the irradiated Pt layer [4,5]. As I will discuss later, optical reflectivity depends on both electron and phonon temperatures and also lattice strain due to thermal expansion. Thus, the separation of the contributions from each temperature is not straightforward.

I employ a sub-nm-thick Co embedded in Pt as a thermometer and monitor the magnon temperature changes at the specific position of Co, i.e., ΔT_m(Co), via time-resolved polar magneto-optical Kerr effect (TR-MOKE) within a small fluence limit, i.e., $\Delta T_m < 50$ K. Time-domain thermoreflectance (TDTR) signals are collected simultaneously for comparison. One of the goals of this work is to characterize the properties of Co as a thermometer. Thus I measure ultrafast dynamics of a 10-nm-thick Co via time-resolved quadratic magneto-optical Kerr effect (TR-QMOKE), and evaluate the electron-phonon coupling constant (g_{ep}) and electron-magnon thermalization time ($\tau_{em}=g_{em}/C_m$) of Co.

Using the ultrathin Co thermometer, I examine the magnon temperature changes at three different positions within Pt of 40–46 nm thickness — at the irradiated surface, in the middle, and at the bottom of the Pt layer — as well as in the middle of a very thin Pt layer of total 6 nm. The sample structures are Pt(4)/Co(0.8)/Pt(42), Pt(16)/Co(0.8)/Pt(24), and Pt(2)/Co(0.8)/Pt(4), with the numbers in parentheses represent thicknesses in nm. I perform pump-probe measurements, in which the pump beam is incident at either of the two surfaces and the probe beam is incident on the surface closer to Co. In all of the sample configurations, the electron-phonon thermalization of Pt (g_{ep}) dominate the temperature evolutions. Heat transport is crucial in the samples with optically thick Pt layers and plays the different roles on ΔT_m(Co) depending on the positions of the thermometer.

4.2. Non-equilibrium thermal transport in Co

The 10-nm-thick Co film has preferential in-plane magnetization due to shape anisotropy and I use the TR-QMOKE to measure the changes in in-plane magnetization on ultrafast time-scales. Figure 4.1(a-b) shows the out-of-plane precession and demagnetization of the 10-nm Co film capped with a 2-nm Pt layer, respectively, for an absorbed fluence of 1.2 J m^{-2}. The precession frequency in Fig. 4.1(a) is 24 GHz; the Kittel formula gives a saturation magnetization of 1.4×10^6 A m^{-1}, in good agreement with the value of bulk Co. The time constant for the damping of the amplitude of the precession is ≈340 ps and a Gilbert damping parameter of ≈0.014. In Fig. 4.1(b), the magnetization of Co shows the so-called type-I behavior, characterized by fast demagnetization followed by slower and partial recovery. [6] The maximum rise of the magnetic temperature is < 50 K, far below the Curie temperature. I confirmed that the TR-QMOKE data are linear in the absorbed fluence for laser fluences up to

2.0 J m^{-2}. Therefore, I conclude that the TR-MOKE signal is linearly related to the magnon temperature (T_m) of Co. [6]

The 10 nm thickness of the Co layer is comparable to the optical absorption depth ≈12 nm, and therefore the entire layer contributes significantly to the measured TR-QMOKE signal. To account for the temperature gradient and associated magnetization gradient in the Co layer, I compare the demagnetization data with the value of T_m calculated for the midpoint of the Co layer, i.e., a depth of 5 nm below the Pt capping layer. Fig. 4.1(b) also includes TDTR data, which is affected by phonon (T_{ph}) and electron (T_e) temperatures and lattice strain. (The full-width-at-half-maximum of the correlated pump-probe pulses is 1.2 ps and zero-time-delay is set at the peak of the pump optical pulse.)

The temperatures of electrons, magnons, and phonons as a function of time and position are modeled by numerically solving the 3TM using the Crank-Nicholson method. The materials parameters used in modeling are shown in Table 4.1. The absorbed fluence and absorption profile are calculated using a transfer matrix method with refractive indices of the constituent layers. The demagnetization data is normalized to calculated ΔT_m(Co) at the time delay of 50 ps based on the optical absorption depth and the known thermal properties of substrate and the metal/substrate interface.

The electrons, phonons, and magnons are out-of-equilibrium during the first 3 ps following the optical excitation. T_m(Co) rises nearly instantaneously following the electron temperature, implying that the ratio of $(g_{em}C_p)/(g_{ep}C_m) > 1$. [6] The temperature evolutions at time delays ≤ 3 ps are dominated by volumetric energy exchange processes between the thermal reservoirs. The role of heat transport is negligible as the whole metal layers are directly heated and heat transport across the metal/substrate interface is slow. (The characteristic time scale for

cooling of the metal film by heat conduction into the substrate is ≈50 ps and will be discussed in more detail below.) The sensitivity of the magnon temperature rise (ΔT_m) to a material parameter (β) is defined in Eq. (4.1) and plotted for various parameters in Fig. 4.1(c). $\Delta T_{m,max}$ is the maximum temperature rise of magnons.

$$S(\beta) = \frac{\partial(\Delta T_{\mathrm{m}}) / \Delta T_{\mathrm{m,max}}}{d\beta / \beta} \tag{4.1}$$

The initial temperature-rise of T_m is most sensitive to g_{ep}, g_{em}, C_m and γ_e of Co. I use C_m(Co)=0.02×10^6 J m^{-3} K^{-1} [7] and γ_e(Co)=680 J m^{-3} K^{-2} [8] from literature values for bulk Co; g_{ep} and g_{em} of Co are two free parameters that I vary to fit the data. The best-fit is obtained with g_{ep}(Co)=(2.0±0.2)×10^{18} W m^{-3} K^{-1} and g_{em}(Co)=(0.9±0.1)×10^{17} W m^{-3} K^{-1}. These values for g_{ep} and g_{em} for Co are similar to previous reports for ferromagnets, e.g., g_{ep}=1×10^{18} W m^{-3} K^{-1} and g_{em}=1×10^{17} W m^{-3} K^{-1} for Ni, and g_{ep}=0.7×10^{18} W m^{-3} K^{-1} and g_{em}=0.6×10^{17} W m^{-3} K^{-1} for FePt:Cu at 300 K. [6]

The evolution of temperature at time delay > 3 ps is determined by phonon properties: C_{ph}(Co) and the phonon interface thermal conductance (G_{ph}) between Co and the Al_2O_3 substrate. G_{ph}(Co/Al_2O_3) is a free parameter that is determined from fits to the data at time delays between 50 ps and 1 ns; I find G_{ph}(Co/Al_2O_3) ≈400 MW m^{-2} K^{-1}, a relatively high value for the conductance of a metal/sapphire interface. Ref. [9] shows that thermal conductance of strongly-bonded metal/dielectric interface is determined by the Debye temperature and sound velocity, with one of the examples being the Al/MgO interface with G_{ph}≈500 MW m^{-2} K^{-1}. As Co and Al have similar Debye temperatures, [8] and MgO and sapphire have similar Debye temperatures, [10] I expect that a clean interface of Co/Al_2O_3 should have similarly high G_{ph}. "Remote electron-phonon" coupling refers to coupling of charge carriers in metal and surface phonons in polar substrates, and has been suggested as a possible channel for heat transfer across

the interface of metal and substrate. [11] However, I do not find any evidence of remote electron-phonon coupling in the data and thus, do not include the coupling channel in my model.

I also observe ultrafast demagnetization in a sub-nm-thick Co driven by direct excitation, using a Pt(2)/Co(0.8)/Pt(4) sample with an absorbed fluence of 0.4 J m^{-2}, as shown in Figure 4.2(a-b). The sub-nm-thick Co layer possesses perpendicular magnetic anisotropy and is measured via TR-MOKE. The use of an ultrathin Co layer minimizes inhomogeneous heating and confines the magneto-optic response to a thin layer of the sample. Also, due to the small volume of Co relative to Pt, the temperature evolutions are less sensitive to the properties of Co (see Fig. 4.2(c)). The sensitivity to γ_e(Co) becomes negligible and only the ratio, τ_{em}(Co)=C_m/g_{em}, i.e., electron-magnon thermalization time, and g_{ep}(Co) are important parameters in the model. Although the previous measurement on a 10-nm-thick Co resulted in τ_{em}(Co)≈0.2 ps, I cannot assume that τ_{em} remains the same in an ultrathin Co film. This is because the sub-nm-thick Co possesses a Curie temperature at around 600 K [12], significantly lower than 1400 K of bulk Co, and the magnon heat capacity in ultrathin Co could be significantly higher than in bulk Co. Some research [13,14] has suggested enhanced electron-magnon coupling in ultrathin ferromagnets, although the degree of enhancement varies for different underlayers and experiment conditions. Therefore, I treat τ_{em}(Co) as a free parameter in addition to g_{ep}(Pt) in this sample and compare with the results of the other Pt/Co/Pt trilayer structures. I note that it is difficult to separate g_{ep}(Co) and g_{ep}(Pt) due to their similar effects on T_m(Co) at short time delays. I use g_{ep}(Co) from my experiments on the 10 nm-thick Co layer. A factor of two uncertainty in g_{ep}(Co) propagates into <20% uncertainty in g_{ep}(Pt).

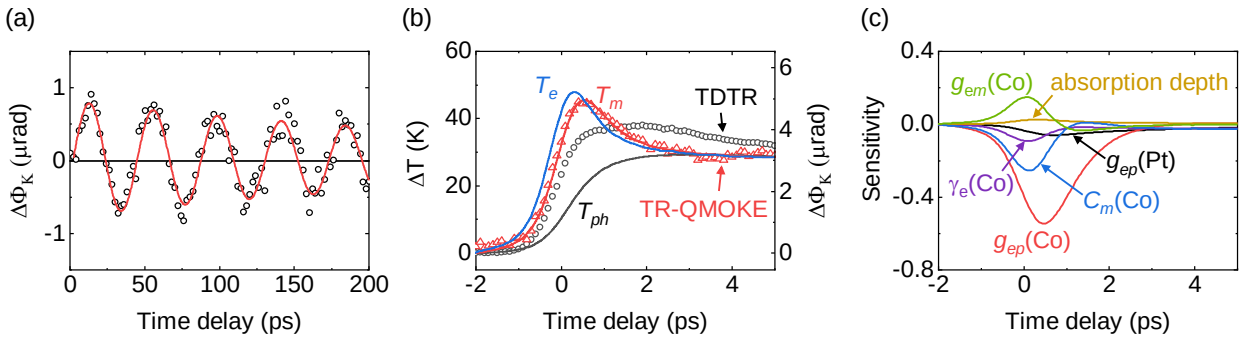

Figure 4.1. Time-resolved quadratic magneto-optical Kerr effect (TR-QMOKE) measurements of Co 10 nm capped with Pt 2 nm. (a) Out-of-plane component of precession in Co derived as the sum of TR-QMOKE signals with probe polarizations of +45° and –45° relative to the applied magnetic field of 0.3 T (black symbol). The best fit gives the frequency of 24 GHz and decay constant of 340 ps (red line). (b) Ultrafast demagnetization of Co derived as the difference of TR-QMOKE signals with probe polarizations of +45° and –45° (red symbol). Time-domain thermoreflectance (TDTR) data are shown as black symbol. Solid lines are simulated electron (blue), magnon (red), and phonon (black) temperatures of Co at 5 nm depth by using a three-temperature model. (c) Sensitivity calculations of the magnon temperature to materials parameters.

4.3. Non-equilibrium thermal transport in Pt probed by an ultrathin Co thermometer

Ultrafast demagnetization in Co can occur via heat transport through a Pt layer of 42 nm thickness, as shown in Figure 4.3(a-c). The measurement is performed on Pt(42)/Co(0.8)/Pt(4) with the pump incident on the Pt(42) surface and an absorbed fluence of 1.2 J m^{-2}. The Co layer absorbs only 0.2% of the total fluence (see Table 4.2) and is predominately heated indirectly by transport through the Pt layer. T_e and T_m of Co increase by ≈7 K across zero-time-delay, and cool quickly as the out-of-equilibrium electrons lose energy to the phonons. At time delays > 50 ps, all of the thermal reservoirs in Co and Pt are equilibrated, and the temperature evolution is determined by thermal diffusion of phonons into the substrate. The maximum demagnetization in Co is 0.9%, which is significantly reduced compared with direct excitation of Co, e.g., 13% maximum demagnetization in Fig. 4.2.

Fig. 4.3(c) shows the calculated sensitivities of ΔT_m(Co) to material parameters at time delays ≤ 5 ps. Fig. 4.3(c) includes parameters which have a significant influence on ΔT_m(Co) at short time delays, and significant uncertainties. (Sensitivities to the other parameters that are well-defined from literatures and other experiments, e.g., thickness, phonon heat capacity, and thermal conductivity, are shown in Figure 4.4.) ΔT_m(Co) is most sensitive to g_{ep}(Pt) because most of the laser energy deposited in the Pt/Co/Pt structure is redistributed to the Pt phonons while the amount of the energy consumed by the ultrathin Co layer is small. The electronic heat capacity coefficient of Pt, γ_e(Pt), is fixed at 400 J m^{-3} K^{-2} and will be discussed in more detail below.

As the Pt layer is much thicker than the optical absorption depth ≈12 nm, ΔT_m(Co) is affected by parameters that control heat transport and the initial energy deposition profile in Pt.

The parameters related to heat transport are the electron thermal conductivity of Pt (Λ_e(Pt)) and the electron thermal conductance at the Pt/Co interface (G_{ee}(Pt/Co). Λ_e(Pt) is determined by applying the Wiedemann-Franz law to the measured electrical conductivity of Pt. For G_{ee}(Pt/Co), the lower limit can be determined through analysis of TDTR as 8 GW m^{-2} K^{-1} through the relation of G(Pt/Pt)$^{-1}$=2·[G_{ee}(Pt/Co)]$^{-1}$ + [Λ(Co)/h(Co)]$^{-1}$. G_{ee}(Pt/Co) has a negligible effect on ΔT_m(Co). To evaluate the influence of the energy deposition profile on ΔT_m(Co), I approximate the profile as a single exponential decay with the absorption depth of Pt, 12 nm, and calculate the sensitivity (see Fig. 4.3(c)). The sensitivity to the absorption depth is large and comparable to that of g_{ep}(Pt). I have two free parameters, g_{ep}(Pt) and τ_{em}(Co), same as in the analysis discussed above for the Pt(2)/Co/Pt(4) sample. In contrast to the Pt(2)/Co/Pt(4) sample where heat transport is negligible, I expect that if ballistic transport of electronic excitations in Pt is significant, it would contribute to the enhanced energy deposition profile, thus affecting the fitted value of g_{ep}(Pt).

Fig. 4.3(d-f) shows the TR-MOKE and TDTR data of the same sample, Pt(42)/Co(0.8)/Pt(4), but with both the pump and probe incident on the Pt(4) surface and an absorbed fluence of 0.7 J m^{-2}. In this configuration, Co is directly heated; the Co layer absorbs 4.4% of the total fluence (see Table 4.2) and the maximum demagnetization is 8%. The major difference compared to having the pump on the Pt(42) surface is that heat transport in Pt now serves to cool the Co layer. The sensitivities of ΔT_m(Co) to the parameters relevant to heat transport, i.e., Λ_e(Pt) and G_{ee}(Co/Pt), and the absorption depth have opposite signs, while the other parameters including g_{ep}(Pt) remain similar to the previous case. (See Fig. 4.3(c,f)) Therefore, I can expect that ballistic transport of excited electrons would affect the fitted g_{ep}(Pt)

in the opposite sense to the one in the sample configuration of Fig. 4.3(a-c), if the effect of ballistic transport is significant.

The ultrathin Co layer is also demagnetized when it is heated through Pt layers of 16 or 24 nm thickness, i.e., in Pt(16)/Co(0.8)/Pt(24) with the pump incident either on the Pt(16) or Pt(24) surface, respectively. (See Figure 4.5) The maximum demagnetization is 4% for an absorbed fluence of 0.6 and 1.2 J m^{-2}, respectively. Heat transport in Pt plays both roles, i.e., heat transport through the irradiated Pt layer increases T_m(Co), whereas heat transport through the underlying Pt layer lowers T_m(Co). As a result, the sensitivities to the heat transport parameters are significantly reduced when the Pt(16) surface is irradiated with the pump and remain small but positive when the Pt(24) surface is irradiated with the pump.

The uncertainties in the two free parameters, g_{ep}(Pt) and τ_{em}(Co), are evaluated with the criterion of $\sigma^2 \leq 2\sigma_{min}^2$, where σ^2 is the sum of square of the residuals. The contours for $\sigma^2=2\sigma_{min}^2$ are shown in Figure 4.9. The values that are consistent with all five sample configurations are $g_{ep}(\text{Pt})=(6\pm1)\times10^{17}$ W m^{-3} K^{-1} and $\tau_{em}(\text{Co})=(0.23\pm0.05)$ ps. Throughout my analysis, I use the optical absorption profile calculated from the refractive indices of Pt, Co, and Al_2O_3, which is likely to underestimate the energy deposition length scale if ballistic transport of electronic excitations is significant. However, the fitted g_{ep}(Pt) is not consistently low for the sample configurations in which heat transport contributes to heating of Co magnons, i.e., "Pt(42) front" and "Pt(16) back" in Fig. 4.9. Nor is g_{ep}(Pt) noticeably higher for sample configurations in which heat transport cools the Co magnons, i.e., "Pt(42) back" in Fig. 4.9. τ_{em} of the sub-nm-thick Co is in good agreement with τ_{em} of 10-nm-thick Co within the experimental uncertainties.

The comparison of the TDTR data with the electron and phonon temperatures is complicated at time delays < 5 ps because near-surface region of the sample is subject to

temperature and strain gradients as well as non-equilibrium between electrons and phonons. The temperature gradient can be considered by slicing the region near the surface into multilayers with varying refractive indices and applying the transfer matrix method to calculate the total reflectance at the surface. This can be easily calculated if temperature-dependence of complex refractive index, i.e., $d\tilde{n}/dT$, is known. [15] However, the non-equilibrium of electrons and phonons further requires the knowledge of $d\tilde{n}/dT = d\tilde{n}/dT_e + d\tilde{n}/dT_{ph} + d\tilde{n}/d\varepsilon$ (ε=lattice strain), which are difficult to obtain. The ΔR calculated by considering T_{ph} only is shown in Figs. 4.3 and 4.5. The simulated $\Delta R(T_{ph})$ captures the TDTR data only after the electrons and phonons are equilibrated. Therefore, without the specific information of $d\tilde{n}/dT_i$ (i=e, ph) and $d\tilde{n}/d\varepsilon$, the accurate separation of electron and phonon temperatures from the measured TDTR data is challenging.

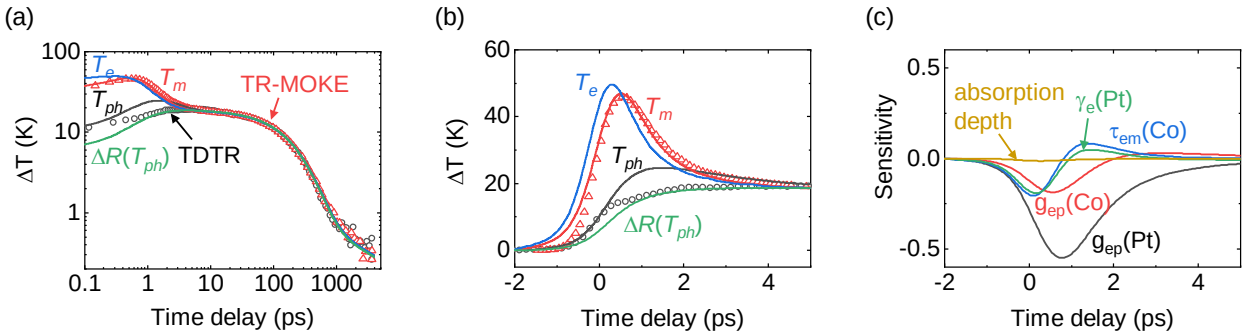

Figure 4.2. Magnetization dynamics in Pt(2)/Co(0.8)/Pt(4)/sapphire with pump and probe incident on Pt(2) surface. Time-resolved magneto-optical Kerr effect (TR-MOKE) (red symbol) and TDTR (black symbol) measurement data in (a) log-log axes and (b) linear axes at short delay times. Solid lines are simulated electron (blue), magnon (red), and phonon (black) temperatures of Co by using a 3TM. Also shown is transient reflectance simulated with the phonon temperature profile across the Pt/Co/Pt trilayer (green). (c) Sensitivity calculations of the magnon temperature of Co to materials parameters.

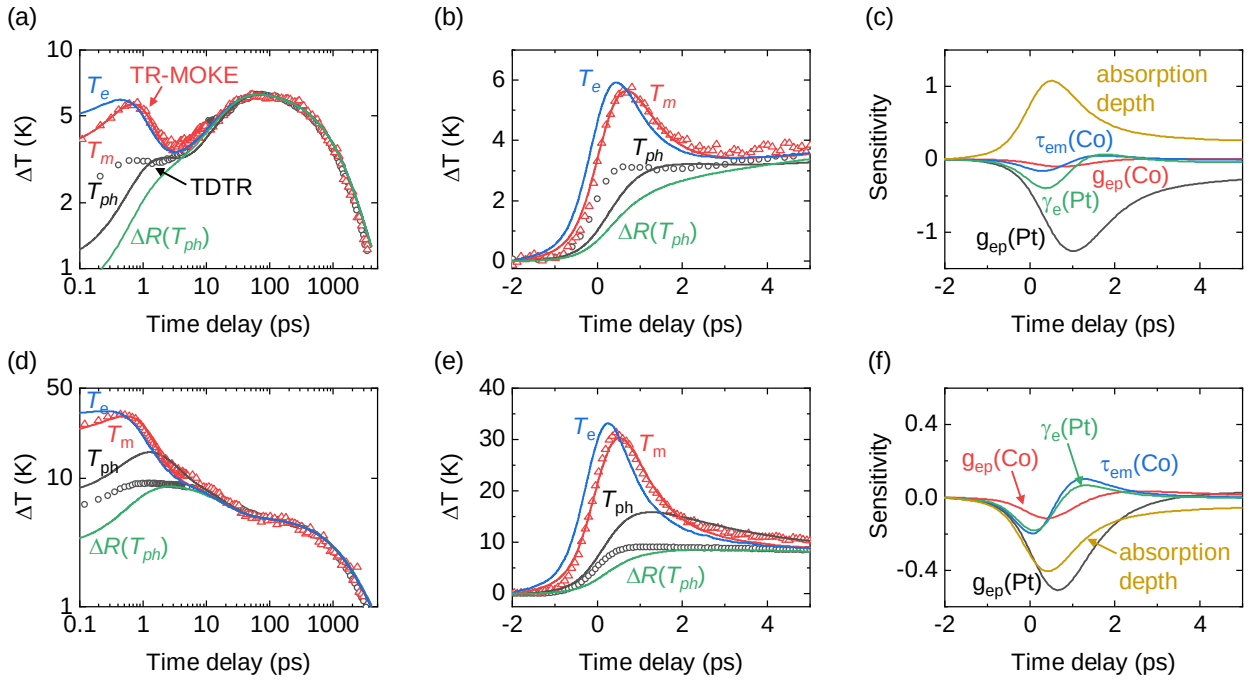

Figure 4.3. Magnetization dynamics in Pt(42)/Co(0.8)/Pt(4)/sapphire driven by heat transport through Pt layers. Pump is incident on (a-c) Pt(42) surface and (d-f) Pt(4) surface while probe is incident on Pt(4) surface in both cases. Open symbols are TR-MOKE (red) and TDTR (black) data. Solid lines are simulated electron (blue), magnon (red), and phonon (black) temperatures of Co. Also shown is transient reflectance simulated with the phonon temperature profile across the Pt/Co/Pt trilayer (green). (c, f) Sensitivity calculations of the magnon temperature of Co to materials parameters.

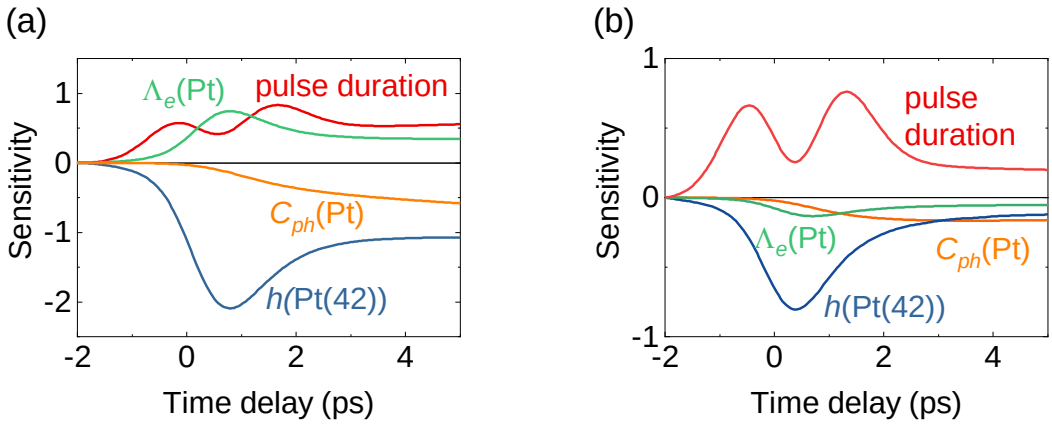

Figure 4.4. Sensitivities of a magnon temperature of Co in Pt(42)/Co(0.8)/Pt(4)/sapphire to materials and experimental parameters. Pump is incident on (A) Pt(42) or (B) Pt(4) surface, and probe is incident on Pt(4) surface in both cases. The parameters that have sensitivity magnitudes > 0.1 are displayed. Λ_e, C_{ph}, and h represent the electron thermal conductivity, phonon heat capacity, and thickness, respectively.

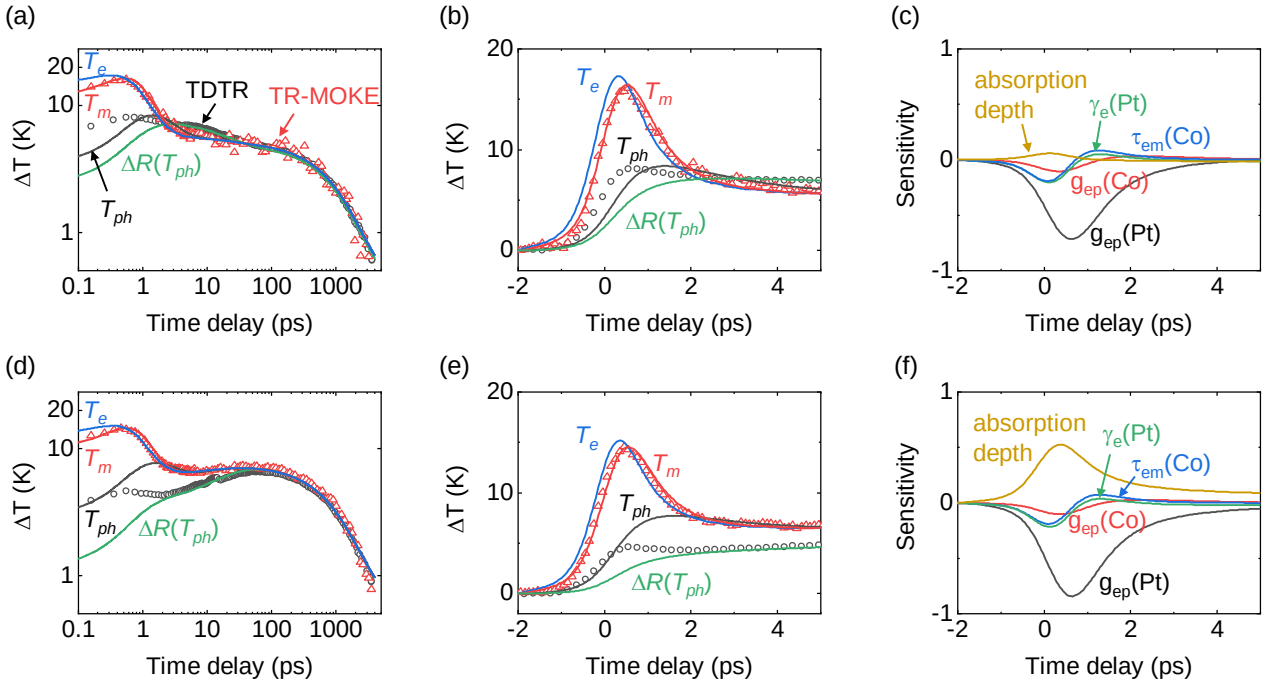

Figure 4.5. Magnetization dynamics in Pt(16)/Co/Pt(24)/sapphire driven by heat transport through Pt layers. Pump is incident on (a-c) Pt(16) surface and (d-f) Pt(24) surface, while probe is incident on Pt(16) surface in both cases. Open symbols are TR-MOKE (red) and TDTR (black) data. Solid lines are simulated electron (blue), magnon (red), and phonon (black) temperatures of Co. Also shown is transient reflectance simulated with the phonon temperature profile across the Pt/Co/Pt trilayer (green). (c, f) Sensitivity calculations of the magnon temperature of Co to materials parameters.

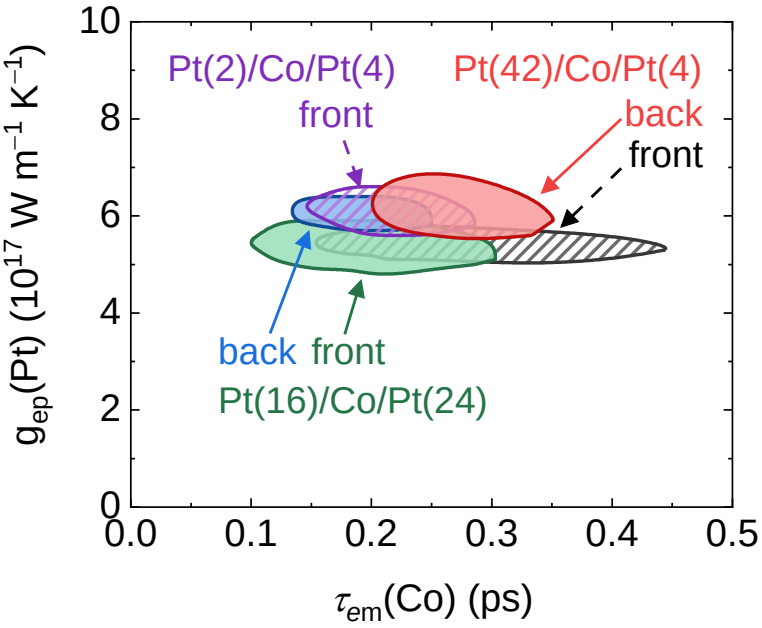

Figure 4.6. Best-fit of electron-magnon thermalization time of Co (τ_{em}(Co)) and electron-phonon coupling constant of Pt (g_{ep}(Pt)) for five configurations of Pt/Co/Pt trilayers on sapphire substrates. "Front" or "back" is the surface on which the pump pulse is incident. The patterned areas are the samples where Co is directly excited, and the solid areas are the samples where Co is indirectly excited, i.e., relative absorption in Co is $\leq$ 1.2% of total absorption.

4.4. Discussion

The electronic heat capacity coefficient, $\gamma_e(\mathrm{Pt})=C_e(\mathrm{Pt})/T$, is an important parameter for calculating the initial temperature rise of Pt electrons. Lin *et al.* [16] point out that γ_e of metals is not a constant and depends on temperature, especially when the electronic density of states is not a smooth function of energy. First-principles calculation of the electron density of states of Pt [16] shows that $\gamma_e(\mathrm{Pt})$ decreases as temperature increases, and is ≈400 J m^{-3} K^{-2} at 300 K. [16]

The experimental heat capacity of Pt, $C_P(T)$, also suggests that $\gamma_e(\mathrm{Pt})$ varies as a function of temperature in the range of 300 K $\leq T \leq$ 2000 K. [17] As the Debye temperature of Pt is 236 K, the temperature-dependence of $C_P(T)$ in this temperature range is predominantly determined by the electronic heat capacity and the difference of C_P and C_V, i.e., C_P-C_V =$\alpha^2 V_m T/\kappa_T$, where α, V_m, and κ_T are the thermal expansion coefficient, molar volume, and isothermal compressibility, respectively. After subtracting the thermodynamic term from C_P/T at 300 K using the experimental values of α=2.75×10^{-5} K^{-1} [18], V_m=9.09 cm^3 mol^{-1} [18], and κ_T=3.26×10^{-3} GPa^{-1} [19], I obtain γ_e ≈410 J m^{-3} K^{-2}, similar to the result of the first-principles calculation. [16] Therefore, I fix $\gamma_e(\mathrm{Pt})$=400 J m^{-3} K^{-2} in my work. This gives $C_e(\mathrm{Pt})=\gamma_e T$=0.12×10^6 J m^{-3} K^{-1} out of the total heat capacity of Pt, 2.82 ×10^6 J m^{-3} K^{-1} at 300 K.

The 3TM is only rigorously valid if $\tau_{ee} \ll \tau_{ep}$ and $\tau_{ee} \ll \tau_{em}$. Otherwise, non-thermal electrons could participate in energy exchange with the other thermal reservoirs at different rates than thermal electrons. There is, in fact, prior experimental and theoretical work that calls into question the validity of the 3TM. Wilson *et al.* [20] experimentally demonstrate that g_{ep} of non-thermal electrons in [Co/Pt] multilayers is a factor of 2 smaller than that of thermal electrons by comparing optical pulse excitation of 1.55 eV and electrical pulse excitation corresponding to a

few meV. First-principles calculations [21] also find smaller g_{ep} for nonthermal electrons with examples of Al, Au, and Ni for $\Delta T_e < 1000$ K.

The time scales of electron-electron and electron-magnon scattering processes that I derive for Pt and Co in my work are significantly longer than the time scales of electron-electron scattering in Pt and Co. According to the time-resolved photoemission spectroscopy, [22] τ_{ee} of Pt and Co are 5 fs and <7 fs, respectively, at 1 eV excitation energy. I obtain $\tau_{ep}=C_e/g_{ep}$ as 0.2 ps and 0.1 ps for Pt and Co, respectively, and $\tau_{em}=C_m/g_{em}$ for Co as 0.23 ps. Moreover, the fitted values of g_{ep}(Pt) and τ_{em}(Co) do not show a systematic change across the samples, as can be seen in Fig. 4.6. A possible change in g_{ep}(Co) for direct and indirect excitations of Co cannot be determined in these experiments due to the small sensitivity to g_{ep}(Co).

In this work, I demonstrate the ultrathin Co layer sandwiched by Pt layers exhibit perpendicular anisotropy and can serve as a thermometer for detecting non-equilibrium dynamics. I point out that Kerr rotation can be assumed to be linear with magnetization temperature only when the magneto-optical constants do not vary during the measurement. It is often confirmed by comparing the real and imaginary parts of complex Kerr rotation, i.e., Kerr rotation and ellipticity, respectively. Figure 4.7 shows the Kerr rotation and ellipticity of a [Co/Pt] multilayer and Pt/Co/Pt samples of this chapter. Overall, the Kerr rotation and ellipticity show similar temperature evolutions, without any change in a sign or a large difference in magnitude that are induced by photo-excited electrons. [23,24] The [Co/Pt] multilayer in Fig. 4.7(a) is 10-nm-thick, and the difference in ellipticity and rotation can be attributed to their different depth sensitivities. Ref. [25] shows that the Kerr rotation of cobalt is more sensitive to near surface while the Kerr ellipticity has less depth-dependent.

In the Pt/Co/Pt samples of this study, the Co layer is less than 1 nm and the effect of the different depth sensitivities is not expected. The difference of Kerr rotation and ellipticity is negligible in Pt(2)/Co(0.8)/Pt(4) in Fig. 4.7(b), while the difference is bigger in Pt(42)/Co(0.8)/Pt(4) when the pump is incident on either of surfaces, see Fig. 4.7(c-d). The origin of the different Kerr rotation and ellipticity in different samples despite the same sub-nm-thick Co layer is not clear yet. Since g_{ep}(Pt) derived from the Kerr ellipticity data agree with g_{ep}(Pt) from the Kerr rotation data reported in Fig. 4.6, I focus on the Kerr rotation for analysis across the samples of this work.

I apply the Pt/Co/Pt trilayer as a thermometer to determine the carrier coupling parameter in Ru. Figure 4.8 shows the TR-MOKE measurement on a sample of Pt(2)/Co(0.8)/Pt(2)/Ru(50)/ sapphire with pump on either surface and probe on top Pt surface. The overall temperature rise resembles that in the Pt/Co/Pt samples. The non-equilibrium among electrons and phonons predominantly occurs when the Ru layer is directly excited, in Fig. 4.8(a), and this results in a higher sensitivity to g_{ep}(Ru). I determine g_{ep}(Ru)=$(0.9\pm0.2)\times10^{18}$ W m^{-3} K^{-1} in Fig. 4.8(a) and $(2\pm1)\times10^{18}$ W m^{-3} K^{-1} in Fig. 4.8(b).

Prior work on laser-induced non-equilibrium in optically thick metal layers have emphasized the role of ballistic transport of photoexcited carriers of a few eV energies, for simple and noble metals, such as Au [1,26], and Cu [27]. I argue that diffusive heat transport is not negligible compared to ballistic transport and appears in different aspects for noble metals as opposed to transition metals, therefore the mechanism for heat transport should be treated carefully. In Figure 4.9, I illustrate the behaviors of diffusive heat transport in transition metals and noble metals, taking Pt and Cu as an example, respectively. I use a two-temperature model for electrons and phonons and display the electron temperature at the bottom of a metal layer in

contact with a sapphire substrate. Therefore, the behaviors shown in Fig. 4.9. are purely from a diffusive transport mechanism.

Fig. 4.9(a) shows that the normalized temperature-rise is almost identical for all the Pt thicknesses for modeling, and the temperature decay also appears identical for a Pt layer thicker than 100 nm. On the other hand, Fig. 4.9(b) shows the temperature rise is delayed for a Cu layer proportional to the Cu thickness. The faster temperature-rise in Pt than in Cu seems non-sensical given the higher electron diffusivity of Cu than of Pt, i.e., $D_e=\Lambda_e/C_e=10^{-2}$ m^2 s^{-1} and 4×10−4 m^2 s^{-1}, respectively. (See Table 4.1 and 4.3) However, this behavior is because heat transport occurs differently in Pt and Cu.

Fig. 4.9(c-d) shows the electron temperature at the bottom surface of 100-nm-thick of Pt and Cu layers on sapphire. Following laser absorption, Pt shows a small temperature rise across the time-zero, followed by a bigger increase in temperature at time delay > 1 ps, in Fig. 4.9(c). This type of temperature evolution is experimentally observed in optically thick Pt in Fig. 4.3(a) and Ru, also a transition metal, in Fig. 4.8(a). However, In Fig. 4.9(d), Cu shows most of the heat is transferred to the bottom surface within 1 ps. Then the electron temperature decreases due to energy exchange from electrons to lattice, followed by a plateau implying heat carriers in a Cu layer are thermalized.

An important metric to distinguish the different temperature evolutions in metals is the electron-phonon coupling length, i.e., $l_{ep}=\sqrt{\Lambda_e / g_{ep}}$, which represents the characteristic distance over which electrons and phonons remain in non-equilibrium. This length-scale is about ≈9 nm for Pt and ≈63 nm for Cu. In Pt, the electron-phonon non-equilibrium is even shorter than the optical absorption depth ≈ 12 nm. Thus, electrons rapidly thermalize with phonons, and heat transport is described by equilibrium thermal diffusivity, i.e., $D_{tot}=\Lambda_{tot}/C_{tot}$. Ctot is the sum of

electron and phonon heat capacities. The small temperature rise across zero-time-delay can be attributed to direct optical absorption, which has an exponential decay profile present throughout the metal layer. On the other hand, electrons in Cu can maintain high temperature over the long l_{ep}, and display their own heat transport characterized by D_e.

Typically, noble metals such as Au and Cu, show longer electron-phonon coupling lengths and exhibit pronounced electron transport behaviors, which are often confused with ballistic transport behaviors. The footprint of ballistic transport is the travel time being linear with distance. Prior work demonstrated the presence of ballistic transport by showing the onset-time of temperature rise is linear with the thickness of Au [26] and Cu [27] layers. However, the linear relationship does not exclusively belong to ballistic transport. In Figure 4.10, I plot the Cu thickness and thickness-squared versus onset-time in a Cu layer on sapphire, based on the 2TM calculations in Fig. 4.9(b). The onset-time is defined as the time-delay where the temperature rise is 10% of the maximum temperature at the bottom surface of the Cu layer. Fig. 4.10(a) shows the thickness is linear with the onset-time and the apparent slope, 0.58×10^6 m s^{-1}, is very close to the Fermi velocity of Cu in Ref. [27]. However, the slope in Fig. 4.10(b), 0.35 m^2 s^{-1} does not agree with the electron diffusivity of Cu. Therefore, the fact that a pure diffusive model can produce an apparently linear relationship between thickness and travel time implies how difficult it is to determine a transport mechanism based on a simple functional form of parameters. The situation is even more complicated due to the presence of various heat transfer processes, e.g., direct optical excitation and electron-phonon interactions.

Ref. [27] reported the magnetization dynamics of [Co/Pt] multilayers induced by ballistic transport in a Cu layer. However, the results can also be explained by considering “pure thermal transport.” As can be seen in Figure 4.11(a), the 3TM calculation shows excellent agreement

with the measurement data taken from Ref. [27] without any adjustable parameter. I use the same parameters for Cu as in Ref. [27] but for Pt and [Co/Pt], I use the values derived in this work (see Table 4.3).

The authors in Ref. [27] also argue that diffusive thermal transport results in lower efficiency of demagnetization compared with ballistic transport of hot electrons. However, the 3TM can reproduce the maximum efficiency ($\Delta\theta_{max}/\theta$) for the samples with Cu thickness > 150 nm in Ref. [27]. (see Fig. 4.11(b)). The maximum efficiency calculated by the 3TM as a function of Cu thickness is normalized to give $\Delta\theta_{max}/\theta$=2.6% for Cu of 250 nm thickness. This efficiency of 2.6% corresponds to an absorbed fluence of 20 J m^{-2}, given $(d\theta/\theta)/T \approx 10^{-3}$ K^{-1} for Co. The 3TM calculation deviates from the data for $\Delta\theta_{max}/\theta > 10\%$, i.e., $\Delta T_m > 100$ K. This deviation can be attributed to the fact that the temperature excursion is large enough that the materials parameters, e.g., electron and magnon heat capacities, are not constant, and the assumption of linear response is no longer valid. [6] The efficiency ($\Delta\theta_{max}/\theta$) calculated by the 3TM decreases exponentially with the thickness of Cu, with a characteristic length scale of 45 nm, as shown in Fig. 4.11(b). This length-scale is ≈70% of l_{ep} of Cu ≈ 63 nm. [28]

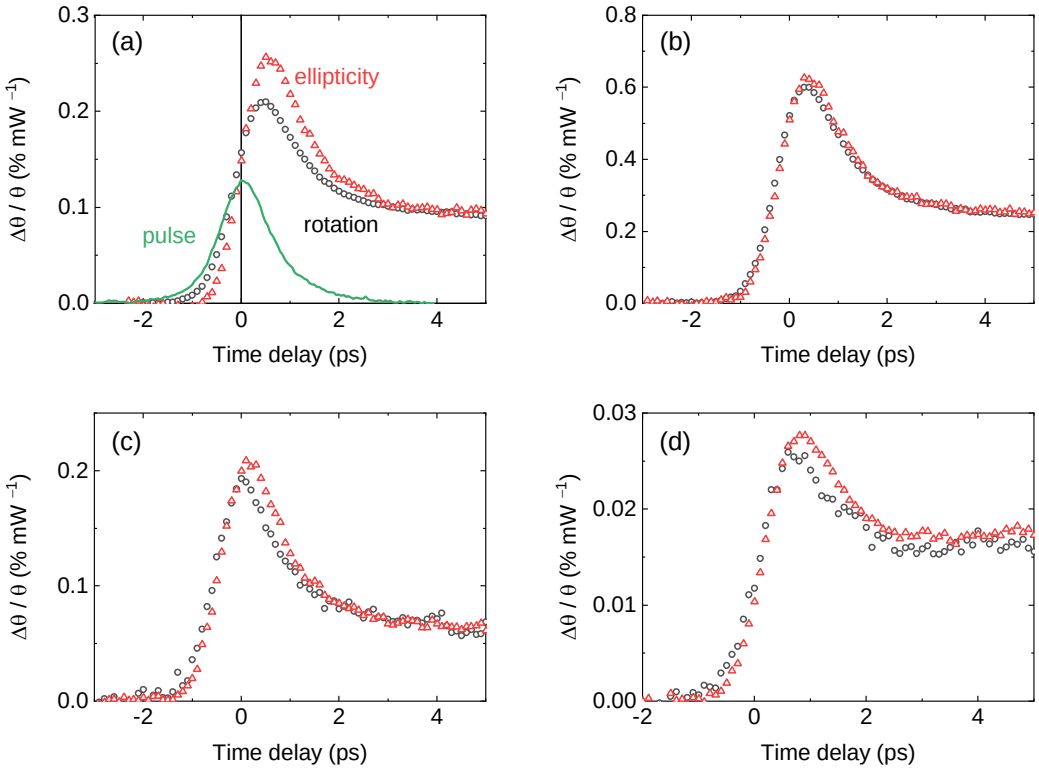

Figure 4.7. Kerr rotation (black) and ellipticity (red) divided by a pump power of (a) Pt(1)/[Pt(1)/Co(0.5)]$_6$/Pt(10)/sapphire, (b) Pt(2)/Co(0.8)/Pt(4)/sapphire, and (c-d) Pt(42)/Co(0.8)/Pt(4)/sapphire, where pump is incident on (c) Pt(42) surface and (d) substrate.

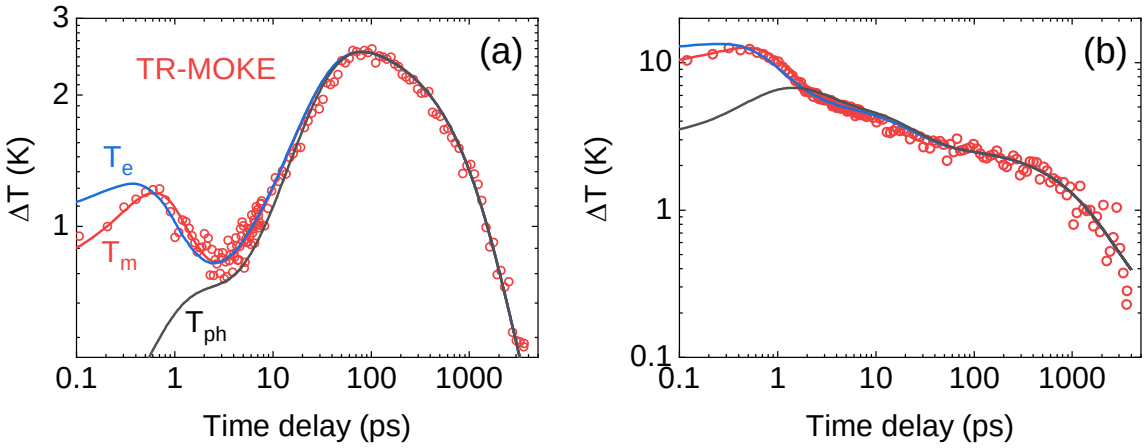

Figure 4.8. Temperature evolutions in Pt(2)/Co(0.8)/Pt(2)/Ru(50)/sapphire compared with measured TR-MOKE data with probe incident on top Pt surface and pump on (a) sapphire substrate and (b) the top Pt surface.

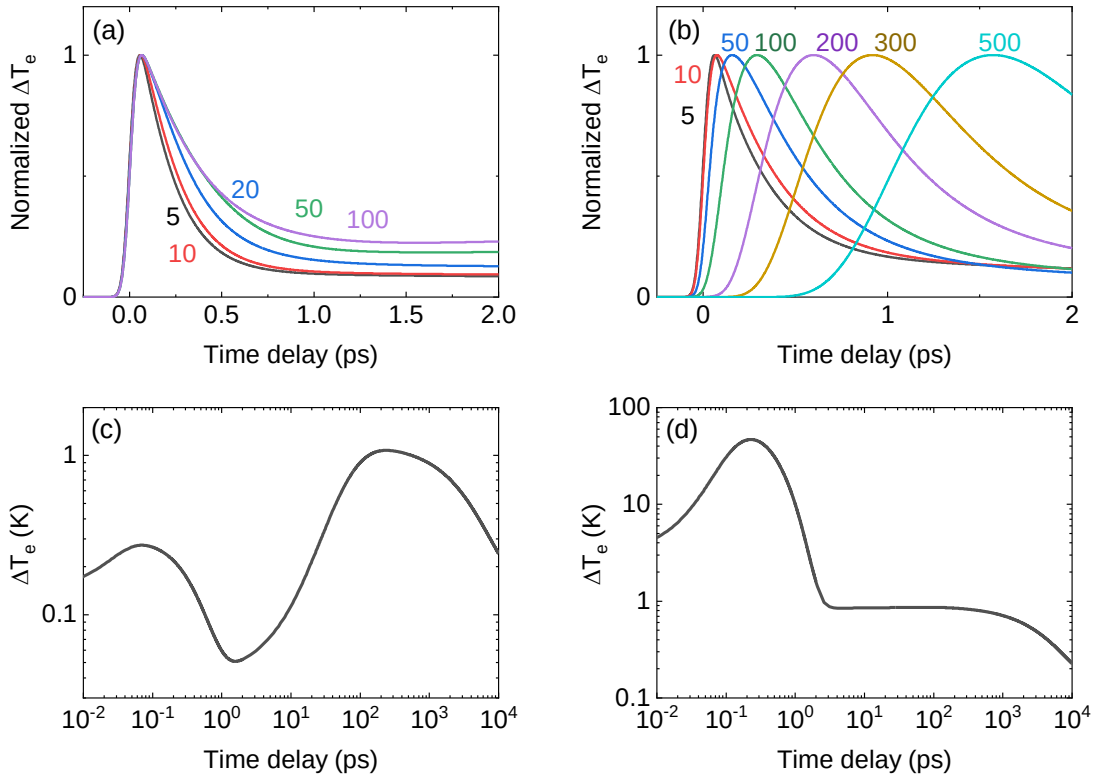

Figure 4.9. Electron temperatures at the bottom surface of (a) Pt and (b) Cu on sapphire substrates calculated using a two-temperature model. The numbers represent the thickness of either a Pt or Cu layer. (c,d) Electron temperatures at the bottom surface of a 100-nm-thick (c) Pt and (d) Cu layer.

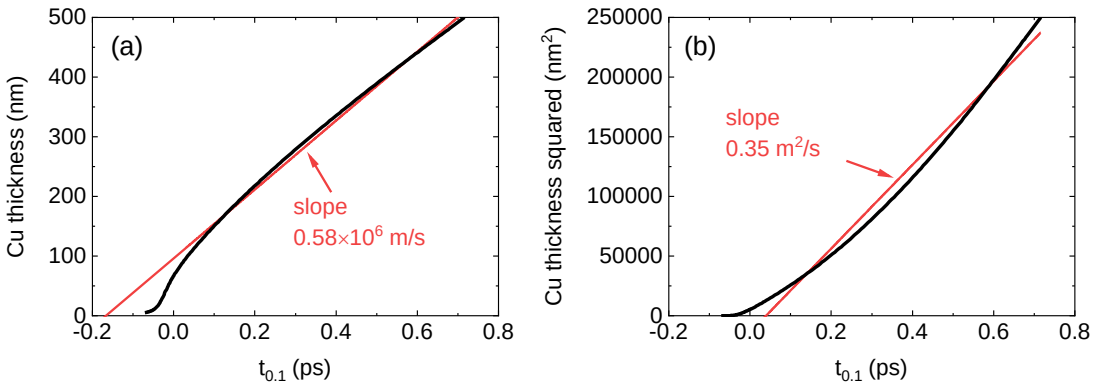

Figure 4.10. Onset-time ($t_{0.1}$) of electron temperature at the bottom surface of a Cu layer of different thicknesses plotted versus (a) thickness and (b) thickness-squared of the Cu layer. Black lines are the onset-times extracted from Figure 4.9(b) and red lines are linear fits.

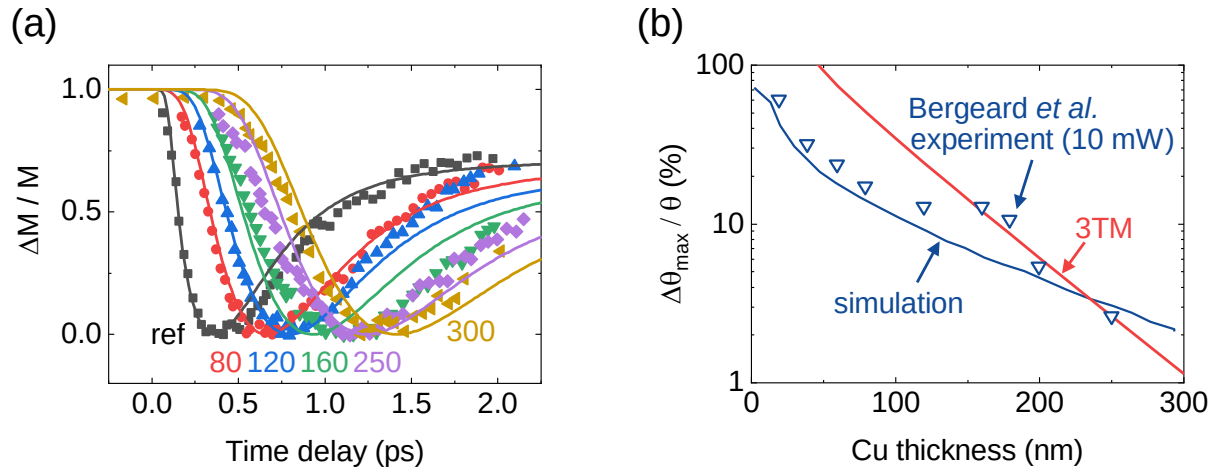

Figure 4.11. Magnetization dynamics in Pt(3)/Cu(*d*)/[(Co(0.6)/Pt(1.1)]2/Pt(3)/Ta(3)/glass (d=0-300 nm) in Bergeard *et al.* [27] analyzed with a three-temperature model. (a) Demagnetization of [Co/Pt] for various Cu thicknesses. Data (symbols) are taken from Figure 1(b) in Ref. [27]. Solid lines are 3TM calculation results. The numbers represent the thickness of Cu (*d*) in nm and "ref" is for *d*=0. (b) Maximum demagnetization vs. Cu thickness. The experimental data (blue symbol) and simulation curve (blue line) are taken from Figure 3(b) and Figure 4(b), respectively, for a laser power of 10 mW in Ref. [27]. Red line represents the 3TM calculation results.

	Pt	**Co**	**Al_2O_3**
C_{total} (10^6 J m^{-3} K^{-1})	2.82 [a]	3.75	3.08
γ_e (J m^{-3} K^{-2})	400 [b]	680 [c]	–
C_m (10^6 J m^{-3} K^{-1})	–	0.02 (bulk) [d]	–
Λ_{ph} (W m^{-1} K^{-1})	7 [e]	14 [f]	33
Λ_e (W m^{-1} K^{-1})	50 [g]	20 [g]	–
g_{ep} (W m^{-3} K^{-1})	$(6\pm1)\times10^{17}$	$(2.0\pm0.2)\times10^{18}$	–
$\tau_{em}=C_m/g_{em}$ (ps)	–	0.23±0.05	–
refractive index, $\tilde{n}$	$2.7+i5.9$ [h]	$2.5+i4.9$ [i]	1.76
$d\tilde{n}/dT$	$2.6\times10^{-4}+i(-3\times10^{-4})$ [j]	$2.6\times10^{-4}+i(-3\times10^{-4})$ [j]	–

Table 4.1. Materials parameters that are used for calculating the three-temperature model.

a. Reference [17]
b. Reference [16]
c. Reference [8]
d. Reference [7]
e. Reference [29]
f. Λ_{ph} of Co is assumed to be the same as Λ_{ph} of Ni in Reference [30].
g. Electrical conductivities of Pt and Co are measured by using a four-probe method on a 50-nm-thick Pt single layer and a 10-nm-thick Co layer capped with Pt 2 nm on sapphire substrates, respectively. The electronic thermal conductivities are derived via the Wiedemann-Franz law.
h. Reference [28]
i. Reference [20]
j. Reference [15]. The $d\tilde{n}/dT$ of Co is not available and assumed to be the same as that of Pt as the thermoreflectance, dR/dT, of Co and Pt are the same within the experimental uncertainty for 785 nm wavelength. [15]

Sample structure	Pump	Pt	Co	Pt	Total absorbance	Static Kerr rotation (mrad)
$Pt(2)/Co(10)/Al_2O_3$	Front	23.1%	76.9%	–	0.322	-
$Pt(2)/Co/Pt(4)/Al_2O_3$	Front	28.8 %	10.0 %	61.2 %	0.305	1.7
$Pt(42)/Co/Pt(4)/Al_2O_3$	Front	98.3 %	0.2 %	1.5 %	0.220	0.4
	Back	63.1 %	3.5 %	33.2 %	0.314	
$Pt(16)/Co/Pt(24)/Al_2O_3$	Front	75.4 %	1.2 %	23.4 %	0.222	0.2
	Back	12.8 %	0.7 %	86.5 %	0.319	

Table 4.2. Absorbance and static Kerr rotation of Pt/Co/Pt samples. Fractional absorbance of each layer in the Pt/Co/Pt samples and total absorbance calculated by a transfer matrix method. "Front/Back" indicates the surface on which the pump pulse is incident. Static Kerr rotation is measured when the probe pulse is incident on the surface that is closer to the Co layer.

	Cu	[Co/Pt]
C_{total} (10^6 J m^{-3} K^{-1})	3.45	3.10
γ_e (J m^{-3} K^{-2})	100	530
C_m (10^6 J m^{-3} K^{-1})	–	0.2
Λ_{ph} (W m^{-1} K^{-1})	10	10
Λ_e (W m^{-1} K^{-1})	300	20
g_{em} (W m^{-3} K^{-1})	7.5×10^{16}	2×10^{18}
g_{em} (W m^{-3} K^{-1})	–	9×10^{17}
refractive index	$0.25+i5.03$	$2.67+i5.19$

Table 4.3. Materials parameters for Pt(3)/Cu(d)/[Co/Pt](4)/Pt(3)/Ta(3)/glass (d=0-300 nm). [Co/Pt] is Co(0.6)/[Pt(1.1)/Co(0.6)]$_2$. For [Co/Pt], C_{total} and γ_e are volumetrically averaged values; C_m, g_{ep}, and g_{em} are the values derived for Co in this work, and others are from Ref. [27].

4.5. Reference

[1] J. Hohlfeld, S.-S. Wellershoff, J. Güdde, U. Conrad, V. Jähnke, and E. Matthias, *Chem. Phys.* **251**, 237 (2000).

[2] C. Lei, M. Bauer, K. Read, R. Tobey, Y. Liu, T. Popmintchev, M. M. Murnane, and H. C. Kapteyn, *Phys. Rev. B* **66**, 245420 (2002).

[3] A. P. Caffrey, P. E. Hopkins, J. M. Klopf, and P. M. Norris, *MTE Microscale Thermophys. Eng.* **9**, 365 (2005).

[4] G.-M. Choi, C.-H. Moon, B.-C. Min, K.-J. Lee, and D. G. Cahill, *Nat. Phys.* **11**, 576 (2015).

[5] J. Kimling and D. G. Cahill, *Phys. Rev. B* **95**, 14402 (2017).

[6] J. Kimling, J. Kimling, R. B. Wilson, B. Hebler, M. Albrecht, and D. G. Cahill, *Phys. Rev. B - Condens. Matter Mater. Phys.* **90**, 224408 (2014).

[7] Z. Li, S. Bigdeli, H. Mao, Q. Chen, and M. Selleby, *Phys. Status Solidi* **254**, 1600231 (2017).

[8] G. R. Stewart, *Rev. Sci. Instrum.* **54**, 1 (1983).

[9] R. B. Wilson, B. A. Apgar, W. P. Hsieh, L. W. Martin, and D. G. Cahill, *Phys. Rev. B - Condens. Matter Mater. Phys.* **91**, 115414 (2015).

[10] G. A. Slack, *Phys. Rev.* **126**, 427 (1962).

[11] Y. K. Koh, A. S. Lyons, M. H. Bae, B. Huang, V. E. Dorgan, D. G. Cahill, and E. Pop, *Nano Lett.* **16**, 6014 (2016).

[12] P. J. Metaxas, J. P. Jamet, A. Mougin, M. Cormier, J. Ferré, V. Baltz, B. Rodmacq, B. Dieny, and R. L. Stamps, *Phys. Rev. Lett.* **99**, 217208 (2007).

[13] R. M. Rowan-Robinson, A. T. Hindmarch, and D. Atkinson, *Phys. Rev. B* **90**, 104401 (2014).

[14] H. Ibach and C. M. Schneider, *Phys. Rev. B* **98**, 14413 (2018).

[15] R. B. Wilson, B. A. Apgar, L. W. Martin, and D. G. Cahill, *Opt. Express* **20**, 28829 (2012).

[16] Z. Lin, L. V. Zhigilei, and V. Celli, *Phys. Rev. B - Condens. Matter Mater. Phys.* **77**, 075133 (2008).

[17] J. W. Arblaster, *Platin. Met. Rev.* **38**, 119 (1994).

[18] L. G. Liu, T. Takahashi, and W. A. Bassett, *J. Phys. Chem. Solids* **31**, 1345 (1970).

[19] J. N. Plendl and P. J. Gielisse, *Phys. Status Solidi* **42**, 681 (1970).

[20] R. B. Wilson, Y. Yang, J. Gorchon, C. H. Lambert, S. Salahuddin, and J. Bokor, *Phys. Rev. B* **96**, 045105 (2017).

[21] B. Y. Mueller and B. Rethfeld, *Phys. Rev. B - Condens. Matter Mater. Phys.* **87**, 035139 (2013).

[22] M. Bauer, A. Marienfeld, and M. Aeschlimann, *Prog. Surf. Sci.* **90**, 319 (2015).

[23] B. Koopmans, M. Van Kampen, J. T. Kohlhepp, and W. J. M. De Jonge, *Phys. Rev. Lett.* **85**, 844 (2000).

[24] I. Razdolski, A. Alekhin, U. Martens, D. Bü Rstel, D. Diesing, M. Münzenberg, U. Bovensiepen, and A. Melnikov, *J. Phys. Condens. Matter* **29**, 174002 (2017).

[25] J. Wieczorek, A. Eschenlohr, B. Weidtmann, M. Rösner, N. Bergeard, A. Tarasevitch, T. O. Wehling, and U. Bovensiepen, *Phys. Rev. B* **92**, 174410 (2015).

[26] S. D. Brorson, J. G. Fujimoto, and E. P. Ippen, *Phys. Rev. Lett.* **59**, 1962 (1987).

[27] N. Bergeard, M. Hehn, S. Mangin, G. Lengaigne, F. Montaigne, M. L. M. Lalieu, B. Koopmans, and G. Malinowski, *Phys. Rev. Lett.* **117**, 147203 (2016).

[28] G.-M. Choi, R. B. Wilson, and D. G. Cahill, *Phys. Rev. B* **89**, 64307 (2014).

[29] M. J. Duggin, *J. Phys. D. Appl. Phys.* **3**, L21 (1970).

[30] X. Zheng, D. G. Cahill, P. Krasnochtchekov, R. S. Averback, and J. C. Zhao, *Acta Mater.* **55**, 5177 (2007).

CHAPTER 5
THERMAL TRANSPORT IN MAGNETIC TUNNEL JUNCTIONS

5.1. Sample characterization

The samples with tunnel barriers are provided from the group of Dr. Kuschel at Bielefeld University in Germany. The sample stacks are Ru(50)/oxide(2)/$Co_{40}Fe_{40}B_{20}$(1)/Ta(5)/substrate and Ru(50)/oxide(2)/Co(0.7)/Pt(5)/substrate, in which the oxide layer is either MgO or $MgAl_2O_4$ of 2 nm thickness, and the substrate is double-side polished MgO(001). All the samples are prepared by magnetron sputtering. The samples with CoFeB are post-annealed at 350°C for 1 hr to crystallize CoFeB and oxide. The details of sample preparation processes are described in Ref. [1]. All of the four samples exhibit perpendicular magnetic anisotropy. I prepare Pt(2)/$Co_{40}Fe_{40}B_{20}$(6.5) on *c*-Al_2O_3 substrate using a two-target DC magnetron sputtering deposition system for TR-QMOKE measurement. This relatively thick CoFeB layer displays in-plane easy axis due to shape anisotropy.

The thickness of layers in the samples are determined by using Rutherford backscattering spectrometry (RBS, NEC Pelletron). I use ^{4}He ions of 2 MeV as an incident ion beam. The incident angle of the ion beam, exit angle, and corresponding scattering angle are 22.5°, 52.5°, and 150°, respectively. The detector resolution is typically 17−18 keV. The measured RBS spectra and calculated spectra using *SIMNRA* software are shown in Figure 5.1. The *y*-axis is the normalized intensity, i.e., intensity in counts divided by the number of incident particles times solid angle of the detector. The plateau at energy < 1050 keV is from MgO substrate; the largest peak at 1600−1750 keV is from a 50-nm-thick Ru layer at the top; the peak at 1480 keV is from

Co in Fig. 5.1(a) and from Co and Fe in Fig. 5.1(b); the peak at 1780 keV in Fig. 5.1(a) is from Pt and the peak at 1750 keV in Fig. 5.1(b) is from Ta. The peak at 1200 keV in Fig. 5.1(a) is not identified. The thicknesses derived from RBS agree with the nominal thicknesses within 10% and are used as inputs in thermal analysis. The thickness of Pt(2)/CoFeB(6.5) is determined by using X-ray reflectivity (XRR).

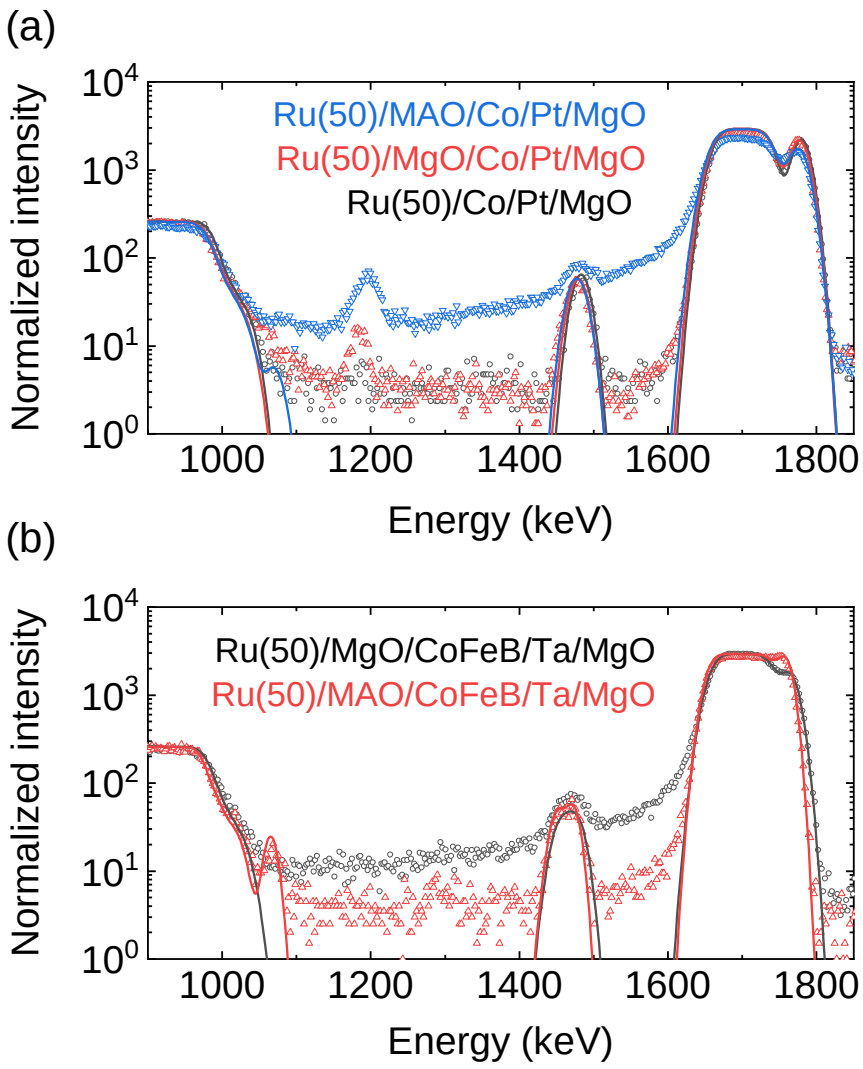

Figure 5.1. Rutherford backscattering spectra of samples with (a) Co and (b) CoFeB. The normalized intensity in *y*-axis is the intensity in counts divided by total ion dose, i.e., the number of incident particles times the solid angle of the detector. Open symbols are measured data and solid lines are calculated spectra.

5.2. Non-equilibrium thermal transport in CoFeB alloy

Magnetization dynamics of $Co_{40}Fe_{40}B_{20}$ alloy is measured via TR-QMOKE with magnetic field ≈0.26 T applied parallel to the sample plane. The CoFeB film having in-plane magnetic easy axis undergoes both precession and demagnetization of the magnetization upon the incidence of a pump pulse. The sum of TR-QMOKE signals with probe polarizations at +45° and −45° relative to the applied magnetic field represents the out-of-plane component of precessing magnetization, as shown in Figure 5.2. The precession frequency (f) is 17.5 GHz and the time constant of decay in precession amplitude (τ) is (540±160) ps. According to the Kittel's formula in Eq. (5.1), the saturation magnetization (M_S) is estimated as $(1.0\pm0.2)\times10^6$ A m^{-1}. The Gilbert damping parameter (α) is 0.012±0.004 derived from the time constant via Eq. (5.2).

$$f = \frac{\gamma_e \mu_0}{2\pi}\sqrt{H(H+M_S)} \tag{5.1}$$

$$\alpha = \frac{1}{\tau[\gamma_e \mu_0 (H + M_S/2)]} \tag{5.2}$$

γ_e and μ_0 are electron gyromagnetic ratio and vacuum permeability, respectively.

The difference of TR-MOKE signal for probe polarizations at +45° and −45° relative to the applied magnetic field represents demagnetization of CoFeB and is shown in Figure 5.3. The unknown parameters for calculating temperature responses are g_{ep} and $\tau_{em}=C_m/g_{em}$ of CoFeB. I determine g_{ep} of CoFeB from the magnitude of the initial temperature-rise of T_m, and τ_{em} from the time-delay dependence of T_m. However, the measured TR-QMOKE data cannot be explained by a single set of g_{ep} and τ_{em} values. The temperatures in Fig. 5.3(a-b) are calculated by the 3TM with $g_{ep}=11\times10^{17}$ W m^{-3} K^{-1} and τ_{em}=0.3 ps, and the temperatures in Fig. 5.3(c) are with $g_{ep}=6\times10^{17}$ W m^{-3} K^{-1} and τ_{em}=2 ps. The discrepancy between the measured data and the 3TM calculations is not attributed to the change of magneto-optical constants induced by direct optical

excitation. This is supported by the fact that the Kerr rotation and ellipticity show the same magnetization dynamics, as shown in Figure 5.4.

It is not clear yet the reason why the magnetization dynamics of CoFeB cannot be explained by a single set of carrier coupling parameters. For reference, g_{ep} and τ_{em} of Co that I determine in Chap. 4 are 6×10^{18} W m^{-3} K^{-1} and 0.2 ps, respectively. Ref. [2] reported g_{ep} of Co and Fe as both 4×10^{18} W m^{-3} K^{-1}. I note that heat transfer across the tunnel barrier occurs at time delay from 10 ps to 4 ns, and the lower limits of carrier coupling parameters have a negligible effect on determination of the thermal conductance of oxide tunnel barriers, as will be discussed in the next section.

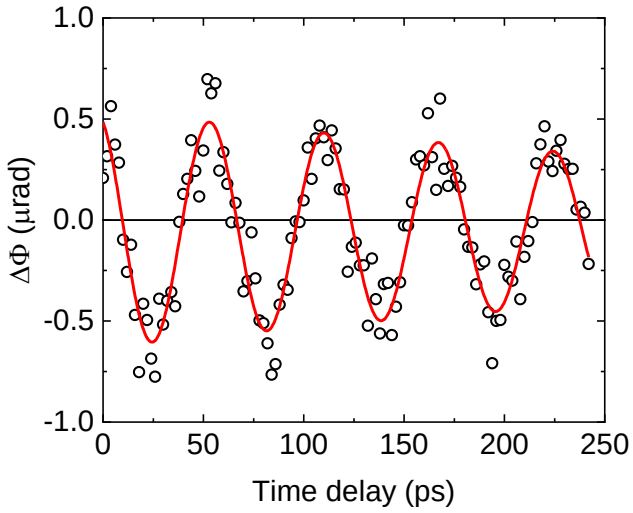

Figure 5.2. Out-of-plane component of precession motion of magnetization in Pt(2)/CoFeB(6.5) measured via time-resolved quadratic magneto-optical Kerr effect (TR-QMOKE) with applied in-plane magnetic field ≈0.26 T. Open symbol is the sum of TR-QMOKE data with probe polarizations of +45° and −45° relative to the applied magnetic field. Red solid line is a fit with a frequency of 17.5 GHz and a time constant of exponential decay of (540±160) ps.

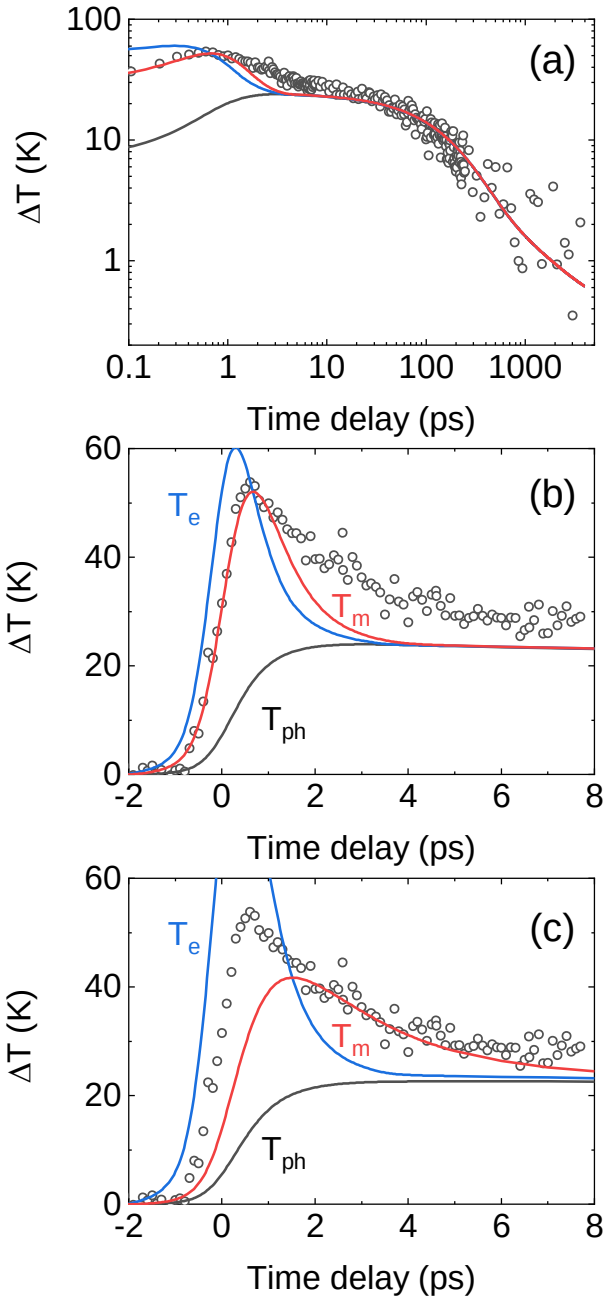

Figure 5.3. Magnetization dynamics in Pt(2)/CoFeB(6.5) measured by TR-QMOKE in (a) log-log axes and (b,c) linear axes at short delay times. Open symbol is the difference of TR-QMOKE data with probe polarizations of +45° and −45° relative to the applied magnetic field. Solid lines are simulated electron (blue), magnon (red), and phonon (black) temperatures of CoFeB by a 3TM. The fitted values of g_{ep} and $\tau_{em}=C_m/g_{em}$ of CoFeB are (a,b) $g_{ep}=11\times10^{17}$ W m^{-3} K^{-1} and $\tau_{em}=0.3$ ps and (c) $g_{ep}=6\times10^{17}$ W m^{-3} K^{-1} and $\tau_{em}=2$ ps.

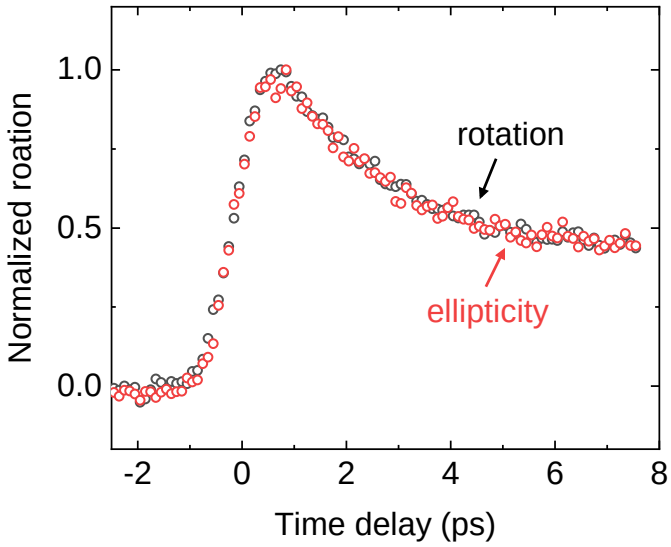

Figure 5.4. Normalized Kerr rotation (black) and ellipticity (red) of Pt(2)/CoFeB(6.5) measured by TR-QMOKE with applied in-plane magnetic field ≈ 0.3 T. The maximum Kerr rotation and ellipticity are 4.3 μrad and 4.1 μrad, respectively.

5.3. Thermal conductance of oxide tunnel barriers

I determine the thermal conductance of an oxide tunnel barrier, which includes the thermal conductivity of the thin oxide layer and a series of thermal conductance of the two interfaces, using the samples with oxide tunnel barriers of 2 nm thickness. The conventional geometry of TDTR having pump and probe beams incident on an opaque metal surface investigates cooling of the surface temperature and is most sensitive to a thermally insulating layer. In my sample stacks, the lowest thermal conductance is displayed by the oxide tunnel barriers and the interface between a metal seed layer, i.e., Ta or Pt, and a MgO substrate. Thus, from this TDTR measurement, I can only determine the serial thermal conductance combining the oxide tunnel barrier and the interface with a substrate, which I refer to as G_{tot}.

Figure 5.5 shows TDTR measurements of the three samples with either MgO or $MgAl_2O_4$ (MAO) tunnel barriers. For the analysis, [3] the samples are modeled as "Ru/substrate," where the interface between Ru and a MgO substrate includes an oxide layer (MgO or MAO), a ferromagnetic layer (Co or CoFeB), and a seed layer (Ta or Pt). The heat capacities of all the components are considered in the thermal model. The materials parameters used for the thermal model are presented in Table 5.1. The total thermal conductance (G_{tot}) between Ru and substrate derived from TDTR measurement is shown in Table 5.2. For reference, I prepare samples without oxide tunnel barriers, i.e., Ru(50)/Co(0.7)/Pt(5)/MgO and Ru(50)/Ta(5)/MgO. The TDTR measurements on the reference samples are most sensitive to the interface thermal conductance between the seed layer (Pt or Ta) and MgO substrate (G_{sub}). G_{sub} determined from the reference samples is (200±50) MW m^{-2} K^{-1}.

To separately determine the thermal conductance of oxide tunnel barriers (Λ_{oxide}) and the interface thermal conductance between a metal seed layer (Ta or Pt) and MgO substrate (G_{sub}), I

perform TR-MOKE measurement with pump incident on Ru surface and probe on MgO substrate. The TR-MOKE signal informs the magnon temperature (T_m), in an ultrathin ferromagnetic layer. Since the ferromagnetic layer, i.e., Co or CoFeB, is located between an oxide tunnel barrier and a substrate, Λ_{oxide} and G_{sub} affects the magnon temperature in CoFeB differently: the higher Λ_{oxide} contributes heating of T_m, while the higher G_{sub} contributes cooling of T_m. The different roles of the two parameters on T_m are quantitatively presented in sensitivity plots in Figure 5.6.

Most of the pump energy is absorbed in Ru as the Ru layer of 50 nm thickness is thicker than the optical absorption depth of Ru, ≈13 nm. (See Table 5.1) Heat transport from Ru across an oxide tunnel barrier into CoFeB occurs at time delays longer than 10 ps. The temperature evolution in CoFeB at time delay < 10 ps is due to direct optical excitation of CoFeB and dominated by carrier coupling parameters of CoFeB. For determination of Λ_{oxide} and G_{sub}, the TR-MOKE data of time delay between 10 ps and 4 ns is compared with the 3TM calculations. In this analysis, only the in-phase signal of TR-MOKE is used, since the heat accumulation in metal layers on MgO substrate is negligible and thus the out-of-phase signal is negligible. To account for the divergence of the pump beam size about 16% across the linear delay stage, the in-phase voltage is multiplied by $(1+0.16 \cdot t_d/3600)$, where t_d is the time delay in ps.

Figure 5.7 shows the measured TR-MOKE data and the 3TM calculations. The oxide tunnel barriers effectively block the passage of electrons and magnons. Therefore, across the oxide tunnel barriers, non-equilibrium among electrons, phonons, and magnons exists until about time delay of 1 ns. The best-fit of Λ_{oxide} and G_{sub} is obtained with a constraint that the total conductance of an oxide tunnel barrier and its two interfaces is confined to G_{tot} from TDTR measurement in Fig. 5.5. The ranges of Λ_{oxide} and G_{sub} are evaluated with the criterion of

$\sigma^2 \leq 2\sigma_{min}^2$ where σ^2 is the squared of the sum of the residuals and is shown in Figure 5.8. The shaded area in Fig. 5.8 represents G_{sub} determined from the control samples without oxide barriers, i.e., G_{sub} =(200±50) MW m^{-2} K^{-1}. The best-fit of Λ_{oxide} and G_{sub} is shown in Table 5.2.

The effective thermal conductivity of MgO with a Co ferromagnetic layer is 0.5−0.8 W m^{-1} K^{-1} and that of MgO with CoFeB is 0.23−0.5 W m^{-1} K^{-1}. The effective thermal conductivity of $MgAl_2O_4$ is 0.4−0.8 W m^{-1} K^{-1}, as can be seen in Fig. 5.8. The difference of the effective thermal conductivity between MgO and $MgAl_2O_4$ barriers is not obviously shown. The effective thermal conductivity of MgO in the as-deposited sample with Co is slightly bigger than that in the annealed sample with CoFeB, but they agree within experimental uncertainty.

The effective thermal conductivity of the 2-nm-thick oxide layers is more than an order of magnitude smaller than the thermal conductivity of bulk or thin films: the bulk thermal conductivity of MgO and $MgAl_2O_4$ are 48 W m^{-1} K^{-1} and 22 W m^{-1} K^{-1}, respectively, at 300 K. [4] Lee *et al.* [5] reported thermal conductivity of a sputtered MgO thin film with average grain size of 3−7 nm and micron-thickness as 4 W m^{-1} K^{-1} at 300 K, by using a 3ω method. Huebner *et al.* [6] inferred the thermal conductivity of oxide tunnel barriers by comparing the measured TMS voltage across the MTJ stacks and a temperature profile calculated from finite-element modeling. They reported the effective thermal conductivity of MgO and $MgAl_2O_4$ as 5.8 W m^{-1} K^{-1} and 0.7 W m^{-1} K^{-1}, respectively.

I expect that the thermal conductivity of MgO of 2-nm-thickness would be similar to the thermal conductivity of nanocrystalline MgO films reported in Ref. [5]. The low effective thermal conductivity of the oxide tunnel barriers can be attributed to the dominant contributions from the thermal conductance of the two interfaces, i.e., Ru/oxide and oxide/ferromagnet. Wilson *et al.* [7] showed that the upper limit of interface thermal conductance is determined by

intrinsic phonon properties of materials, and linearly dependent on the product of the Debye velocity and heat capacity. According to Ref. [7], a clean interface of Al/MgO shows the interface thermal conductance of 0.5 GW m^{-2} K^{-1}.

The Debye temperatures of Co and Fe are 460 K and 477 K, respectively, and similar to the Debye temperature of Al, which is 433 K. [8] The Debye temperature of Ru is 555 K. [8] The Debye temperatures of MgO and $MgAl_2O_4$ are 950 K and 900 K, respectively. [4] Thus, I can assume that the upper limit of thermal conductance from the two interfaces of the oxide barriers is ≈ 0.25 GW m^{-2} K^{-1}., corresponding to the effective thermal conductivity of 0.5 W m^{-1} K^{-1}. This demonstrates that the effective thermal conductivity of the oxide barriers is dominated by the interfacial contributions. The result is in good agreement with first-principles calculations of Ref. [9] taking account of the interfacial heat transport, which predicts the thermal conductance across an MgO tunnel barrier in a Fe/MgO/Fe MTJ as 0.2 GW m^{-2} K^{-1}.

In summary, I report the effective thermal conductivity of the oxide tunnel barriers of MgO and $MgAl_2O_4$ as 0.2−0.8 W m^{-1} K^{-1}. This is significantly lower than the thermal conductivity of MgO ≈ 4 W m^{-1} K^{-} that is used for evaluating the tunnel-magneto Seebeck effect in the original work, [10] thus overestimating the performance. Moreover, electrons and phonons are not in thermal equilibrium across the tunnel barrier, and it should be considered for estimating the temperature difference.

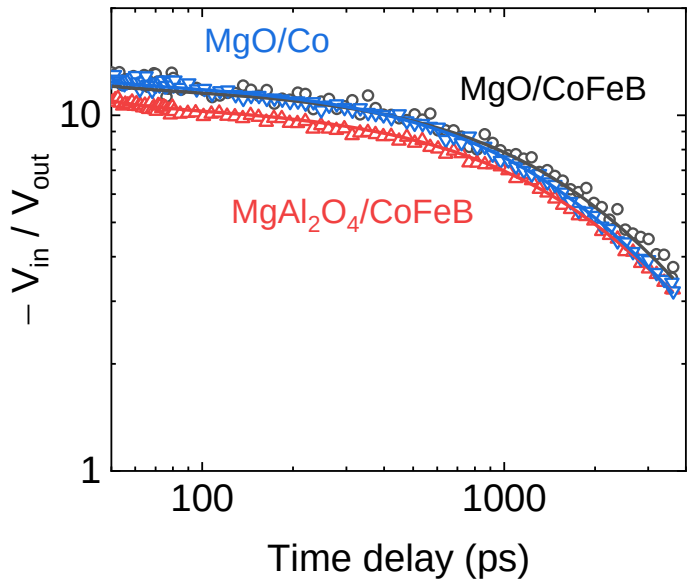

Figure 5.5. Time-domain thermoreflectance (TDTR) measurement of samples with oxide tunnel barriers with pump and probe on Ru surface. Open symbols are measured TDTR signal and solid lines are the best-fit.

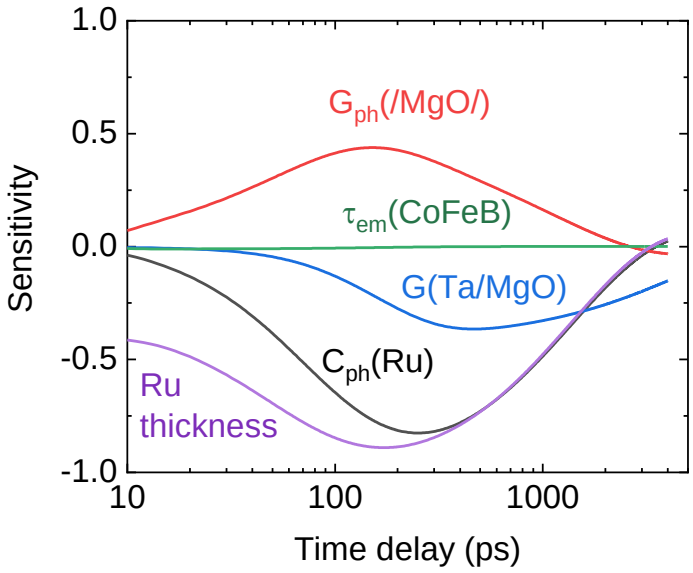

Figure 5.6. Sensitivity of magnon temperature in CoFeB to materials parameters when a pump pulse is incident on Ru surface in Ru(50)/MgO(2)/CoFeB(1)/Ta(5)/substrate sample.

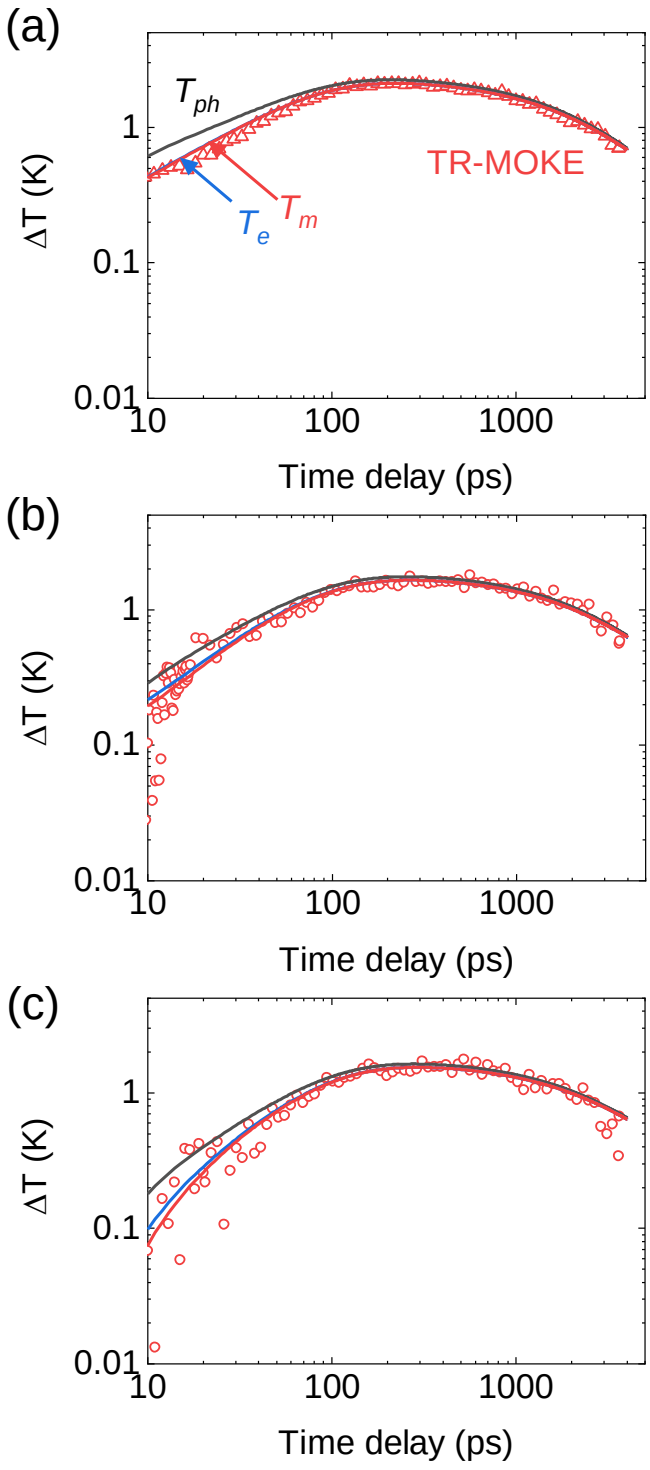

Figure 5.7. Temperature evolutions in (a) Co in Ru/MgO/Co/Pt/substrate, (b) CoFeB in Ru/MgO/CoFeB/Ta/substrate, and (c) CoFeB in Ru/MAO/CoFeB/Ta/substrate when pump is incident on Ru surface. Open symbol is TR-MOKE data measured with probe on substrate. Solid lines are simulated electron (blue), magnon (red), and phonon (black) temperatures of either Co or CoFeB by a 3TM.

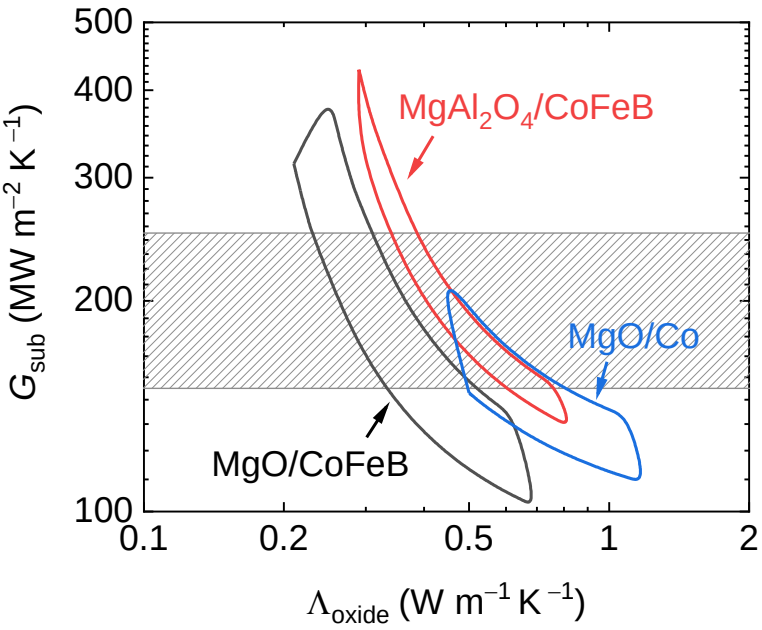

Figure 5.8. Best-fit of effective thermal conductivity of oxide tunnel barriers (Λ_{oxide}) and interface thermal conductance (G_{sub}) between a seed layer (Pt or Ta) and MgO substrate for TR-MOKE measurement with pump on Ru surface and probe on substrate. The shaded area represents the range of G_{sub} determined by TDTR measurement on the samples without tunnel barriers.

	Ru	Co	CoFeB	Pt	Ta	MgO	MAO
C_{tot} (10^6 J m^{-3} K^{-1})	2.94	3.55	3.34	2.82	2.33	3.35	2.97
γ_e (J m^{-3} K^{-2})	371	680	680	400	400	-	-
g_{ep} (10^{17} W m^{-3} K^{-1})	1	20	20	6	6	-	-
τ_{em} (ps)	-	0.2	1.3	-	-	-	-
Λ_{ph} (W m^{-1} K^{-1})	7	14	14	7	7	45	-
Λ_e (W m^{-1} K^{-1})	70	50	50	50	50	-	-
n+*i*k at 785 nm	5.2+ 4.9*i*	2.5+ 4.8*i*	2.5+ 4.8*i*	2.7+ 5.9*i*	1.1+ 3.5*i*	1.73	1.73

Table 5.1. Materials parameters for thermal modeling.

	G_{tot} (MW m^{-2} K^{-1})	Λ_{oxide} (W m^{-1} K^{-1})	G_{sub} (MW m^{-2} K^{-1})
Ru(50)/MgO(2)/Co(0.7)/Pt(5)/MgO	100±8	0.68	144
Ru(50)/MgO(2)/CoFeB(1)/Ta(5)/MgO	86±8	0.33	183
Ru(50)/MAO(2)/CoFeB(1)/Ta(5)/MgO	98±8	0.38	178

Table 5.2. Best-fit of total thermal conductance (G_{tot}), effective thermal conductivity of oxide tunnel barriers (Λ_{oxide}), and interface thermal conductance (G_{sub}) with MgO substrate.

5.4. Reference

[1] T. Huebner, U. Martens, J. Walowski, A. Boehnke, J. Krieft, C. Heiliger, A. Thomas, G. Reiss, T. Kuschel, and M. Münzenberg, *Phys. Rev. B* **96**, 214435 (2017).

[2] R. Chimata, A. Bergman, L. Bergqvist, B. Sanyal, and O. Eriksson, *Phys. Rev. Lett.* **109**, (2012).

[3] D. G. Cahill, *Rev. Sci. Instrum.* **75**, 5119 (2004).

[4] G. A. Slack, *Phys. Rev.* **126**, 427 (1962).

[5] S. M. Lee, D. G. Cahill, and T. H. Allen, *Phys. Rev. B* **52**, 253 (1995).

[6] T. Huebner, U. Martens, J. Walowski, M. Münzenberg, A. Thomas, G. Reiss, and T. Kuschel, *J. Phys. D. Appl. Phys.* **51**, 224006 (2018).

[7] R. B. Wilson, B. A. Apgar, W. P. Hsieh, L. W. Martin, and D. G. Cahill, *Phys. Rev. B - Condens. Matter Mater. Phys.* **91**, 115414 (2015).

[8] G. R. Stewart, *Rev. Sci. Instrum.* **54**, 1 (1983).

[9] J. Zhang, M. Bachman, M. Czerner, and C. Heiliger, *Phys. Rev. Lett.* **115**, 037203 (2015).

[10] M. Walter, J. Walowski, V. Zbarsky, M. Münzenberg, M. Schäfers, D. Ebke, G. Reiss, A. Thomas, P. Peretzki, M. Seibt, J. S. Moodera, M. Czerner, M. Bachmann, and C. Heiliger, *Nat. Mater.* **10**, 742 (2011).

CHAPTER 6
CONCLUSIONS

In this dissertation, I report the three-dimensional thermal conductivities of BP, WTe_2, and ReS_2 along the three crystalline axes at room temperature for the first time. The trend of thermal conductivity in 2D materials follows general rules of thermal conductivity: thermal conductivity is higher for the direction of stronger atomic bonding and for materials with lighter elements. For transition metal dichalcogenides (TMDs), the chalcogen elements determine the overall in-plane thermal conductivity, as the phonon spectra of chalcogen elements dominate near the Debye frequency.

The interface thermal conductance with metals is very low, i.e., the lowest is ≈ 20 MW m^{-2} K^{-1} for ReS_2 with Al or NbV. This is in accordance with the through-plane thermal conductivity being more than an order of magnitude smaller than the in-plane thermal conductivity. The low thermal conductance along the through-plane direction can seriously limit heat dissipation when 2D materials are implemented in electronic devices.

Time-domain thermoreflectance (TDTR) of beam-offset geometry with NbV as a transducer is useful for measuring in-plane thermal conductivity along any arbitrary direction on surface. However, this technique requires a significantly large thickness of a sample for lateral heat transport to occur, compared with an NbV layer. This imposes a lower limit on the flake thicknesses and all the reported values in this thesis are for the flakes of a-few-hundreds nm thickness and represent the values in bulk limit.

Second, I demonstrate that an ultrathin Co layer is a useful thermometer for studying non-equilibrium heat transport. Time-resolved magneto-optical Kerr effect (TR-MOKE) on the

Co layer informs temperature evolution of magnons, which thermalize rapidly with electrons, i.e., $\tau_{em} \approx 0.2$ ps. The use of an ultrathin thermometer also eliminates the uncertainty in position-dependence of temperature.

By using an ultrathin Co layer as a thermometer, I determine the electron-phonon coupling parameter of Pt as 6×10^{17} W m^{-3} K^{-1}. The temperature evolutions in Pt/Co/Pt trilayers with Pt thicknesses of 2−42 nm can be adequately described by a phenomenological three-temperature model with a consistent set of materials parameters. I also demonstrate that transition metals have much shorter electron-phonon coupling lengths compared with noble metals. Thus, the laser energy in transition metals is carried mostly by electrons and phonons in equilibrium with each other, while the energy in noble metals is predominantly carried by electrons.

Finally, I report the effective thermal conductivity of MgO and $MgAl_2O_4$ tunnel barriers of 2 nm thickness in magnetic tunnel junction structures. The challenge is to separate the thermal conductance of tunnel barriers with the thermal conductance with a dielectric substrate. I use a 1-nm-thick ferromagnetic electrode layer (Co or CoFeB) as a thermometer, for which the tunnel barrier and the substrate are located in the opposite sides. TDTR measurement on the top layer of Ru informs the sum of two thermal conductances, while TR-MOKE allows to separate the contributions of the two thermal conductances. As a result, I obtain 0.23−0.8 W m^{-1} K^{-1} for MgO (with Co and CoFeB) and 0.4−0.8 for $MgAl_2O_4$ (with CoFeB). These results are much smaller than nanocrystalline MgO films and suggest the contributions from the two interfaces are dominant. In addition to the effective thermal conductivity of a tunnel barrier, non-equilibrium between electrons and phonons across the tunnel barrier should be considered for proper evaluation of a temperature drop across the tunnel barrier.

APPENDIX A

TWO-COLOR PUMP-PROBE SETUP

USING AN OPTICAL PARAMETRIC OSCILLATOR

The optical pump-probe setup presented in Chap. 2 is used for all of the measurements in this thesis. However, the optical setup suffers from a long pulse duration ≈ 1.2 ps for the cross-correlation of pump and probe pulses. Although the output pulses of the Ti:sapphire laser have pulse duration < 400 fs, significant dispersion is caused by the electro-optic modulator of a 160-mm-long KDP birefringent crystal and the ultrasteep edge spectral filters. The elongated pulse duration at the sample stage limits the temporal resolution of time-resolved experiments and prevents the observation of fast dynamic processes that occur on sub-picosecond time scale.

To improve the temporal resolution and additionally obtain tunability of wavelength, we set up a two-color pump-probe setup using an optical parametric oscillator. A Ti:sapphire laser (Spectra-Physics, Mai Tai HP) pumps an optical parametric oscillator (OPO) (Spectra-Physics, Inspire HF100), which has four laser outputs: depleted pump, second-harmonic generation, signal, and idler. To prevent the confusion with "pump" in pump-probe measurement, the depleted pump is referred to as "NIR." The NIR (wavelength fixed at 820 nm) and signal (490−750 nm) outputs are used for two-color pump-probe measurement. The use of pump and probe beams at different wavelengths eliminates the need of the ultrasteep edge filters.

Currently, the NIR beam has wavelength of 820±8 nm and the signal beam path is optimized for 632 nm wavelength with 6 nm width. A pulse of the NIR follows a sech^2 function, and the bandwidth-limited pulse duration is 88 fs by assuming a time-bandwidth-product of

0.315 for a $sech^2$ pulse. A time-bandwidth-product of the signal is provided from a manufacturer (Radiants) and is 0.6, giving the bandwidth-limited pulse duration as 133 fs. The pulse durations measured for the laser outputs using an auto-correlator (APE, PulseCheck) are 117 fs for the NIR and 244 fs for the signal. Therefore, the signal beam appears to be broader than the bandwidth-limited duration.

The laser pulses further undergo broadening due to group-delay-dispersions (GDDs) of optics. The largest GDDs are introduced from polarizing beam splitters and acousto-optic modulators (AOMs): polarizing beam splitters are commonly made of N-SF1 glass, which has a group-velocity-dispersion (GVD) of 140 fs^2/mm at 820 nm and 220 fs^2/mm at 630 nm wavelength. We use 5-mm-thick cube polarizing beam splitters when needed, which is the minimum thickness than can contain the electric field of laser beams, i.e., $1/e^2$ radius is ≈0.9−1 mm for both NIR and signal outputs. This cube beam splitter creates GDD of 700 fs^2 and 1100 fs^2 for NIR and signal, respectively. The AOMs are made of fused silica and the 35 mm thickness creates GDD of 1225 fs^2 and 1820 fs^2 for NIR and signal, respectively. The estimated total GDDs are 3000 fs^2 for NIR and 3600 fs^2 for signal before the microscope objective lens. The objective lens further introduces significant broadening in pulse durations. The cross-correlation of pump and probe pulses measured by a GaP photodiode with a 10× lens is 450 fs.

To interchangeably use the NIR and signal outputs for pump and probe, each of the laser outputs is modulated with a square wave by an acousto-optic modulator (AOM: Isomet M1133-aQ110L-2 for signal, M1133-aQ80L-1.5 for NIR; RF-driver: APE, Inc.). The phases of the two modulation frequencies are locked to each other by locking the time-base of one function generator to the 10 MHz internal oscillator of the other function generator. Regarding a material for AOMs, quartz is chosen over other materials, such as TeO_2, due to the much lower group

velocity dispersion in quartz. The diffraction efficiencies are 75% for NIR and 65% for signal, and the first-order diffraction beams are used for measurements, as the background power is negligible.

The rise time of modulation is determined by the travel time of an acoustic wave generated in quartz across the beam diameter. The smaller beam size allows for higher modulation frequencies but reduces the diffraction efficiency as the interaction volume with the acoustic wave is decreased. I use a spherical lens of 45−50 cm focal length to focus the NIR and signal in the middle of the quartz crystal to minimize the beam divergence inside the crystal. The larger the beam divergence is inside the AOM, the more elliptical the diffracted beam becomes, and the lower diffraction efficiency it has. The ellipticity and divergence of the diffracted beams are corrected by using a pair of cylindrical lenses, whose focal lengths are 50 cm (for vertical axis) and 70 cm (for horizontal axis) in order.

I use a dichroic beam splitter (SEMROCK, FF725-SDi01-25-D for signal transmission, FF740-DI01-25-D for NIR transmission) to reflect the pump beam and transmit the probe beam. A non-polarizing beam splitter (Newport, 10BC17MB.1 for signal, 10BC17MB.2 for NIR) is used for reflection and transmission of the probe beam. A plate beam splitter (Thorlabs, BSS04) creates less broadening in pulse duration due to smaller thickness, i.e., 3 mm, but its reflectance and transmission largely depend on polarization of light, making it less desirable for TR-MOKE measurement. The reflected probe is collected by a Si photodiode for TDTR measurement or by a balanced amplified photodiode for TR-MOKE measurement, as shown in Figure A.1 and A.2. As both the pump and probe are modulated at two different frequencies, i.e., f_1 and f_2, a lock-in amplifier is synchronized to the difference of the frequencies, i.e., $f_1 - f_2$. The reference frequency

is generated via a frequency mixer with f_1 and f_2 inputs and a low pass filter at 2.5 MHz to pass only the frequency difference.

Noise in the laser outputs is measured by using a Si photodiode and the noise measurement function of a lock-in amplifier (SRS, SR865A). The voltage output of the Si photodiode is multiplied by a factor of five through a preamplifier and is read by the lock-in amplifier. Figure A.3 shows the noise in the NIR and signal as a function of frequency for different time constants (τ) of the lock-in and a single-pole filter (6 dB/octave). The wait time for noise measurement is 200 times of a time constant. The cut-off frequency of the low pass filter is estimated as $1/4\tau$, and the noise below the cut-off frequency is not accurate. In Fig. A.3(a), the noise in the NIR shows f^{-1} dependence up to 1 kHz and becomes flat at the higher frequencies. I expect the noise at > 1 kHz is dominated by the noise from electronic sources. The noise level of the signal is higher than that of the NIR by about an order of magnitude, which can be expected as the signal is generated via a non-linear effect from the NIR in the OPO crystal.

The modulation frequencies of the pump and probe beams are about 1−7 MHz. At this frequency range, the noise level in TDTR signal is dominated by the noise level in laser intensity. A resonant filter, which consists of an inductor in series, and a capacitor in parallel as optional, helps to improve the signal-to-noise ratio, e.g., at 1.9 MHz, the gains in signal and noise are ≈13 and ≈8, respectively. The preamplifier amplifies both signal and noise by a factor of five and does not contribute to enhancing the signal-to-noise ratio.

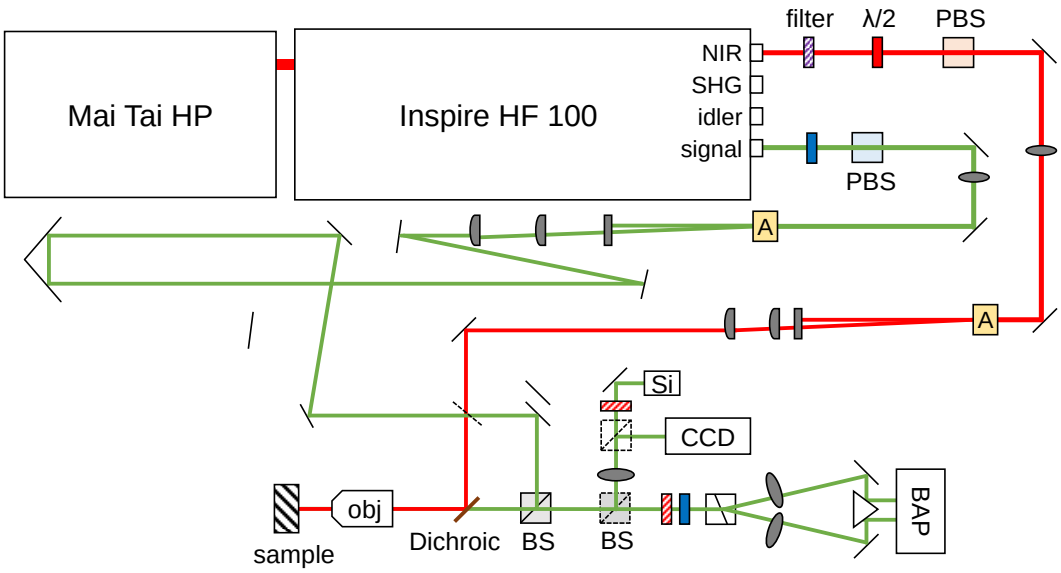

Figure A.1. Optical pump-probe setup using an optical parametric laser when NIR at 820 nm wavelength is a pump beam and signal at 632 nm is a probe beam. “A” is an acousto-optic modulator.

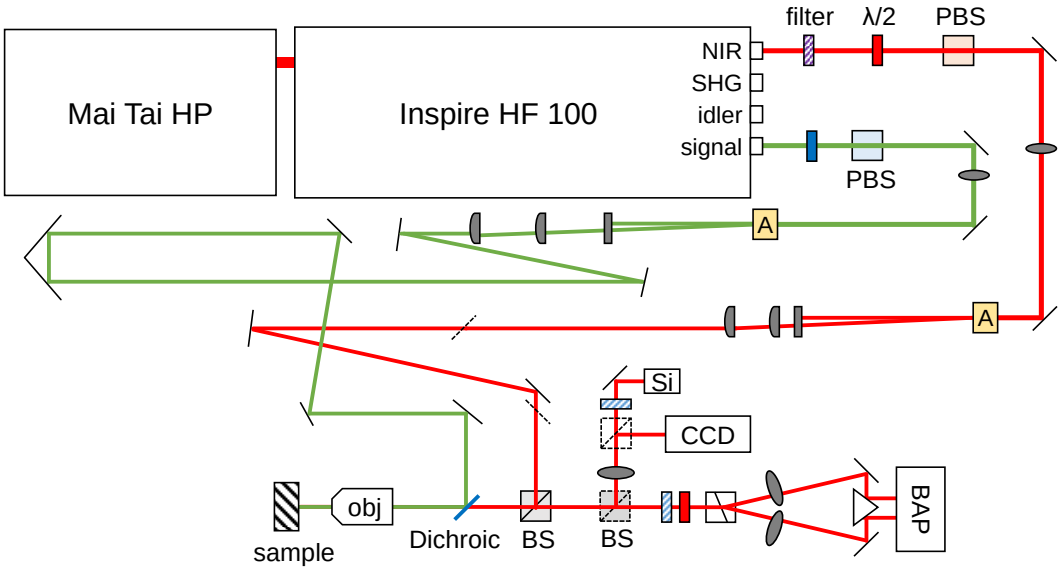

Figure A.2. Optical pump-probe setup using an optical parametric laser when signal at 632 nm is a pump beam and NIR at 820 nm wavelength is a probe beam.

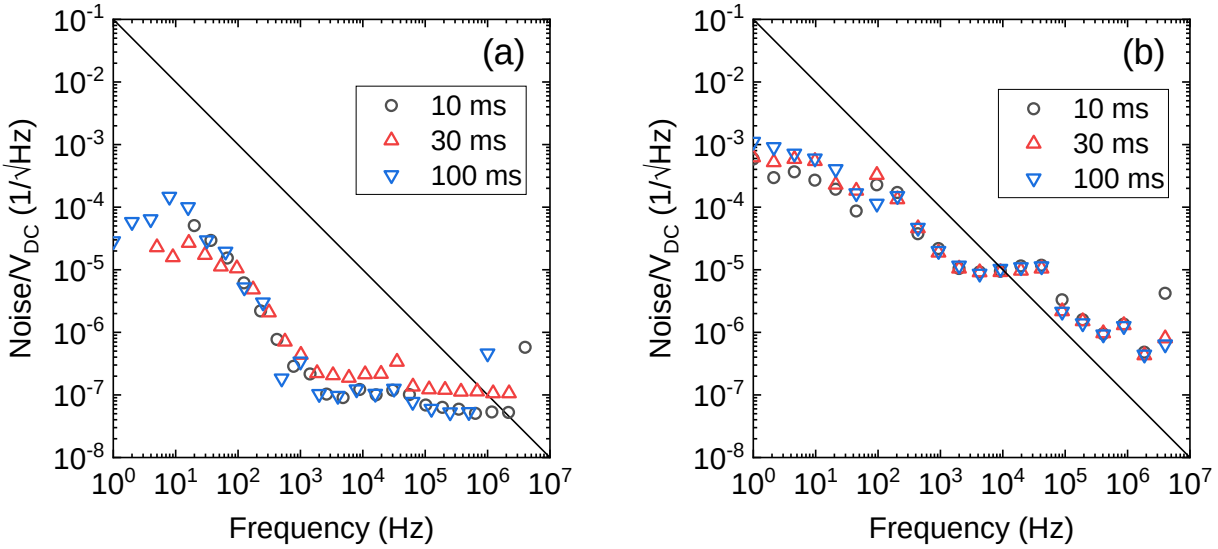

Figure A.3. Noise measurement using a lock-in amplifier for (a) NIR at 820 nm wavelength and (b) signal at 632 nm. Open symbols are noise measured with different time constants for the lock-in amplifier, 10 ms (black), 30 ms (red), and 100 ms (blue) and the low-pass-filter slope of 6 dB/octave.